



Faculteit Wetenschappen
Departement Fysica

Hyperfine Parameters and Radiation Damage in Semiconductors and Superconducting Materials

Hyperfijn Parameters en Stralingschade in Halfgeleiders en Supergeleidende Materialen

Proefschrift voorgelegd tot het behalen van de graad van doctor in de
Wetenschappen aan de Universiteit Antwerpen te verdedigen door

Yamiel Abreu Alfonso

Promotoren

prof. dr. Carlos M. Cruz Inclán
prof. dr. Piet Van Espen
prof. dr. Nick Van Remortel

Antwerpen, 2014

“For David, Ivelisse and my family.”

Acknowledgements

This thesis is the result of several years of work, in which I have received the support of many colleagues, friends and family. Already close to the end of this stage I look back and lot of emotions comes over me, thanks you all.

The best thing that happened in my life as a Physics student and researcher was to meet my promotor, prof. dr. Carlos M. Cruz Inclán. Thanks for your teachings, guide and patience. If I've got here is due to your clear vision of the scientific problems addressed in this thesis.

When the collaboration with prof. dr. Piet Van Espen started I could not imagine the magnitude of what we just began to do and how much I would learn as a scientist, but also as a human being. Thanks for the opportunity to work together, for your confidence and for your support to my thesis as promotor.

Thanks also to my promotor prof. dr. Nick Van Remortel for your support and the enthusiastic discussions we had about the thesis. Your comments and suggestions improved a lot my work and the way I see my own thesis.

Special thanks to Ana Esther for giving me the opportunity to work in this international collaboration, for the confidence and for your comments on my thesis. You are like a mother to me.

Thanks to my friend Ibrahim for all your support, we've been together on this physics journey for many years and each day seems to be more interesting.

Thanks to Dr. Antonio Leyva for your advices, for your support to this thesis and in my scientific career.

Thanks to the jury members (prof. D. Lamoen, prof. B. Partoens, prof. S. Cottenier, prof. P. Van Espen, prof. N. Van Remortel and prof. C. Cruz), your suggestions and comments were really valuable.

Thanks to my colleagues at CEADEN, especially from the Radiation Damage and Detectors Group (Carlos, Ibra, Tony, Ana, Angelina, Diana, Rosana, Sunay y Alianna), for the enthusiasm and friendship during these last 10 years.

Another special thanks to Fabiana, for your unconditional support and friendship.

Thanks to my friends here in Belgium and the Latin community, for make me feel at home.

To my colleagues at UA, especially from the Axes group, thanks for the nice working environment.

Thanks to the UA network and CALCUA groups for the support in the achievement of the thesis calculations.

Thanks to the authors of WIEN2k for the goodwill giving me access to your code.

Thanks to all the people and institutions that contribute to my scientific training and to this thesis.

Finally, I want to thanks to my family for the support and patience during these years of mutual sacrifices. You are always with me, present in every act of my life. Without you none of this makes sense.

YAMIEL ABREU ALFONSO

Contents

List of abbreviations	1
Introduction	3
I. EXPERIMENTAL TECHNIQUES AND COMPUTATIONAL METHODS	7
1. Hyperfine interactions techniques	9
1.1. General aspects	9
1.2. Electric hyperfine interaction	10
1.2.1. Isomer shift	11
1.2.2. Electric quadrupole splitting	13
1.3. Magnetic hyperfine interaction	14
1.4. Hyperfine interaction measurement techniques	16
1.4.1. Mössbauer spectroscopy	16
1.4.2. Perturbed angular correlation spectroscopy	22
2. Electronic structure calculation method	25
2.1. Quantum many body problem	25
2.2. Born-Oppenheimer approximation	27
2.3. Density functional theory method	28
2.3.1. The Hohenberg and Kohn theorems	30
2.3.2. The Kohn-Sham equations	32
2.3.3. The exchange-correlation functional	35
2.4. Solving the electronic problem in practice	41
2.5. All-electron methods	46
2.6. The full potential augmented plane wave (APW) methods	47
2.6.1. The linearized augmented plane wave (LAPW) method	48

2.6.2. The augmented plane wave with local orbitals (APW+lo) method	49
2.7. Hyperfine interaction parameters calculation through density functional theory	49
2.7.1. Hyperfine electric parameters calculation	49
2.7.2. Hyperfine magnetic parameters calculation	52
2.8. Calculation Methodology	53

II. NUMERICAL RESULTS AND VALIDATION OF EXPERIMENTS 55

3. Radiation damage and calculation of hyperfine parameters in ZnO implanted with ^{57}Mn (^{57}Fe) and ^{111}In (^{111}Cd) 57

3.1. Introduction	57
3.2. Calculation Details	60
3.3. Results and Discussion	65
3.3.1. Results for ^{57}Mn (^{57}Fe) into ZnO	66
3.3.2. Results for ^{111}In (^{111}Cd) into ZnO	75
3.4. Conclusions	79

4. Radiation damage and hyperfine parameters calculation results in Si samples implanted with ^{57}Mn (^{57}Fe) 81

4.1. Introduction	81
4.2. Calculation Details	82
4.3. Results and Discussion	85
4.4. Conclusions	90

5. Hyperfine parameters calculations in $\text{YBa}_2\text{Cu}_{3-x}\text{Fe}_x\text{O}_{7-y}$ 91

5.1. Introduction	91
5.2. Calculation Details	92
5.3. Results and Discussion	96
5.4. Conclusions	100

Summary 101

Samenvatting 105

Bibliography 109

List of figures	117
List of tables	119
List of publications	121
Curriculum Vitae	125

*“Learn from yesterday, live for today, hope for tomorrow.
The important thing is to not stop questioning.”*

— Albert Einstein, *Relativity: The Special and the General Theory*

List of abbreviations

NMR	Nuclear Magnetic Resonance
MS	Mössbauer Spectroscopy
PAC	Perturbed Angular Correlation
EFG	Electric Field Gradient
DFT	Density Functional Theory
IS	Isomer Shift
QS	Quadruple Splitting
HF	Hartree-Fock
CI	Configuration Interaction
LDA	Local Density Approximation
LSDA	Local Spin Density Approximation
GGA	Generalized Gradient Approximations
MTO	Muffin Tin Orbitals
KKR	Korringa, Kohn and Rostocker
LMTO	Linear Muffin Tin Orbitals
APW	Augmented Plane Waves
FP-APW	Full Potential Augmented Plane Wave
LAPW	Linearized Augmented Plane W
BCA	Binary Collision Approximation
SC	Supercell
DPA	Displacement Per Atom

Introduction

Hyperfine interaction techniques, like Nuclear Magnetic Resonance (NMR), Mössbauer Spectroscopy (MS) or Perturbed Angular Correlation (PAC), have been used for a long time to study radiation effects and defects in solids [1, 2]. Microscopic details of defects and impurities have been studied by these techniques, with most emphasis in metallic and alloy systems [3–16], as well as in semiconductors [17–31]. Further studies have reported radiation damage in different materials like magnets [32], oxides [33–38], superconductors [39–42] and others [43].

Defects in solids can induce characteristic electric field gradient (EFG) in their neighboring lattice sites. The EFG is measured via its interaction with the nuclear electric quadrupole moment of a suitable probe atom by the mentioned hyperfine techniques. Defect-related EFG have been successfully used as “fingerprints” of the respective defects in the past, because they are very sensitive to an anisotropic charge distribution about the probe nucleus, caused, for example, by a neighboring defect [1, 44, 45]. However, the EFG by itself does not tell much about its microscopic origin, due to the lack of appropriate theories for predicting the EFG of a distinct defect. Many defects are experimentally well characterized via their EFG, but have remained unidentified.

Classical methods, like the point-dipole approximation, were used in the past to estimate the EFG values [46–48], this is a simple and fast model, but not precise in most cases [49]. On the other hand, calculations based on the Density Functional Theory (DFT) formalism have been successfully used for determining hyperfine parameters and other properties of solids [2, 49–58]. But, studies yielding also the EFG caused by defects and impurities, came up only in the last 15 years [59–61].

Several open questions still remain regarding the local environments characterization of defects and dopant’s in various materials, and its relation with the hyperfine parameters observed in those cases. In this thesis some practical and methodological interesting cases in semiconductor and superconductor materials are presented and analyzed.

In this context, the present thesis aims as general objective, the identification of the structural origin of the hyperfine parameters values observed experimentally in the analyzed semiconductor and superconductor materials; explaining the hyperfine parameter changes due to the presence of defects in the material provoked by radiation damage.

It starts from the hypothesis that, by the structural simulation of the defects configurations in the materials and its electronic structure calculation, it is possible to achieve a better understanding of the experimentally observed hyperfine parameters and the influence of radiation damage at the microscopic level.

To fulfill this purpose, we address the following specific objectives:

1. Simulate the implanted ion and vacancy distribution profiles in the material in the case of ion irradiated materials, to assess the produced concentrations of defects.
2. Propose a representative set of local defects and implantation configurations starting from the structural data of each studied material.
3. Apply the DFT electronic structure calculation method to obtain the hyperfine parameters for each proposed configuration.
4. Compare the obtained hyperfine parameters values with experimental measurements, and if possible, give a structural explanation of the differences and similarities.
5. Based on the obtained results, make an interpretation of the radiation damage effects and their evolution in a selection of well studied samples.

As studied cases, the following materials were selected: the semiconductors zinc oxide (ZnO) and silicon (Si), and the superconductor yttrium barium copper oxide ($\text{YBa}_2\text{Cu}_{3-x}\text{Fe}_x\text{O}_{7-y}$). In the semiconductors cases the radiation damage is mainly produced by the implantation of an hyperfine interaction probe atom, ^{57}Mn (^{57}Fe) and ^{111}In (^{111}Cd) in ZnO, as well as ^{57}Mn (^{57}Fe) in Si. In the superconductor, the crystal structure presents some intrinsic disorder changes caused by high pressure synthesis or gamma irradiation of the material.

The semiconductor ZnO has an increasing interest in the research community in part because of its large exciton binding energy of 60 meV, which could lead to lasing action based on exciton recombination even above room temperature. The research on ZnO goes back to many decades. The renewed interest in ZnO is mostly due to the availability of high-quality substrates, and recent reports of p-type conduction and

ferromagnetic behavior when doped with transition metals. Several studies regarding structural characteristics, vibrational and optical properties, samples growth and its practical applications has been reported since 1930's. A complete review of ZnO materials, applications and devices was published by Özgür *et al.* [62].

Impurity doping of silicon by ion implantation is relevant for materials studies and modifications, as well as for technological applications [17–21, 45, 63]. Several experimental and theoretical studies have been performed in this field. The radiation damage created during the ion implantation is a fundamental problem in these cases, including its annealing, and most of the time difficult to interpret. In these cases the experimental observations can be complemented with theoretical models.

Recently, Mössbauer spectra have been reported of $\text{YBa}_2\text{Cu}_{3-x}\text{Fe}_x\text{O}_{7-y}$ superconductor samples synthesized at high pressure [39–41]. In this studies significant changes have been observed in the spectra as a result of the increase of the oxygen and iron dopant content in the samples, which provoked the total extinction of one of the quadrupole doublet that are commonly observed in those samples synthesized at normal pressure [42, 64, 65]. Gamma irradiation effect on $\text{YBa}_2\text{Cu}_{3-x}\text{Fe}_x\text{O}_{7-y}$ samples was attributed, according to MS measurements [42], to changes in the oxygen coordination environment around the probe atom. These facts motivate the review of the atomic local micro-structure that can be present in the $\text{YBa}_2\text{Cu}_3\text{O}_{7-y}$ doped with Fe, which could give origin to the observed phenomena.

More details on the specific related problems are analyzed in the thesis.

The thesis is organized in two parts, the first part contains two chapters, chapter 1 is related to the hyperfine interaction techniques and chapter 2 to the electronic structure computational method used in the present study. The second part is divided in three chapters where the calculated hyperfine parameters, the validation of experiments and the possible interpretation in terms of radiation damage are presented. In this way, chapter 3 shows the results for the ZnO semiconductor implanted with ^{57}Mn (^{57}Fe) and ^{111}In (^{111}Cd), chapter 4 analyzes the case of ^{57}Mn (^{57}Fe) implanted into Si, and chapter 5 presents the obtained results for $\text{YBa}_2\text{Cu}_3\text{O}_{7-y}$ samples doped with Fe and irradiated with gamma rays. A summary is presented at the end, followed by the bibliography.

Part I.

**EXPERIMENTAL TECHNIQUES AND
COMPUTATIONAL METHODS**

Chapter 1.

Hyperfine interactions techniques

1.1. General aspects

The atomic nuclei form a quantum subsystem within solids which in the Born Oppenheimer approximation, can be described by an effective Hamiltonian, that is relatively independent from the Hamiltonian describing the surrounding electrons. Nevertheless, there are a number of mutual interactions between both subsystems, which are analyzed in terms of perturbations. On the atomic nuclei subsystem, the nucleons that form these nuclei represent a third kind of dynamic subsystem, whose internal motions are relatively independent from the other two subsystems that make up the solid. Then, the hyperfine interaction Hamiltonian $\hat{H}_{hf}(t)$ is defined as the result of the perturbation of a particular nuclear subsystem Hamiltonian \hat{H}_0 done by its electromagnetic interaction with the electrons. Due to the difference in motion energies and frequency of the nucleons in relation to the electrons, the first feel an average electromagnetic action exerted by the electrons that move faster due to their lower mass. For that reason the perturbation to \hat{H}_0 can be analyzed as a static interaction $\langle \hat{H}_{hf}(t) \rangle_{\Delta t} = \hat{H}_{hf}$, where Δt is a time characteristic of the electronic movement. Then, it can be expressed as:

$$\hat{H}_{hf} = \hat{H}_{hf}^E + \hat{H}_{hf}^M \quad (1.1)$$

where \hat{H}_{hf}^M represents the Zeeman magnetic interaction and \hat{H}_{hf}^E the electrostatic interaction.

Thus, the hyperfine interactions are introduced as a perturbation problem where we denote the eigenfunctions with energy $E_m^{(0)}$ of the non-perturbed atomic nucleus states of the Hamiltonian \hat{H}_0 with degeneration $s = I(I + 1)$ by $\psi_m^{(0)}(m = 1, \dots, s)$,

where the quantum numbers on regard to the nuclear spin \mathbf{I} and other ones were not explicitly displayed for simplicity's sake. As a result of the perturbation described by Hamiltonian \hat{H}_{hf} the degeneracy of the energy levels is broken, causing the atomic nucleus to occupy any of the perturbed states ψ'_i , which are expressed according to the first order perturbation theory as [66]:

$$\psi'_i = \sum_{m=1}^s C_{im}^{(0)} \psi_m^{(0)} \quad (1.2)$$

$$\sum_{m=1}^s C_{im}^{(0)} ((\hat{H}_{hf})_{m,m'} - \Delta E_i^{(1)} \delta_{m,m'}) = 0, (m' = 1, \dots, s) \quad (1.3)$$

and the perturbed energies $E'_i = E_m^0 + \Delta E_i^{(1)}$ are calculated by the characteristic equation:

$$|(\hat{H}_{hf})_{m,m'} - \delta_{m,m'} \Delta E_i^{(1)}| = 0 \quad (1.4)$$

where $(\hat{H}_{hf})_{m,m'}$ are the matrix elements of the hyperfine interaction in the degeneration functional base of sublevel E_m^0 , and $\Delta E_i^{(1)}$ is the first order perturbation energy correction.

1.2. Electric hyperfine interaction

The electrical hyperfine interactions are described by an electrostatic interaction that can be derived from the classic expression:

$$\hat{H}_{hf}^E = \int \rho_n(\mathbf{r}) \varphi(\mathbf{r}) d\mathbf{r} \quad (1.5)$$

where, $\rho_n(\mathbf{r})$ is the nuclear electrical charge density and $\varphi(\mathbf{r})$ is the electrical potential from the other electrical charges. The right side of Eq. 1.5 can be expressed as:

$$\hat{H}_{hf}^E = \sum_{i=0}^{\infty} \hat{H}^i \quad (1.6)$$

$$\hat{H}^i = \sum_{\alpha_1, \dots, \alpha_i} \frac{1}{i!} M_{\alpha_1, \dots, \alpha_i}^i V_{\alpha_1, \dots, \alpha_i} \quad (1.7)$$

being, \hat{H}^i the i -th order multi-pole electrical interaction energy and $\alpha_1, \dots, \alpha_i = 1, 2, 3$ refer to the cartesian coordinates.

These equations result from the Taylor development of $\varphi(\mathbf{r})$ at the atomic nucleus position (taken as origin of coordinates), $M_{\alpha_1, \dots, \alpha_i}^i$ are the i -th rank tensor components of the electric charge momentum distribution of the atomic nucleus $\rho_n(\mathbf{r})$ and $V_{\alpha_1, \dots, \alpha_i}$ are the i -th rank tensor components of the electric potential gradient:

$$M_{\alpha_1, \dots, \alpha_i}^i = \int \rho_n(\mathbf{r}) \cdot X_{\alpha_1} \cdots X_{\alpha_i} d\mathbf{r} \quad (1.8)$$

$$V_{\alpha_1, \dots, \alpha_i} = \frac{\partial^i}{\partial X_{\alpha_1} \cdots \partial X_{\alpha_i}} \varphi(\mathbf{r})|_{\mathbf{r}=\vec{0}} \quad (1.9)$$

being, $X_{\alpha_1}, \dots, X_{\alpha_i} = x, y$ or z , when $\alpha_1, \dots, \alpha_i = 1, 2$ or 3 respectively.

The zero-order term is an additive constant that depends only on the atomic nucleus charge Z and the potential value $\varphi(0)$, and has no influence on the calculations that are made here. The term \hat{H}^1 is canceled because it is proportional to the electric dipole moment of the nucleus, which is zero when $\rho_n(\mathbf{r})$ corresponds to a nuclear quantum state with a defined parity. Then, the \hat{H}^2 is the first term of significance, if the second-order nuclear electric charge momentum does not vanish:

$$\begin{aligned} \hat{H}^2 &= \frac{1}{2} \sum_{\alpha, \beta} M_{\alpha\beta} V_{\alpha\beta} \\ \hat{H}^2 &= \frac{1}{6} \sum_{\alpha, \beta} Tr(M) \delta_{\alpha\beta} V_{\alpha\beta} + \frac{1}{2} \sum_{\alpha, \beta} (M_{\alpha\beta} - \frac{1}{3} Tr(M) \delta_{\alpha\beta}) V_{\alpha\beta} \\ \hat{H}^2 &= \hat{H}_{IS} + \hat{H}_{QS} \end{aligned} \quad (1.10)$$

where the first term on the right, \hat{H}_{IS} , is known as the isomer shift (IS), and the last, \hat{H}_{QS} , is referred to as the nuclear electric quadrupole interaction or quadrupole splitting (QS). In the latter case, the interaction has a second rank tensor character, while the IS is a scalar.

1.2.1. Isomer shift

From Eqs. (1.10) the IS term can be expressed as:

$$\hat{H}_{IS} = \frac{1}{6} Tr(M) Tr(V_{\alpha\beta}) = -\frac{e}{6\epsilon_0} |\psi(0)|^2 \int r^2 \rho_n(\mathbf{r}) d\mathbf{r} = \frac{Ze^2}{6\epsilon_0} |\psi(0)|^2 \langle R^2 \rangle \quad (1.11)$$

In Eq. (1.11), the magnitude $|\psi(0)|^2$ represents the probability of an electron being in the atomic nucleus, while $\langle R^2 \rangle$ denotes the mean square radius of the nuclear charge density. This last, for a given isotope, depends on the nucleus energy state. Since variations of

the electronic cloud between isotopes and isomers of the same nucleus are negligible, for a given isotope nuclear sublevel, \hat{H}_{IS} will depend on the particular nuclear isomer through the magnitude $\langle R^2 \rangle$. This is why this magnitude is denominated as isomer shift.

For a given isotope, \hat{H}_{IS} will simply represent an additive constant to the $\Delta E_i^{(1)}$ values obtained by Eq. (1.4) of the hyperfine perturbation. If an experiment, as in the case of Nuclear Magnetic Resonance, involved only transitions between two hyperfine sublevels that belong to the same nuclear and electronic state, \hat{H}_{IS} will not affect the experimental results.

For the case when transition between two hyperfine sublevels that belong to different nuclear states (with the same or different electronic states) are studied, it is necessary to add the following value to the gamma quanta energy emitted without hyperfine perturbation:

$$\Lambda = H_{IS}^e - H_{IS}^g = \frac{Z}{6\epsilon_0} |\psi_0|^2 \{ \langle R^2 \rangle_e - \langle R^2 \rangle_g \} \quad (1.12)$$

since $|\psi_0|^2$ does not depend on the particular energetic state of the atomic nucleus. On the other hand, $|\psi_0|^2$ is determined by the electronic bonds characteristics of the analyzed atom in the matrix. While the term $\{ \langle R^2 \rangle_e - \langle R^2 \rangle_g \}$ represents the nucleus geometrical variation from the excited to the ground state.

Then, the magnitude given by Eq (1.12) will depend on the matrix in which that atom is embedded. This condition is critical in the Mössbauer experiment, since this involves the resonant emission and absorption of gamma quanta between a given nuclear sublevels of an isotope, but located in different matrices (source (*s*) and absorber (*a*)). Finally the isomer shift (δ) is defined as the difference in the values of Λ between the two states and given by the expression:

$$\delta = \Lambda^a - \Lambda^s = \frac{Ze^2}{6\epsilon_0} [\langle R^2 \rangle_e - \langle R^2 \rangle_g] [|\psi(0)|_a^2 - |\psi(0)|_s^2] \quad (1.13)$$

As seen from Eq. (1.13), for a given type of absorbent matrix, δ depends on the physical characteristics of the source matrix (usually δ will depend on thermodynamic parameters as pressure P and temperature T). That's why, δ values are given relative to a substance taken as reference. In the case of the Mössbauer isotope ^{57}Fe , experimental values of δ are generally referred to metallic iron or to sodium nitroprusside (NNP).

Usually, δ takes on values between -1.0 and 2.0 *mm/s* referred to metallic iron at room temperature [66, 67].

1.2.2. Electric quadrupole splitting

Based on Eq. (1.10) for \hat{H}_{QS} , it is possible to construct the Hamiltonian operator for the electric quadrupole interaction given according to the expression [66, 67]:

$$\hat{H}_{QS} = \frac{eQ}{6I(2I-1)} \sum_{\alpha,\beta} V_{\alpha\beta} \left[\frac{3}{2}(\hat{I}_\alpha \hat{I}_\beta + \hat{I}_\beta \hat{I}_\alpha) - \delta_{\alpha\beta} \hat{I}^2 \right] \quad (1.14)$$

where I is the nuclear spin, \hat{I}_α and \hat{I}_β are the conventional spin operators, and

$$Q = \frac{1}{2e} \int \rho_n(\mathbf{r})(3Z^2 - r^2) d\mathbf{r},$$

representing Q the nuclear quadrupole moment of the nucleus for the nI sub-state, been \hat{H}_{QS} equals to zero when $I = (0, \frac{1}{2})$. And $V_{\alpha\beta}$ represent the electric quadrupole tensor, which is a second rank tensor with components:

$$V_{\alpha\beta} = \left. \frac{\partial^2}{\partial X_\alpha \partial X_\beta} \varphi(\mathbf{r}) \right|_{\mathbf{r}=\vec{0}} \quad (1.15)$$

being, $X_\alpha, X_\beta = x, y$ or z , when $\alpha, \beta = 1, 2$ or 3 respectively.

For the specific case when the EFG tensor principal axes coincide with the Cartesian reference system the expression (1.14) reduces to:

$$\hat{H}_{QS} = \frac{eQ}{4I(2I-1)} \left[V_{zz}(3\hat{I}_z^2 - \hat{I}^2) + \frac{1}{2}(V_{xx} - V_{yy})(\hat{I}_-^2 - \hat{I}_+^2) \right] \quad (1.16)$$

which as noted, depends on the EFG component in the axial direction (here the z axis, indicated by \hat{I}_z , is matched with the direction of the greater absolute value of the EFG eigenvalues, $|V_{zz}|$) and the difference of the eigenvalues in the transverse direction.

Then, the following parameters related with $V_{\alpha\beta}$ components can be introduced:

$$eq = V_{zz} \quad (1.17)$$

and

$$\eta = \frac{V_{yy} - V_{xx}}{V_{zz}} \quad (1.18)$$

with the following condition $|V_{xx}| \leq |V_{yy}| \leq |V_{zz}|$, according to which $0 \leq \eta \leq 1$, leaving the expression (1.16) for \hat{H}_{QS} as follows:

$$\hat{H}_{QS} = \frac{e^2 q Q}{4I(2I-1)} \left[3\hat{I}_z^2 - \hat{I}^2 + \frac{1}{2}\eta(\hat{I}_-^2 - \hat{I}_+^2) \right] \quad (1.19)$$

Note that in the case where the crystalline lattice presents axial symmetry (*i.e.* Cubic, Tetragonal, Hexagonal) $V_{xx} = V_{yy}$ and then $\eta = 0$.

1.3. Magnetic hyperfine interaction

The third important hyperfine interaction is the Zeeman effect. This will occur if there is a magnetic field at the nucleus. The magnetic field can be originated either within the atom itself, via exchange interactions in the crystal, or as a result of placing the compound in an external applied magnetic field. For the moment, however, it is only necessary to consider that there is a magnetic field with a flux density \mathbf{B} and that its direction defines the principal z axis.

The Hamiltonian describing the magnetic dipole hyperfine interaction is:

$$\hat{H}_{hf}^M = -\boldsymbol{\mu} \cdot \mathbf{B} = -g\mu_N \mathbf{I} \cdot \mathbf{B} \quad (1.20)$$

where μ_N is the nuclear Bohr magneton ($e\hbar/2Mc$), $\boldsymbol{\mu}$ is the nuclear magnetic moment, \mathbf{I} is the nuclear spin, g is the nuclear g -factor, $g = \mu/(I\mu_N)$, and $\mu_N = 5.04929 \times 10^{-27} \text{ J T}^{-1}$. The matrix elements are easy to evaluate using the spin operator form of $H = -g\mu_N I_z B$ and result in eigenvalues of:

$$E_m = \frac{-\mu B m_I}{I} = -g\mu_N B m_I, \quad (1.21)$$

where m_I is the magnetic quantum number representing the z component of \mathbf{I} (*i.e.* $m_I = I, I-1, \dots, -I$). The magnetic field splits the nuclear levels of spin I into $(2I+1)$ equi-spaced non-degenerated substates. As for the quadrupole spectra, the Mössbauer

transition can take place between different nuclear levels if the change in the m_I values is 0, ± 1 , or additionally in some cases ± 2 .

In a similar way to the chemical isomer shift and quadrupole splitting, the magnetic hyperfine effect is the product of a nuclear term, which is a constant for a given Mössbauer transition, and the magnetic field.

The magnetic field at the nucleus can originate in several ways. A general expression would be:

$$\mathbf{B} = \mathbf{B}_0 - D\mathbf{M} + \frac{4}{3}\pi\mathbf{M} + \mathbf{B}_c + \mathbf{B}_{orb} + \mathbf{B}_{dip} \quad (1.22)$$

where \mathbf{B}_0 is the value of the magnetic field at the nucleus generated by an external magnet, \mathbf{M} is the magnetization, $-D\mathbf{M}$ is the demagnetizing field and $\frac{4}{3}\pi\mathbf{M}$ is the Lorentz field (the coefficient being strictly applicable for cubic symmetry only). These last two terms are usually small and negligible. \mathbf{B}_c arises as a result of the interaction of the nucleus with an imbalance in the s -electrons spin density at the nucleus. \mathbf{B}_c is usually referred as the Fermi contact term. Its origin may be from intrinsic impairing of the actual s -electrons, or indirectly as a result of polarization effects on filled s -orbitals. These can occur if the atom has unpaired electrons in d - or f -orbitals, or if it is chemically bonded to such an atom. Intuitively, one can see that, the interaction of an unpaired d -electron with the s -electrons of parallel spin will be different to that with the s -electrons of opposed spin. The result is a slight imbalance of spin density at the nucleus. In the case of metals, direct conduction-electron polarization as well as indirect core-polarization effects may be important.

If the orbital magnetic moment of the parent atom is non-zero, there is a further term in Eq. (1.22), \mathbf{B}_{orb} , that is related with the magnetic field due to any resultant orbital angular momentum. The final term \mathbf{B}_{dip} arises from the dipole interaction of the nucleus with the spin moment of the atom.

The terms \mathbf{B}_c , \mathbf{B}_{orb} , and \mathbf{B}_{dip} can be of the order of 1 – 10 T and their sum is usually referred as the internal magnetic field. It is already clear that the measured internal field can be related to the orbital state of the atom.

The sign of an internal magnetic field \mathbf{B}_{Int} can be readily determined. Equation (1.22) shows that application of an external magnetic field \mathbf{B}_0 alters the effective field at the nucleus, increasing or decreasing \mathbf{B} according to whether the applied field is parallel or antiparallel to \mathbf{B}_{Int} . The fields required for this are rather large, about 3 – 5 T, and

superconducting magnets are usually used. If there are two or more field directions present as in antiferromagnetic materials, it may be possible to distinguish the sublattice resonance lines by the opposite effects of the applied field. This method will fail if the magnetic interaction is highly anisotropic so as to prevent the polarization of the ordered spins by the external field.

From the current statements, it might be assumed that all compounds containing unpaired valence electrons would show a hyperfine magnetic splitting effect. However, there is another factor which has not been considered, namely that the Hamiltonian in Eq. (1.20) contains \mathbf{I} and \mathbf{B} as a vector product, and the observation time-scale is of the order of 10^{-8} s. The electronic spins which generate \mathbf{B}_{Int} are subject to changes of direction, known as electronic spin relaxation. In paramagnetic compounds, the spin relaxation is usually rapid and results in \mathbf{B}_{Int} having a time-average of zero so that no magnetic splitting is seen. The major exceptions are found in rare earths or with magnetically dilute solid solutions. When cooperative phenomena such as ferromagnetism or antiferromagnetism operate, the relaxation rates are effectively slower and a splitting will be recorded. More complex situations can be also present [66].

1.4. Hyperfine interaction measurement techniques

Hyperfine interactions can be measured by several experimental techniques like Mössbauer Spectroscopy, Perturbed Angular Correlations (PAC), Nuclear Magnetic Resonance and others. In the following sessions details on the first two mentioned will be given, since they are close related with the present study.

1.4.1. Mössbauer spectroscopy

The following discussion will focus on the hyperfine interaction measurements that use the ^{57}Fe isotope to perform Mössbauer spectroscopy. This isotope is used most frequently in experiments for several reasons described in [66] and is particularly analyzed in the current thesis.

Let us suppose first that, a ^{57}Fe nucleus is in an excited state E_e and embedded in a solid matrix, and it makes a transition to the ground state E_g . Denoting $E_\gamma^0 = E_e - E_g$, then gamma quanta energy resulting from such a transition will be $E_\gamma = E_\gamma^0 - E_R$, where

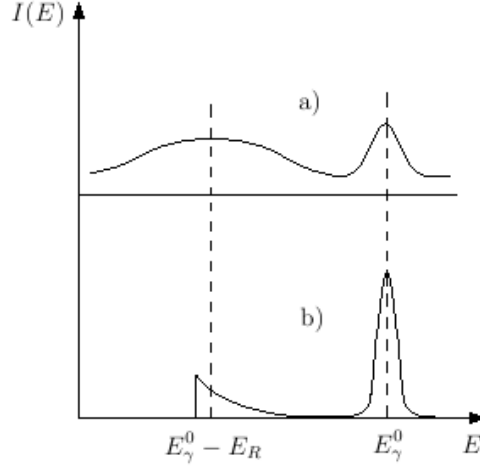


Figure 1.1.: Schematic spectrum of ^{57}Fe gamma emission for: a) weakly bound atom, and b) fixed atom.

E_R is the nucleus recoil energy. Hence, this energy will be different from the intrinsic energy level difference E_γ^0 . Momentum conservation implies that the momentum of the recoiling nucleus has equal value and opposite direction to the momentum of the emitted gamma ray: $\mathbf{p}_R = -\mathbf{p}_\gamma$. This in turn translates to a recoil energy of the nucleus of:

$$E_R = \frac{p_R^2}{2M} = \frac{p_\gamma^2}{2M} = \frac{E_\gamma^2}{2Mc^2} \cong \frac{(E_\gamma^0)^2}{2Mc^2} \quad (1.23)$$

as usually the recoil energy is very small. Here M is the mass of the nucleus.

However, due to the Mössbauer effect in solids, depending on the recoil energy E_R value, it may not be able to excite phonon states in the crystal lattice, because the phonon's energy levels are quantized. In this case the recoil energy is distributed throughout the mass of the crystal, as a consequence of which E_R has a very small value and the gamma quanta emission is done practically at the energy E_γ^0 .

Figure 1.1 shows schematically the distribution of the gamma radiation emitted by the nucleus (in this case ^{57}Fe) embedded in a solid matrix for two cases:

- a) The nucleus is weakly bound to the crystal lattice.
- b) The nucleus is fixed in the crystal lattice.

This figure shows that if the ^{57}Fe atom is strongly bound to the crystal lattice then the nuclear transition line will be more narrow, therefore increasing the gamma radiation proportion of the characteristic line with energy E_γ^0 that is emitted without recoil energy.

This process constitutes the essence of the Mössbauer effect. The probability that the E_γ^0 emission without recoil energy is carried out is known as the Mössbauer factor f , it is expressed as:

$$f = \exp[-k^2 \langle x^2 \rangle] \quad (1.24)$$

where $\langle x^2 \rangle$ expressed the average quadratic deviation of the nucleus from its balance position. From this equation is clear that, for weakly bound nucleus $\langle x^2 \rangle$ is very high and the Mössbauer factor, f , diminishes, in conformity with Figure 1.1 representation. These statements for the emission, are also valid for the absorption of gamma quanta with energy E_γ^0 from the ground state E_g to the excited state E_e .

In Figure 1.2 the schematic outline of the Mössbauer effect measurement in the transmission geometry is represented. A source (S) (*i.e.* ^{57}Co in a given matrix Pd, Rh, etc.) is fixed to a transducer that develops a periodic movement, giving to the source a lineal speed $\vec{v}(t)$ with a dependence of the transducer characteristic time.

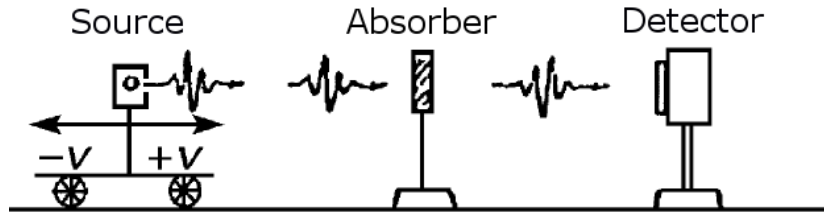


Figure 1.2.: Representation of the typical outline of the Mössbauer effect measurement in the transmission geometry.

Under static conditions this resonant absorption would not take place due to the reasons explained before, since the natural width Γ of the line is much smaller than the value $\Delta E_i^{(1)}$ of those hyperfine interactions. To solve this difficulty, the source (S) needs to be moved at certain speed $v(t)$.

Then, due to the Doppler effect of first order, the source (S) will emit the characteristic radiation E_γ^0 with a small energy variation δE given by the relative speed $v(t)$ of the source (S) with respect to the absorbent (A), that is supposed to be in rest.

When the gamma quanta with energy $E_\gamma^0 + \delta E$ interact with the absorbent (A), they can produce the ^{57}Fe transition from the ground state E_g^A to the excited one E_e^A with the probability f .

In general, $E_g^S \neq E_g^A$ and $E_e^S \neq E_e^A$, then $E_e^A - E_g^A \neq E_e^S - E_g^S$, because those ^{57}Fe nuclei are embedded in different matrix, reason why the isomer shift $\delta \neq 0$, while the magnitude of the nuclear quadrupole hyperfine interaction \hat{H}_{QS} is also different because the EFG depends on each particular matrix.

The detection system (D) is synchronized in time with the transducer. In that way, each velocity value, v_i , corresponds to a specific channel i in the multichannel counter.

In ^{57}Fe Mössbauer Spectroscopy one usually works with the gamma emission and absorption among the excited level with $I_e = \frac{3}{2}$ and the ground level $I_g = \frac{1}{2}$. The emitted gamma quanta energy value is 14.4 keV. In Figure 1.3 the simplified disintegration scheme of $^{57}\text{Mn}(^{57}\text{Fe})$ is shown.

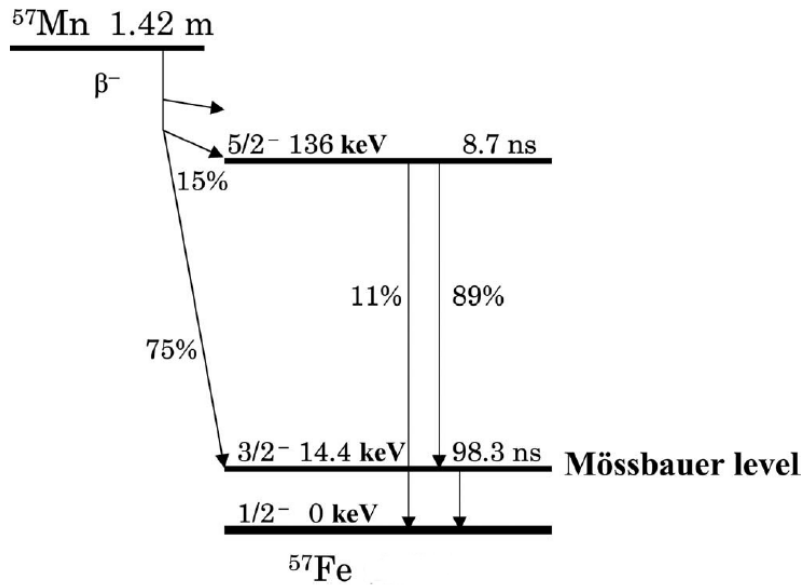


Figure 1.3.: Simplified disintegration scheme of $^{57}\text{Mn}(^{57}\text{Fe})$ [68].

The hyperfine interactions in the case of a transition $\frac{1}{2} \rightarrow \frac{3}{2}$ is schematically represented in Figure 1.4. The first interaction is the Isomer Shift, expressed by Eq. (1.13). This Eq. (1.13) can be expressed in terms of the difference between the electron density at the nucleus in the absorber $\rho_A(0)$ and in the source $\rho_S(0)$ using the following expression [69]:

$$\delta = \frac{2}{3}\pi ZS(Z)[\langle R^2 \rangle_e - \langle R^2 \rangle_g][\rho_A(0) - \rho_S(0)] \quad (1.25)$$

where $S(Z)$ is a correction for the relativistic effects.

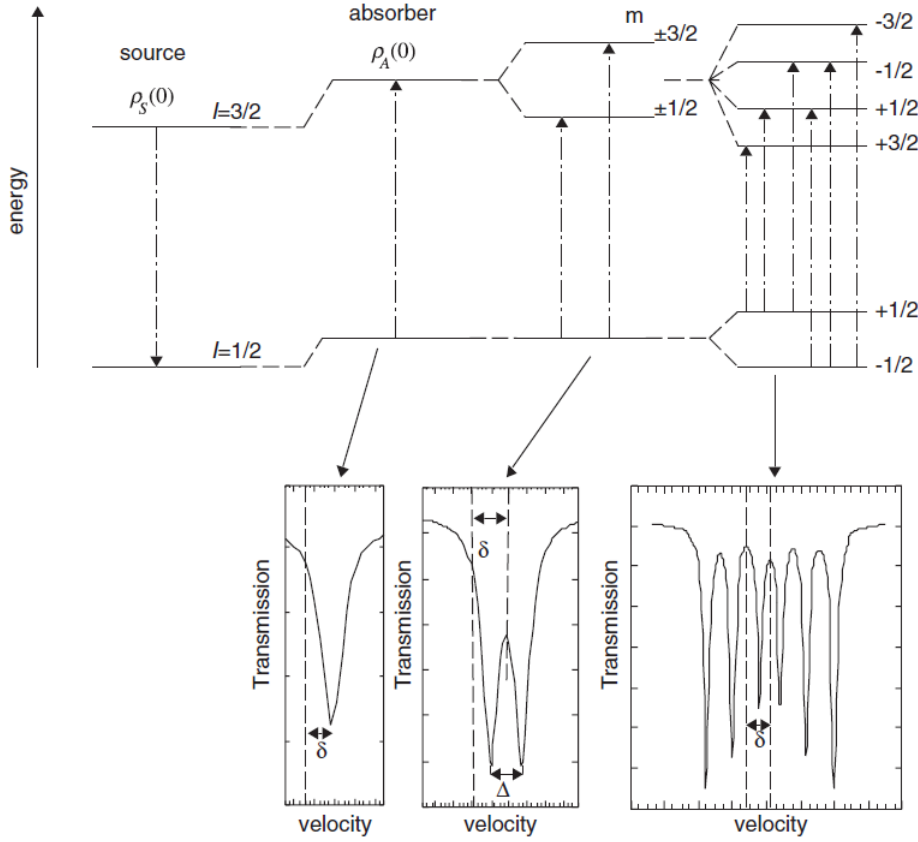


Figure 1.4.: Schematic representation of the hyperfine interactions in the case of a transition $\frac{1}{2} \rightarrow \frac{3}{2}$, like that of ^{57}Fe .

The second perturbation of the nuclear levels is caused by the interaction between the nuclear quadrupole moment and the EFG at the nucleus created by the surrounding electron charge density. As a result, the Mössbauer spectrum will consist of two lines, called a doublet. The isomer shift in this case is measured at the center of the doublet. The separation in energy of the doublet is expressed by Δ , which can be evaluated from Eq. (1.19) for the $\frac{1}{2} \rightarrow \frac{3}{2}$ transition as:

$$\Delta = \frac{1}{2}eQV_{zz} \left(1 + \frac{1}{3}\eta^2\right)^{\frac{1}{2}} \quad (1.26)$$

A third perturbation of the nuclear energy levels occurs in the presence of a magnetic field and yields different energies with regard to the orientations of the nuclear magnetic moment m_I relative to the field direction. Each nuclear level of non-zero spin is shifted into $2I + 1$ sub-levels reached by shifting it by $E_m = -g\mu_N B m_I$ (see Eq. (1.21)).

For example, in the case of iron, the ground level will undergo a symmetric splitting ($I = 1/2, m_I = +1/2, m_I = -1/2$) and the first excited state is split into four sub-levels ($I = 3/2, m_I = +3/2, m_I = +1/2, m_I = -1/2, m_I = -3/2$). Among the eight possible transitions between the two sub-levels of the ground state and the four sub-levels of the excited state only six are allowed by the quantum mechanical selection rule, and the resonance spectra consist of six lines or a sextet. The isomer shift is measured at the center of the sextet (Fig. 1.4). And B is proportional to the difference between the positions of two lines of the spectrum; the outermost ones are generally considered in the data analysis for better precision [69].

A typical spectrum measured in transmission, is shown in Figure 1.5. This measurement was done in a constant acceleration spectrometer, with a $^{57}\text{Co}(\text{Pd})$ source, to a normal pressure (AM) synthesized sample $\text{Fe}_{0.5}\text{Cu}_{0.5}\text{Ba}_2\text{YCu}_2\text{O}_{7.24}$ [39]. The line positions in this case are directly related with the electrical hyperfine interactions (IS and Electric Quadrupole). These positions are commonly expressed in mm/s ; in correspondence with the energy increase of the gamma quanta that is produced by the transducer movement. In the more simple case of the Nuclear Quadrupole Hyperfine Interaction effect, the ^{57}Fe atoms are occupying a single crystallographic position, possessing a unique valency state in a perfect crystal. In that way, all the ^{57}Fe nuclei that are located in this site experience an single type of Electrostatic Hyperfine Interaction. But in this case (see Figure 1.5) there are at least three possible ^{57}Fe occupation sites.

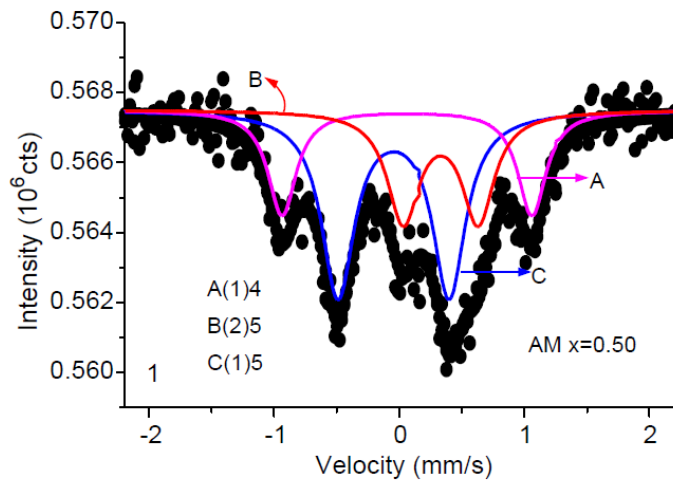


Figure 1.5.: Room-temperature transmission Mössbauer spectra of the normal pressure (AM) sample $\text{Fe}_{0.5}\text{Cu}_{0.5}\text{Ba}_2\text{YCu}_2\text{O}_{7.24}$ measured in [39]. The notation $D(i)n$, in the figure, denotes that in the experiment was considered that the Fe occupies the $\text{Cu}(i)$ site with n -fold oxygen coordination and it is associated with double D .

1.4.2. Perturbed angular correlation spectroscopy

The Perturbed Angular Correlation (PAC) spectroscopy is based on the hyperfine interaction of the nucleus, similar to the Mössbauer effect spectroscopy, studying the change of the angular correlation between those gamma quanta emitted successively in the nucleus deexcitation.

If one has a nucleus that decays via a $\gamma - \gamma$ cascade, as ^{111}Cd (see figure 1.6), the conservation of the angular momentum implies that the direction of emission of the second gamma ray is strongly correlated with the direction of the first one.

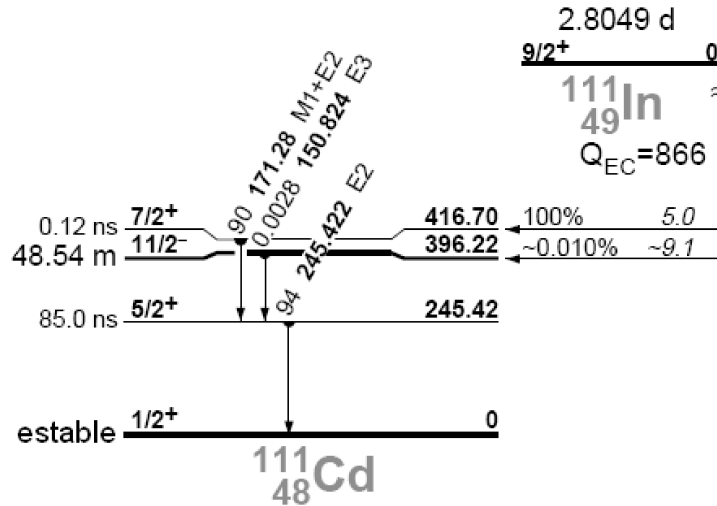


Figure 1.6.: $^{111}\text{In}(^{111}\text{Cd})$ disintegration scheme.

When an EFG exists in the nucleus, a state with half spin I can split in $I + \frac{1}{2}$ sub-states, as is shown in section 1.2.2. These states can be repopulated after the emission of the first gamma γ_1 , which is equivalent to a nuclear spin reorientation. In the semi-classic framework this effect is known as the Larmor precession around the EFG direction. As a result of this precession a correlation between the direction of emission of the first gamma quanta and the second one γ_2 is established and is characterized by the angle between both directions. This angular correlation can be expressed as the probability in time $W(\theta, t)$ that γ_2 is emitted in an angle θ with regard to γ_1 :

$$W(\theta, t) = \frac{1}{\tau_N} \exp\left(-\frac{t}{\tau_N}\right) \left[1 + \sum_{k=2,4,\dots}^{k_{max}} A_k G_k(t) P_k \cos(\theta) \right] \quad (1.27)$$

where $P_k \cos(\theta)$ are the Legendre polynomials, A_k the time independent anisotropy parameters that describe the spatial correlation, and τ_N is the half-time of the intermediate nuclear state. G_k has implicit the angular correlation perturbation and it is what is measured in the experiments. Nevertheless, this is feasible only when the intermediate state has a relatively large life-time (> 1 ns).

In Eq. (1.27) the anisotropy terms A_1 and A_3 are not included in the expansion due to the parity conservation in the gamma transitions. Also, the term A_4 is small compared to A_2 and it is usually rejected in the measurements. The term A_2 depends on the properties of the nucleus and could be used as an experimental calibration variable, so that it keeps information about the geometric effects (like the sample size and the solid angle with the detector) and the absorption of the gamma rays in the sample. Once it is determined for a given configuration, it could be taken as a fixed parameter in the measurements. This way, the angular correlation expressed by Eq. (1.27) is reduced to:

$$W(\theta, t) = \frac{1}{\tau_N} \exp\left(-\frac{t}{\tau_N}\right) [1 + A_2 G_2(t) P_2 \cos(\theta)] \quad (1.28)$$

The perturbation function $G_2(t)$ is used to describe the gamma quanta angular correlation changes when the nucleus interacts with the external EFG. For a polycrystalline sample, it can be expressed as:

$$G_2(t) = S_{20}(\eta) + \sum_{i=1}^3 S_{2i}(\eta) \cos(\omega_i t) \Delta \quad (1.29)$$

where ω_i represents the interaction frequencies corresponding to the transitions that take place during the life-time of the intermediate state (when the new sub-states created by the EFG action are repopulated). They are related to the differences of the intermediate states by the expression $\omega_i = \Delta E_i / \hbar$. The S_{2i} coefficients are the interaction frequency amplitudes obtained from the Fourier transform of the spectrum of both gamma coincidences, and Δ is the line form factor that is related to the coupling quadrupole constant ν_Q .

The Hamiltonian 1.19 allows, sometimes only in a numeric way, to obtain the difference in energy among the spin sublevels I of a nuclear state when an EFG exists, as a function of its main component V_{zz} . Through the PAC measurements these energy differences will be obtained as a function of the mentioned precession frequencies ω_i , so that it is possible to find out the value of the EFG at the nucleus position. Each one of the frequencies will

be a multiple of the quadrupole frequency ω_Q value, which is proportional to V_{zz} [70]:

$$\omega_Q = \frac{eQV_{zz}}{4I(2I-1)\hbar} \quad (1.30)$$

The quadrupole frequency in other ways is also defined as [70]:

$$\nu_Q = \frac{eQV_{zz}}{h} \quad (1.31)$$

where Q is the nuclear quadrupole moment, I , the spin of the intermediate level and e the proton electric charge. The magnitude ν_Q is the one that is usually measured in the PAC experiments and correlated with the EFG present at the probe nucleus.

Chapter 2.

Electronic structure calculation method

2.1. Quantum many body problem

The microscopic description of the physical and chemical properties of a material is a complex problem. In general, it should represent the collection of atoms interacting via forces that derive from some potential field. This ensemble of particles may be isolated (molecules and clusters), extended (solids, surfaces, wires, and liquids), or a combination of both (molecules in solution). However, in all cases we can unambiguously describe the system by a number of nuclei and electrons interacting through Coulombic (electrostatic) forces. Formally, the Hamiltonian of such a system can be separated in the following terms:

$$\hat{H} = \hat{T}_n + \hat{T}_e + \hat{V}_{nn} + \hat{V}_{ee} + \hat{V}_{ne} \quad (2.1)$$

where \hat{T}_n and \hat{T}_e are the kinetic energy operators of nuclei and electrons respectively, \hat{V}_{nn} represent the repulsive Coulomb interaction between the nuclei and \hat{V}_{ee} the same for electrons, while \hat{V}_{ne} is the potential energy of the electrons in the field of nuclei. These

terms can be written in the following general form:

$$\begin{aligned}
\hat{T}_n &= - \sum_{I=1}^P \frac{\hbar^2}{2M_I} \nabla_I^2 \\
\hat{T}_e &= - \sum_{i=1}^N \frac{\hbar^2}{2m_e} \nabla_i^2 \\
\hat{V}_{nn} &= \frac{1}{8\pi\epsilon_0} \sum_{I=1}^P \sum_{J \neq I}^P \frac{Z_I Z_J e^2}{|\mathbf{R}_I - \mathbf{R}_J|} \\
\hat{V}_{ee} &= \frac{1}{8\pi\epsilon_0} \sum_{i=1}^N \sum_{j \neq i}^N \frac{e^2}{|\mathbf{r}_i - \mathbf{r}_j|} \\
\hat{V}_{ne} &= - \frac{1}{4\pi\epsilon_0} \sum_{I=1}^P \sum_{i=1}^N \frac{Z_I e^2}{|\mathbf{R}_I - \mathbf{r}_i|}
\end{aligned} \tag{2.2}$$

where $\mathbf{R} = \{\mathbf{R}_I\}$, $I = 1 \dots P$, is a set of P nuclear coordinates, and $\mathbf{r} = \{\mathbf{r}_i\}$, $i = 1 \dots N$, is a set of N electronic coordinates. Z_I and M_I are the P nuclear charges and masses, respectively; and m_e is the electron mass.

Electrons are fermions, so that the total electronic wave function must be antisymmetric with respect to exchange of two electrons. Nuclei can be fermions, bosons or distinguishable particles, according to the particular problem under examination. In principle, all the properties can be derived by solving the time independent Schrödinger equation:

$$\hat{H}\Psi_i(\mathbf{r}, \mathbf{R}) = E_i\Psi_i(\mathbf{r}, \mathbf{R}) \tag{2.3}$$

where E_i are the energy eigenvalues and $\Psi_i(\mathbf{r}, \mathbf{R})$ are the corresponding eigenstates, or wave functions.

In practice, this problem is almost impossible to treat in a full quantum mechanical framework. Only in a few cases a complete analytic solution is available, and numerical solutions are also limited to a very small number of particles. There are several features that contribute to this difficulty. First, this is a multicomponent *many-body* system, where each component (each nuclear species and the electrons) obey a particular statistics. Moreover, the complete wave function cannot be easily factorized because of Coulombic correlations. In other words, the full Schrödinger equation cannot be easily decoupled into a set of equations so that, in general, we have to deal with $(3P + 3N)$ coupled

degrees of freedom. The dynamics is an even more difficult problem. The usual choice is to resort to some sensible approximations.

2.2. Born-Oppenheimer approximation

The first observation is that the time scale associated to the motion of the nuclei is usually much slower than that associated to electrons. In fact, the small mass of the electrons as compared to that of the protons means that their velocity is much larger. Then, with this assumption the ions are in a stationary configuration and the electrons will be in instantaneous equilibrium with them. This is known as the Born-Oppenheimer approximation and can be cast in a formal mathematical framework by proposing a solution to Eq. (2.3) of the following form [71, 72]:

$$\Psi(\mathbf{R}, \mathbf{r}) = \Theta_n(\mathbf{R})\Phi_n(\mathbf{R}, \mathbf{r}) \quad (2.4)$$

where $\Phi_n(\mathbf{R}, \mathbf{r})$ are the eigenstates of the electronic Hamiltonian and $\Theta_n(\mathbf{R})$ are the nuclear wave function. The Schrödinger equation of the electrons corresponding to a particular nuclear configuration is written as follows:

$$\hat{H}_e\Phi_n(\mathbf{R}, \mathbf{r}) = \varepsilon_n\Phi_n(\mathbf{R}, \mathbf{r}) \quad (2.5)$$

where,

$$\hat{H}_e = \hat{T}_e + \hat{V}_{ee} + \hat{V}_{ext} \quad (2.6)$$

Here, \hat{V}_{ext} is the potential energy of the electrons moving in the potential of the nuclei, represented as \hat{V}_{ne} in Eq. 2.1. In this partial differential equation on the \mathbf{r} variables, \mathbf{R} enters as a parameter. This expansion, which is always mathematically possible, is called the expansion in the *adiabatic basis*. Eq. (2.5) has to be solved for all nuclear configurations where the nuclear wave function is non-zero.

The quantum *many-body* problem obtained after the Born-Oppenheimer approximation is much simpler than the original one, but still this is very difficult to solve. Several methods exist to reduce Eq. (2.5) to an approximate but tractable form. One of the most important is the Hartree-Fock method (HF) [71], which is routinely used as a

starting point for more elaborated calculations like Møller-Plesset perturbation theory or by configuration interaction method (CI).

Parallel to the development of this line in electronic structure theory, Thomas and Fermi proposed, at about the same time as Hartree (1927-1928), that the full electronic density was the fundamental variable of the *many-body* problem, and derived a differential equation for the density without resorting to one-electron orbitals [73, 74]. The Thomas-Fermi approximation was actually too crude because it did not include exchange and correlation effects, and was also unable to sustain bound states because of the approximation used for the kinetic energy of the electrons. However, it set up the basis for the later development of Density Functional Theory (DFT).

2.3. Density functional theory method

The total energy of an inhomogeneous system composed by N interacting electrons is given by the following expectation value [71, 72]:

$$E = \langle \Phi | \hat{T} + \hat{V}_{ext} + \hat{V}_{ee} | \Phi \rangle = \langle \Phi | \hat{T} | \Phi \rangle + \langle \Phi | \hat{V}_{ext} | \Phi \rangle + \langle \Phi | \hat{V}_{ee} | \Phi \rangle \quad (2.7)$$

where $|\Phi\rangle$ is the N -electron wave function. This wave function has to include correlations amongst electrons, and its general form is basically unknown. \hat{T} is the kinetic energy operator, \hat{V}_{ext} is the interaction with an external field, and \hat{V}_{ee} is the electron-electron interaction. The analysis will focus on this latter term, which introduces the *many-body* effects.

$$V_{ee} = \langle \Phi | \hat{V}_{ee} | \Phi \rangle = \left\langle \Phi \left| \frac{1}{2} \sum_{i=1}^N \sum_{j \neq i}^N \frac{1}{|\mathbf{r}_i - \mathbf{r}_j|} \right| \Phi \right\rangle = \iint \frac{\rho_2(\mathbf{r}, \mathbf{r}')}{|\mathbf{r} - \mathbf{r}'|} d\mathbf{r} d\mathbf{r}' \quad (2.8)$$

with

$$\rho_2(\mathbf{r}, \mathbf{r}') = \frac{1}{2} \langle \Phi | \hat{\Psi}^\dagger(\mathbf{r}) \hat{\Psi}^\dagger(\mathbf{r}') \hat{\Psi}(\mathbf{r}') \hat{\Psi}(\mathbf{r}) | \Phi \rangle \quad (2.9)$$

the two-body density matrix expressed in real space, being $\hat{\Psi}$ and $\hat{\Psi}^\dagger$ the destruction and creation operators for electrons, which obey the anticommutation relations $\{\hat{\Psi}(\mathbf{r}), \hat{\Psi}^\dagger(\mathbf{r}')\} = \delta(\mathbf{r} - \mathbf{r}')$. Defining the two-body direct correlation function $g(\mathbf{r}, \mathbf{r}')$ in

the following way:

$$\rho_2(\mathbf{r}, \mathbf{r}') = \frac{1}{2} \rho_1(\mathbf{r}, \mathbf{r}) \rho_1(\mathbf{r}', \mathbf{r}') g(\mathbf{r}, \mathbf{r}') \quad (2.10)$$

where $\rho_1(\mathbf{r}, \mathbf{r}') = \langle \Phi | \Psi^\dagger(\mathbf{r}) \Psi(\mathbf{r}') | \Phi \rangle$ is the one-body density matrix (in real space), whose diagonal elements $\rho(\mathbf{r}) = \rho_1(\mathbf{r}, \mathbf{r})$ represent the electron density. With this definition, the electron-electron interaction can be written as:

$$V_{ee} = \frac{1}{2} \iint \frac{\rho(\mathbf{r}) \rho(\mathbf{r}')}{|\mathbf{r} - \mathbf{r}'|} d\mathbf{r} d\mathbf{r}' + \frac{1}{2} \iint \frac{\rho(\mathbf{r}) \rho(\mathbf{r}')}{|\mathbf{r} - \mathbf{r}'|} [g(\mathbf{r}, \mathbf{r}') - 1] d\mathbf{r} d\mathbf{r}' \quad (2.11)$$

The first term is the classical electrostatic interaction energy corresponding to a charge distribution $\rho(\mathbf{r})$. The second term includes correlation effects of both, classical and quantum origin. Basically, $g(\mathbf{r}, \mathbf{r}')$ takes into account the fact that the presence of an electron at \mathbf{r} excludes the possibility that a second electron comes to a position \mathbf{r}' very close to \mathbf{r} , because of the Coulomb repulsion. In other words, the probability of finding two electrons (two particles with charges of the same sign, in the general case) is reduced with respect to the probability of finding them at infinite distance. This is the case at the classical level, and it is further modified at the quantum level. Purely quantum exchange further decreases this probability in the case of electrons having the same spin projection.

To understand the effect of exchange, let us imagine that we stand on an electron with spin \uparrow , and we look at the density of the other $(N - 1)$ electrons. The Pauli principle forbids the presence of electrons with spin \uparrow at the origin, but it says nothing about electrons with spin \downarrow , which can be at the origin. Therefore:

$$g_x(\mathbf{r}, \mathbf{r}') \rightarrow \frac{1}{2} \quad \text{for } \mathbf{r} \rightarrow \mathbf{r}' \quad (2.12)$$

If one postulates a total wave function of the form of a Slater determinant, the electron-electron interaction can be rewritten as:

$$V_{ee} = \frac{1}{2} \iint \frac{\rho(\mathbf{r}) \rho(\mathbf{r}')}{|\mathbf{r} - \mathbf{r}'|} d\mathbf{r} d\mathbf{r}' - \frac{1}{2} \iint \frac{\rho(\mathbf{r}) \rho(\mathbf{r}')}{|\mathbf{r} - \mathbf{r}'|} \left[-\frac{\rho_1^2(\mathbf{r}, \mathbf{r}')}{2\rho(\mathbf{r})\rho(\mathbf{r}')} \right] d\mathbf{r} d\mathbf{r}' \quad (2.13)$$

meaning that the exact expression for the exchange depletion (also called exchange hole) in the HF limit is:

$$g_X(\mathbf{r}, \mathbf{r}') = 1 - \frac{1}{2} \frac{\rho_1^2(\mathbf{r}, \mathbf{r}')}{\rho(\mathbf{r})\rho(\mathbf{r}')} \quad (2.14)$$

The calculation of the correlation hole ($g_C(\mathbf{r}, \mathbf{r}') = g(\mathbf{r}, \mathbf{r}') - g_X(\mathbf{r}, \mathbf{r}')$) is a major problem in *many-body* theory and, up to the present, it is an open problem in the general case of an inhomogeneous electron gas. The exact solution is known numerically, and also in some analytic derivations, for the homogeneous electron gas. There are several approximations that go beyond the homogeneous limit by including slowly varying densities through its spatial gradients (gradient corrections), and others [71].

Finally, the energy of a *many-body* electronic system can be written as:

$$E = T + V_{ext} + \frac{1}{2} \iint \frac{\rho(\mathbf{r})\rho(\mathbf{r}')}{|\mathbf{r} - \mathbf{r}'|} d\mathbf{r}d\mathbf{r}' + E_X + E_C \quad (2.15)$$

where

$$V_{ext} = \sum_{I=1}^P \left\langle \Phi \left| \sum_{i=1}^N v_{ext}(\mathbf{r}_i - \mathbf{R}_I) \right| \Phi \right\rangle = \sum_{I=1}^P \int \rho(\mathbf{r}) v_{ext}(\mathbf{r} - \mathbf{R}_I) d\mathbf{r} \quad (2.16)$$

$$T = \left\langle \Phi \left| -\frac{\hbar^2}{2m_e} \sum_{i=1}^N \nabla_i^2 \right| \Phi \right\rangle = -\frac{\hbar^2}{2m_e} \int [\nabla_{\mathbf{r}}^2 \rho_1(\mathbf{r}, \mathbf{r}')]_{\mathbf{r}'=\mathbf{r}} d\mathbf{r} \quad (2.17)$$

and E_X and E_C are the exchange and correlation energies, respectively.

2.3.1. The Hohenberg and Kohn theorems

In 1964, P. Hohenberg and W. Kohn [75] formulated and proved a theorem supporting the former ideas, which were first proposed by Thomas and Fermi. The theorem is divided into two parts:

Theorem: *The external potential $v_{ext}(\mathbf{r})$ is unequivocally determined by the electronic density $\rho(\mathbf{r})$, except for a trivial additive constant.*

Corollary: *Since $\rho(\mathbf{r})$ unequivocally determines $v_{ext}(\mathbf{r})$, then it also determines the ground state wave function Ψ_{GS} .*

Theorem: Let $\tilde{\rho}(\mathbf{r})$ be a non-negative density normalized to N . Then: $E_0 < E_v[\tilde{\rho}]$, for

$$E_v[\rho] = T[\rho] + U[\rho] + \int \rho(\mathbf{r})v(\mathbf{r})d\mathbf{r} \quad (2.18)$$

with

$$U[\rho] = \frac{1}{2} \iint \frac{\rho(\mathbf{r})\rho(\mathbf{r}')}{|\mathbf{r} - \mathbf{r}'|} d\mathbf{r}d\mathbf{r}' + E_X[\rho] + E_C[\rho] \quad (2.19)$$

The inequality follows from Rayleigh-Ritz's variational principle for the wave function, but applied to the electronic density. Therefore, the variational principle says:

$$\delta \left\{ E_v[\rho] - \mu \left(\int \rho(\mathbf{r})d\mathbf{r} - N \right) \right\} = 0 \quad (2.20)$$

so that a general Thomas-Fermi-like equation is obtained [71]:

$$\mu = \frac{\delta E_v[\rho]}{\delta \rho} = v_{ext}(\mathbf{r}) + \frac{\delta F[\rho]}{\delta \rho} \quad (2.21)$$

where $F[\rho] = T[\rho] + U[\rho]$. The knowledge of $F[\rho]$ implies the solution of the ground state density. It has to be remarked that $F[\rho]$ is a universal functional which does not depend explicitly on the external potential. It depends only on the electronic density. In the Hohenberg-Kohn formulation, $F[\rho] = \langle \Psi | \hat{T} + \hat{U} | \Psi \rangle$, where Ψ is the ground state wave function. These two theorems are the basis of the *density functional theory* (DFT).

Following the Hohenberg-Kohn theorem, the electronic density determines the external potential, but the density needs to corresponded to some antisymmetric wave function derived from a potential, which is not always the case. However, DFT can be reformulated in such a way that this is not necessary [71]. It can define

$$F[\rho] = \min_{\{\Psi\} \rightarrow \rho} \left\{ \langle \Psi | \hat{T} + \hat{U} | \Psi \rangle \right\} \quad (2.22)$$

for non-negative ρ such that $\int \rho(\mathbf{r})d\mathbf{r} = N$ and $\int |\nabla \rho^{1/2}(\mathbf{r})|^2 d\mathbf{r} < \infty$, arising from an antisymmetric wave function. In other words, the search is performed in the subspace of all the antisymmetric Ψ that give rise to the same density ρ .

DFT is exact for the electronic ground state provided that $F[\rho]$ is known. However, it does not say anything about (*many-body*) excited states. To solve the excited states is a hard problem that is currently still researched [71].

2.3.2. The Kohn-Sham equations

A reasonably good description of the electron–electron interaction potential U can be done by separating the electrostatic (classical Coulomb energy), exchange and correlation contributions. The biggest difficulty is to deal with the correlation. This is, in fact, an active field of research which has produced significant improvements in the 90’s. On the contrary, there is a problem with the expression of the kinetic energy $\langle \Psi | \hat{T} | \Psi \rangle$ in terms of the electronic density.

In 1965, W. Kohn and L. Sham [76] proposed the idea of replacing the kinetic energy of the interacting electrons with that of an equivalent non-interacting system, because the latter can be easily calculated. Any density $\rho(r)$ that derives from an antisymmetric wave function can be written as:

$$\rho(\mathbf{r}) = \sum_{i=1}^{\infty} \sum_{s=1}^2 n_{i,s} |\varphi_{i,s}(\mathbf{r})|^2 \quad (2.23)$$

where $\{\varphi_{i,s}(\mathbf{r})\}$ are natural spin orbitals, and $\{n_{i,s}\}$ are the occupation numbers of these orbitals. In that case, the kinetic energy can be written as

$$T = \sum_{s=1}^2 \sum_{i=1}^{\infty} n_{i,s} \left\langle \varphi_{i,s} \left| -\frac{\hbar^2}{2m_e} \nabla^2 \right| \varphi_{i,s} \right\rangle. \quad (2.24)$$

These occupation numbers are actually an artifact arising from the fact that the density is written in terms of a set of single-particle orbitals associated with non-interacting fermions. The interacting *many-body* wave function has to be identified with an occupation N , and not with a set of occupation numbers. However, bearing in mind this conceptual difference, we can always think of $n_{i,s}$ as the occupation of orbital i and spin s . For the moment we shall suppose that the equivalent non-interacting system, *i.e.* a system of non-interacting fermions whose density coincides with that of the interacting system, does exist. This can be called the *non-interacting reference system* of density

$\rho(\mathbf{r})$, which is described by the Hamiltonian

$$\hat{H}_R = \sum_{i=1}^{N_s} \sum_{s=1}^2 \left(-\frac{\hbar^2}{2m_e} \nabla_i^2 + v_R(\mathbf{r}_i) \right) \quad (2.25)$$

with $N_s = N/2$. Here, the potential $v_R(\mathbf{r})$, or *reference potential*, is such that the ground state density of \hat{H}_R equals $\rho(\mathbf{r})$.

This Hamiltonian has no electron-electron interactions and, thus, its eigenstates can be expressed in the form of Slater determinants

$$\Psi_s(\mathbf{r}) = \frac{1}{\sqrt{N!}} SD[\varphi_{1,s}(\mathbf{r}_1)\varphi_{2,s}(\mathbf{r}_2) \cdots \varphi_{N_s,s}(\mathbf{r}_{N_s})] \quad (2.26)$$

where we have chosen, at $T = 0$ K, the occupation numbers to be 1 for $i \leq N_s$ ($s = 1, 2$), and 0 for $i > N_s$ ($s = 1, 2$). This means that the density is written as

$$\rho(\mathbf{r}) = \sum_{i=1}^{N_s} \sum_{s=1}^2 |\varphi_{i,s}(\mathbf{r})|^2 \quad (2.27)$$

while the kinetic term from Eq. 2.24 yields:

$$T_R[\rho] = \sum_{s=1}^2 \sum_{i=1}^{N_s} \left\langle \varphi_{i,s} \left| -\frac{\hbar^2}{2m_e} \nabla^2 \right| \varphi_{i,s} \right\rangle. \quad (2.28)$$

The single-particle orbitals $\{\varphi_{i,s}(\mathbf{r})\}$ are the N_s lowest eigenfunctions of $\hat{h}_R = -\frac{\nabla^2}{2} + v_R(\mathbf{r})$, *i.e.* $\hat{h}_R \varphi_{i,s}(\mathbf{r}) = \varepsilon_{i,s} \varphi_{i,s}(\mathbf{r})$.

With this definition, the density functional is rewritten in the following form:

$$E_{KS}[\rho] = T_R[\rho] + \int \rho(\mathbf{r}) v_{ext}(\mathbf{r}) d\mathbf{r} + \frac{1}{2} \iint \frac{\rho(\mathbf{r})\rho(\mathbf{r}')}{|\mathbf{r} - \mathbf{r}'|} d\mathbf{r}d\mathbf{r}' + E_X[\rho] + \tilde{E}_C[\rho] \quad (2.29)$$

where the fact that $T_R[\rho]$ is the kinetic energy of the non-interacting reference system implies that the correlation piece of the true kinetic energy has been ignored, and has to be taken into account somewhere else. In practice this is done by redefining the correlation energy functional in such a way as to include kinetic correlations. For that reason the corresponding term is now expressed as \tilde{E}_C in Eq. 2.29.

In this way the density functional is expressed in terms of $N = N_\uparrow + N_\downarrow$ orbitals. The electron density is parametrized with a set of N orbitals, and the problem consist of

minimizing the energy functional by applying the variational principle on the orbitals instead of the density. In principle these orbitals are a mathematical object constructed in order to render the problem more tractable, and do not have a physical meaning by themselves, except in terms of the density. In practice, however, it is customary to think of them as single-particle physical eigenstates. Only in the case that correlations are weak, this intuitive idea makes sense.

Now, expression (2.29) could be minimized with respect to $\{\varphi_{i,s}(\mathbf{r})\}$ by taking into account that the orbitals have to be orthogonal, *i.e.* $\int \varphi_{i,s}^*(\mathbf{r})\varphi_{j,u}(\mathbf{r})d\mathbf{r} = \delta_{ij}\delta_{su}$, because they are the N lowest eigenfunctions of a unique potential. This constraints enter into the minimization problem as Lagrange multipliers:

$$\Omega_{KS}[\{\varphi_{i,s}(\mathbf{r})\}] = E_{KS}[\{\varphi_{i,s}(\mathbf{r})\}] - \sum_{s=1}^2 \sum_{i=1}^{N_s} \sum_{j=1}^{N_s} \varepsilon_{ij,s} \int \varphi_{i,s}^*(\mathbf{r})\varphi_{j,s}(\mathbf{r})d\mathbf{r} \quad (2.30)$$

Minimizing this functional with respect to each $\varphi_{i,s}(\mathbf{r})$ gives the following set of coupled differential equations:

$$\begin{aligned} \frac{\delta\Omega_{KS}[\{\varphi_{i,s}(\mathbf{r})\}]}{\delta\varphi_{i,s}^*(\mathbf{r})} &= \left\{ -\frac{\hbar^2}{2m_e}\nabla^2 + v_{ext}(\mathbf{r}) + \int \frac{\rho(\mathbf{r}')}{|\mathbf{r}-\mathbf{r}'|}d\mathbf{r}' + \frac{\delta E_{XC}[\rho]}{\delta\rho} \right\} \varphi_{i,s}(\mathbf{r}) \\ &- \sum_{j=1}^{N_s} \varepsilon_{ij,s}\varphi_{j,s}(\mathbf{r}) = 0 \end{aligned} \quad (2.31)$$

The effective potential (see below) is hermitian and, therefore, the matrix $\varepsilon_{ij,s}$ is symmetric and can be diagonalized by a unitary transformation that keeps invariant the total wave function (the Slater determinant), and thus the density. Such a procedure brings us to the final result, which are the well-known, self-consistent Kohn-Sham equations:

$$\left\{ -\frac{\hbar^2}{2m_e}\nabla^2 + v_{eff}(\mathbf{r}) \right\} \varphi_{i,s}(\mathbf{r}) = \varepsilon_{i,s}\varphi_{j,s}(\mathbf{r}) \quad (2.32)$$

where the effective potential $v_{eff}(\mathbf{r})$ is defined as:

$$v_{eff}(\mathbf{r}) = v_{ext}(\mathbf{r}) + \int \frac{\rho(\mathbf{r}')}{|\mathbf{r}-\mathbf{r}'|}d\mathbf{r}' + \mu_{XC}[\rho] \quad (2.33)$$

and the electron density is constructed with the solutions of Kohn-Sham equations

$$\rho(\mathbf{r}) = \sum_{i=1}^{N_s} \sum_{s=1}^2 |\varphi_{i,s}(\mathbf{r})|^2 \quad (2.34)$$

The exchange correlation potential $\mu_{XC}[\rho]$ defined above is simply the functional derivative of the exchange-correlation energy $\delta E_{XC}[\rho]/\delta\rho$.

The solution of Kohn-Sham equations has to be obtained by an iterative procedure, in the same way as for Hartree and Hartree-Fock equations [71]. As in these methods, the total energy cannot be written simply as the sum of the eigenvalues $\varepsilon_{i,s}$, but double counting terms have to be subtracted:

$$E_{KS}[\rho] = \sum_{i=1}^{N_s} \sum_{s=1}^2 \varepsilon_{i,s} - \frac{1}{2} \iint \frac{\rho(\mathbf{r})\rho(\mathbf{r}')}{|\mathbf{r} - \mathbf{r}'|} d\mathbf{r}d\mathbf{r}' + \left\{ E_{XC}[\rho] - \int \rho(\mathbf{r})\mu_{XC}[\rho]d\mathbf{r} \right\} \quad (2.35)$$

This theory is able to solve the complicated *many-body* electronic ground state problem by mapping the *many-body* Schrödinger equation into a set of N coupled single-particle equations. Therefore, given an external potential, we are in a position to find the electron density, the energy, and any ground state property we want to (e.g. stress, phonon's, etc.). The density of the non-interacting reference system is equal to that of the true interacting system. Up to now the theory is exact, all the ignorance about the *many-fermion* problem has been displaced to the $\tilde{E}_C[\rho]$ term, while the remaining terms in the energy are well-known. In the next section we are going to discuss the exchange and correlation functionals.

2.3.3. The exchange-correlation functional

We have shifted the ignorance about the quantum *many-body* problem towards the exchange and correlation functional $E_{XC}[\rho]$. If we knew the exact expression for the kinetic energy including correlation effects, *i.e.* $T[\rho]$, then

$$E_{XC}[\rho] = \frac{1}{2} \iint \frac{\rho(\mathbf{r})\rho(\mathbf{r}')}{|\mathbf{r} - \mathbf{r}'|} [g(\mathbf{r}, \mathbf{r}') - 1] d\mathbf{r}d\mathbf{r}' \quad (2.36)$$

Since we are using the uncorrelated expression for the kinetic energy, *i.e.* the one for non-interacting fermions $T_R[\rho]$, we have to use a slightly different expression:

$\tilde{E}_{XC}[\rho] = E_{XC}[\rho] + T[\rho] - T_R[\rho]$. It can be shown that the kinetic contribution to the correlation energy (the kinetic contribution to exchange is just Pauli's principle, which is already contained in $T_R[\rho]$ and in the density when adding up the contributions of the N lowest eigenstates) can be taken into account by averaging the pair correlation function $g(\mathbf{r}, \mathbf{r}')$ over the strength of the electron-electron interaction, *i.e.*

$$\tilde{E}_{XC}[\rho] = \frac{1}{2} \iint \frac{\rho(\mathbf{r})\rho(\mathbf{r}')}{|\mathbf{r} - \mathbf{r}'|} [\tilde{g}(\mathbf{r}, \mathbf{r}') - 1] d\mathbf{r}d\mathbf{r}' \quad (2.37)$$

where

$$\tilde{g}(\mathbf{r}, \mathbf{r}') = \int_0^1 g_\lambda(\mathbf{r}, \mathbf{r}') d\lambda \quad (2.38)$$

and $g_\lambda(\mathbf{r}, \mathbf{r}')$ is the pair correlation function corresponding to the Hamiltonian $\hat{H} = \hat{T} + \hat{U} + \lambda \hat{V}_{ee}$ [77]. If we separate the exchange and correlation contributions, then:

$$\tilde{g}(\mathbf{r}, \mathbf{r}') = 1 - \frac{1}{2} \frac{\rho_1^2(\mathbf{r}, \mathbf{r}')}{\rho(\mathbf{r})\rho(\mathbf{r}')} + \tilde{g}_C(\mathbf{r}, \mathbf{r}') \quad (2.39)$$

with $\rho_1(\mathbf{r}, \mathbf{r}')$ the one-body density matrix, which in general is a non-diagonal operator. The diagonal elements of it constitute the electron density. For the homogeneous electron gas the expression for ρ_1 is well-known, so that the exchange pair correlation assumes the analytic closed form

$$g_X(\mathbf{r}, \mathbf{r}') = g_X(|\mathbf{r} - \mathbf{r}'|) = 1 - \frac{9}{2} \left(\frac{j_1(k_F |\mathbf{r} - \mathbf{r}'|)}{k_F |\mathbf{r} - \mathbf{r}'|} \right)^2 \quad (2.40)$$

where $j_1(x) = [\sin(x) - x \cos(x)]/x^2$ is the spherical Bessel function of order 1 and k_F is the Fermi momentum. We are now going to define the exchange-correlation hole $\tilde{\rho}_{XC}(\mathbf{r}, \mathbf{r}')$ in the following form:

$$\tilde{E}_{XC}[\rho] = \frac{1}{2} \iint \frac{\rho(\mathbf{r})\tilde{\rho}_{XC}(\mathbf{r}, \mathbf{r}')}{|\mathbf{r} - \mathbf{r}'|} d\mathbf{r}d\mathbf{r}' \quad (2.41)$$

or

$$\tilde{\rho}_{XC}(\mathbf{r}, \mathbf{r}') = \rho(\mathbf{r}') [\tilde{g}(\mathbf{r}, \mathbf{r}') - 1] \quad (2.42)$$

This means that $\tilde{E}_{XC}[\rho]$ can be written as the interaction between the electronic charge distribution and the charge distribution that has been displaced by exchange

and correlation effects, *i.e.* by the fact that the presence of an electron at \mathbf{r} reduces the probability for a second electron to be at \mathbf{r}' , in the vicinity of \mathbf{r} . Actually, $\tilde{\rho}_{XC}(\mathbf{r}, \mathbf{r}')$ is the exchange-correlation hole averaged over the strength of the interaction, which takes into account kinetic correlations. The properties of $\tilde{g}(\mathbf{r}, \mathbf{r}')$ and $\tilde{\rho}_{XC}(\mathbf{r}, \mathbf{r}')$ are very interesting and instructive:

1. $\tilde{g}(\mathbf{r}, \mathbf{r}') = \tilde{g}(\mathbf{r}', \mathbf{r})$ (symmetry)
2. $\int \tilde{g}(\mathbf{r}, \mathbf{r}')\rho(\mathbf{r}')d\mathbf{r}' = \int \tilde{g}(\mathbf{r}, \mathbf{r}')\rho(\mathbf{r})d\mathbf{r} = N - 1$ (normalization)
3. $\int \tilde{\rho}_{XC}(\mathbf{r}, \mathbf{r}')d\mathbf{r}' = \int \tilde{\rho}_{XC}(\mathbf{r}, \mathbf{r}')d\mathbf{r} = -1$

This means that the exchange-correlation hole contains exactly *one* displaced electron. This sum rule is very important, and it has to be verified by any approximation used for $\tilde{\rho}_{XC}(\mathbf{r}, \mathbf{r}')$. If we separate the exchange and correlation contributions, it is easy to see that the displaced electron comes exclusively from the exchange part, and it is a consequence of the form in which the electron-electron interaction has been separated. In this way, the interaction of the electron with itself is exactly canceled by the exchange interaction of the full charge density with the displaced density. However, exchange is more than that. It is a nonlocal operator whose local component is minus the self-interaction. On the other hand, the correlation hole integrates to zero $\int \tilde{\rho}_C(r, r')dr' = 0$ so that the correlation energy corresponds to the interaction of the charge density with a neutral charge distribution [71].

The Local Density Approximation (LDA)

This has been for a long time the most widely used approximation to the exchange-correlation energy. It has been proposed in the seminal paper by Kohn and Sham, but the philosophy was already present in Thomas-Fermi theory [71]. The main idea is to consider the general inhomogeneous electronic systems as locally homogeneous, and then to use the exchange-correlation hole corresponding to the homogeneous electron gas for which there are very good approximations and also exact numerical (quantum Monte Carlo) results. This means:

$$\tilde{\rho}_{XC}^{LDA}(\mathbf{r}, \mathbf{r}') = \rho(\mathbf{r}) \{ \tilde{g}^h[|\mathbf{r} - \mathbf{r}'|, \rho(\mathbf{r})] - 1 \} \quad (2.43)$$

with $\tilde{g}^h[|\mathbf{r} - \mathbf{r}'|, \rho(\mathbf{r})]$ the pair correlation function of the homogeneous gas, which depends only on the distance between \mathbf{r} and \mathbf{r}' , evaluated at the density ρ^h which locally equals

$\rho(\mathbf{r})$. Within this approximation, the exchange-correlation energy density is defined as:

$$\epsilon_{XC}^{LDA}[\rho] = \frac{1}{2} \int \frac{\tilde{\rho}_{XC}^{LDA}(\mathbf{r}, \mathbf{r}')}{|\mathbf{r} - \mathbf{r}'|} d\mathbf{r}' \quad (2.44)$$

and the exchange-correlation energy becomes

$$E_{XC}^{LDA}[\rho] = \int \rho(\mathbf{r}) \epsilon_{XC}^{LDA}[\rho] d\mathbf{r}. \quad (2.45)$$

In general, the exchange-correlation energy density is not a functional of ρ . From its very definition it is clear that it has to be a non-local object, because it reflects the fact that the probability of finding an electron at \mathbf{r} depends on the presence of other electrons in the surroundings, through the exchange-correlation hole.

Looking at expression (2.43), it may seem that there is an inconsistency in the definition. The exact expression would indicate to take $\rho(\mathbf{r}')$ instead of $\rho(\mathbf{r})$. However, this would make of $\epsilon_{XC}^{LDA}[\rho]$ a non-local object which would depend on the densities at \mathbf{r} and \mathbf{r}' , and we want to parametrize it with the homogeneous gas, which is characterized by only one density. This is the essence of the LDA, and it is equivalent to postulate:

$$\tilde{g}(\mathbf{r}, \mathbf{r}') = \tilde{g}^h[|\mathbf{r} - \mathbf{r}'|, \rho(\mathbf{r})] \left(\frac{\rho(\mathbf{r})}{\rho(\mathbf{r}')} \right) \quad (2.46)$$

Therefore, there are in fact two approximations embodied in the LDA:

1. The exchange-correlation hole is centered at \mathbf{r} , and interacts with the electronic density at \mathbf{r} . The true exchange-correlation hole is actually centered at \mathbf{r}' instead of \mathbf{r} .
2. The pair correlation function (g) is approximated by that of the homogeneous electron gas of density $\rho(\mathbf{r})$ corrected by the density ratio $\rho(\mathbf{r})/\rho(\mathbf{r}')$ to compensate the fact that the LDA exchange-correlation hole is centered at \mathbf{r} instead of \mathbf{r}' .

The Local Spin Density Approximation

In magnetic systems or, in general, in cases where open electronic shells are involved, better approximations to the exchange-correlation functional can be obtained by introducing the two spin densities, $\rho_{\uparrow}(\mathbf{r})$ and $\rho_{\downarrow}(\mathbf{r})$, such that $\rho(\mathbf{r}) = \rho_{\uparrow}(\mathbf{r}) + \rho_{\downarrow}(\mathbf{r})$, and $\zeta(\mathbf{r}) = (\rho_{\uparrow}(\mathbf{r}) - \rho_{\downarrow}(\mathbf{r}))/\rho(\mathbf{r})$ is the magnetization density. The non-interacting kinetic energy

(2.28) splits trivially into *spin-up* and a *spin-down* contributions, and the external and Hartree potential depend on the full density $\rho(\mathbf{r})$, but the approximate XC functional (even if the exact functional should depend only on $\rho(\mathbf{r})$) will depend on both spin densities independently, $E_{XC} = E_{XC}[\rho_{\uparrow}(\mathbf{r}), \rho_{\downarrow}(\mathbf{r})]$. Kohn-Sham equations then read exactly as in (2.32), but the effective potential $v_{eff}(\mathbf{r})$ now acquires a spin index:

$$\begin{aligned} v_{eff}^{\uparrow}(\mathbf{r}) &= v_{ext}(\mathbf{r}) + \int \frac{\rho(\mathbf{r}')}{|\mathbf{r} - \mathbf{r}'|} d\mathbf{r}' + \frac{\delta E_{XC}[\rho_{\uparrow}(\mathbf{r}), \rho_{\downarrow}(\mathbf{r})]}{\delta \rho_{\uparrow}(\mathbf{r})} \\ v_{eff}^{\downarrow}(\mathbf{r}) &= v_{ext}(\mathbf{r}) + \int \frac{\rho(\mathbf{r}')}{|\mathbf{r} - \mathbf{r}'|} d\mathbf{r}' + \frac{\delta E_{XC}[\rho_{\uparrow}(\mathbf{r}), \rho_{\downarrow}(\mathbf{r})]}{\delta \rho_{\downarrow}(\mathbf{r})} \end{aligned}$$

The density given by expression (2.34) contains a double summation, over the spin states and over the number of electrons in each spin state, N_s . These later have to be determined according to the single-particle eigenvalues, by asking for the lowest $N = N_{\uparrow} + N_{\downarrow}$ to be occupied. This defines a Fermi energy ε_F , such that the occupied eigenstates have $\varepsilon_{i,s} < \varepsilon_F$.

In the case of non-magnetic systems $\rho_{\uparrow}(\mathbf{r}) = \rho_{\downarrow}(\mathbf{r})$, and everything reduces to the simple case of double occupancy of the single-particle orbitals, and then the calculations spare half of the computer time.

The equivalent of the LDA in spin-polarized systems is the *local spin density approximation* (LSDA), and it basically consists of replacing the XC energy density with a spin-polarized expression:

$$E_{XC}^{LSDA}[\rho_{\uparrow}(\mathbf{r}), \rho_{\downarrow}(\mathbf{r})] = \int [\rho_{\uparrow}(\mathbf{r}) + \rho_{\downarrow}(\mathbf{r})] \epsilon_{XC}^h[\rho_{\uparrow}(\mathbf{r}), \rho_{\downarrow}(\mathbf{r})] d\mathbf{r} \quad (2.47)$$

obtained, for instance, by interpolating between the fully-polarized and fully-unpolarized XC energy densities using an appropriate expression that depends on $\zeta(\mathbf{r})$ [78].

Generalized Gradient Approximations

Several works have been done to improve the LDA and construct better approximations. Undoubtedly, and probably because of its computational efficiency and its similarity to the LDA, the most popular approach has been to introduce semilocally the inhomogeneities of the density, by expanding $E_{XC}[\rho]$ as a series in terms of the density and its gradients. This approach, known as generalized gradient approximation (GGA), is easier (and

cheaper) to implement in practice than full *many-body* approaches, and has been quite successful in improving some features over the LDA.

The exchange-correlation energy has a gradient expansion

$$E_{XC}[\rho] = \int A_{XC}[\rho] \rho(\mathbf{r})^{4/3} d\mathbf{r} + \int C_{XC}[\rho] |\nabla \rho(\mathbf{r})|^2 / \rho(\mathbf{r})^{4/3} d\mathbf{r} + \dots \quad (2.48)$$

which is asymptotically valid for densities that vary slowly in space. The LDA retains only the leading term of Eq. (2.48). It is well-known that a straightforward evaluation of this expansion is ill-behaved, in the sense that it is not monotonically convergent, and it exhibits singularities that cancel out only when an infinite number of terms is resumed. In fact, the first-order correction worsens the results, and the second order correction is plagued of divergences [79]. The largest errors of this approximation actually arise from the gradient contribution to the correlation term. Provided that the problem of the correlation term can be cured in some way, the biggest problem remains with the exchange energy.

Many papers have been devoted to the improvement of the exchange term within DFT [71]. In general, those GGAs are either based on theoretical developments that reproduce the exact results in some known limits, or that are generated by fitting a number of parameters to a molecular database (training set). Normally, these improve some of the drawbacks of the LDA. The basic idea of GGAs is to express the exchange-correlation energy in the following form:

$$E_{XC}[\rho] = \int \rho(r) \varepsilon_{XC}[\rho(\mathbf{r})] d\mathbf{r} + \int F_{XC}[\rho(\mathbf{r}), \nabla \rho(\mathbf{r})] d\mathbf{r} \quad (2.49)$$

where the function F_{XC} is asked to satisfy a number of formal conditions for the exchange-correlation hole, like sum rules, long-range decay, etc. Naturally, not all the formal properties can be enforced at the same time, and this differentiates one functional from another. A comparison of different GGAs can be found in [71].

In the present work the Perdew-Burke-Ernzerhof (PBE) exchange-correlation functional [80] is used. This GGA retains the correct features of LDA (LSDA), and combines them with the nonlocality features which are supposed to be the most energetically important. It sacrifices a few correct, but less important features, like the correct second-order gradient coefficients in the slowly-varying limit, and the correct nonuniform scaling of the exchange energy in the rapidly varying density region.

2.4. Solving the electronic problem in practice

Solids are macroscopic objects constituted by a huge number of atoms, of the order of the Avogadro number (6×10^{23}). This justifies the standard approach of describing solids as an infinite collection of atoms. Crystalline solids are those in which a small number of atoms (*a basis*) is infinitely replicated along d different directions in space, where d is the dimensionality of space. Bulk solids are replicated in three dimensions, surfaces in two, and wires in one. These directions are defined by d linearly independent vectors.

There are infinitely many ways of characterizing a crystalline solid, depending on the choice of the set of atoms that are replicated. However, there is only one choice with the minimal number of atoms that contains the whole symmetry of the system. This is called the *primitive cell*, like for instance the Wigner-Seitz cell, which contains all the information about the point group symmetry underlying the crystalline structure. The vectors that serve to reconstruct the infinite solid from this cell are also unique, and are called *primitive vectors*. The set of points in space corresponding to integer combinations of the primitive vectors receives the name of *Bravais lattice*, of which there are only 14 in three dimensions with 36 associated point group symmetries. The combination of the translational symmetry present in the Bravais lattice plus the point group symmetry of the basis, gives rise to 230 space groups, which are sufficient to classify all the known crystalline solids. We will call $\{\mathbf{a}_i\}$, $i = 1, 2, 3$, the primitive vectors, and the volume of the cell is going to be $\Omega = \mathbf{a}_1 \cdot (\mathbf{a}_2 \times \mathbf{a}_3)$. The Wigner-Seitz cell can be constructed by drawing a line perpendicular to each unit vector exactly at its mid point.

The properties of the infinite system are connected to those of the unit cell by means of Bloch's theorem:

Theorem(Bloch): the wave function of an electron in an external periodic potential $V(\mathbf{r}) = V(\mathbf{r} + \mathbf{a}_i)$ can be written as the product of a function with the same periodicity of the potential, and a purely imaginary phase factor arising from the translational symmetry, *i.e.*

$$\Psi_{\mathbf{k}}(\mathbf{r}) = e^{i\mathbf{k}\cdot\mathbf{r}} u_{\mathbf{k}}(\mathbf{r}) \quad (2.50)$$

with $u_{\mathbf{k}}(\mathbf{r}) = u_{\mathbf{k}}(\mathbf{r} + \mathbf{a}_i)$. This implies that:

$$\Psi_{\mathbf{k}}(\mathbf{r} + \mathbf{a}_i) = e^{i\mathbf{k}\cdot\mathbf{a}_i} \Psi_{\mathbf{k}}(\mathbf{r}) \quad (2.51)$$

The reciprocal lattice vectors are defined by the relation $\mathbf{a}_i \cdot \mathbf{b}_j = 2\pi\delta_{ij}$, such that $e^{i\mathbf{a}_i \cdot \mathbf{b}_j} = 1$. This implies:

$$\mathbf{b}_1 = 2\pi \frac{\mathbf{a}_2 \times \mathbf{a}_3}{\Omega}; \quad \mathbf{b}_2 = 2\pi \frac{\mathbf{a}_3 \times \mathbf{a}_1}{\Omega}; \quad \mathbf{b}_3 = 2\pi \frac{\mathbf{a}_1 \times \mathbf{a}_2}{\Omega} \quad (2.52)$$

and the volume of the reciprocal cell is: $\mathbf{b}_1 \cdot (\mathbf{b}_2 \times \mathbf{b}_3) = (2\pi)^3/\Omega$. The cell defined by the reciprocal vectors corresponding to the primitive vectors is called the first Brillouin zone, or Brillouin zone for short (BZ). The idea is that any vector outside the BZ can be written as $\mathbf{k} = \mathbf{k}' + \mathbf{G}$ with \mathbf{k}' inside the BZ and $\mathbf{G} = n_1\mathbf{b}_1 + n_2\mathbf{b}_2 + n_3\mathbf{b}_3$, with n_i integer numbers. In other words, the whole reciprocal space can be covered by translating the BZ with vectors of the reciprocal lattice. It is clear that $e^{i\mathbf{G} \cdot \mathbf{a}_i} = 1 \Rightarrow e^{i\mathbf{k} \cdot \mathbf{a}_i} = e^{i\mathbf{k}' \cdot \mathbf{a}_i}$. Such a periodic wave function obeys the Schrödinger equation

$$\left\{ -\frac{\hbar^2}{2m_e} \nabla^2 + V(\mathbf{r}) \right\} \Psi_{\mathbf{k}}(\mathbf{r}) = \varepsilon_{\mathbf{k}} \Psi_{\mathbf{k}}(\mathbf{r}) \quad (2.53)$$

where $\varepsilon_{\mathbf{k}}$ is the energy of the wave. It is easy to see that there is a family of solutions $\Psi_{\mathbf{k}+\mathbf{G}}(\mathbf{r})$ and $\Psi_{\mathbf{k}'+\mathbf{G}'}(\mathbf{r})$ with the same energy, provided that $|\mathbf{k} + \mathbf{G}| = |\mathbf{k}' + \mathbf{G}'|$, for instance $\mathbf{k}' = \mathbf{k} + (\mathbf{G} - \mathbf{G}')$. It is then clear that for every vector \mathbf{k}' we can always find another vector \mathbf{k} in the first BZ such that $\varepsilon_{\mathbf{k}} = \varepsilon_{\mathbf{k}'}$. Since wave functions of identical energy mix together, then the solutions of the eigenvalue problem have to be searched in the degenerate subspaces $\{\Psi_{\mathbf{k}+\mathbf{G}}(\mathbf{r})\}$, where \mathbf{G} represent all the reciprocal lattice vectors. Therefore, we can focus on the solution of the eigenvalue problem for \mathbf{k} vectors in the first BZ, and then obtain trivially the solution for any vector outside the first BZ that is connected with \mathbf{k} through a lattice vector \mathbf{G} . A more detailed treatment of solid state theory can be found in any specific book on the subject [81].

In conclusion, the calculation of the wave function for each of the infinite number of electrons in the infinite solid, is mapped, via Bloch theorem, onto the calculation of the wave function for a finite number of electrons in the unit cell, at an infinite number of \mathbf{k} vectors in the first BZ. Obviously, we do not want to solve the electronic problem for an infinite number of Bloch states. Nearby \mathbf{k} vectors carry very similar information. Therefore, it should be possible to reproduce the required physical properties to the desired numerical accuracy by using the wave functions at a finite number of \mathbf{k} -points in the first BZ.

The central problem in electronic structure at the single-particle approximation level is, then, to self-consistently solve a set of N coupled, 3-dimensional, partial differential

equations. In the Kohn-Sham formulation of DFT for infinite systems, this set of equations reads [71]:

$$\hat{H}_{KS}\Psi_{\mathbf{k},i}(\mathbf{r}) = \left\{ -\frac{\hbar^2}{2m_e}\nabla^2 + v_{ext}(\mathbf{r}) + \int \frac{\rho(\mathbf{r}')}{|\mathbf{r}-\mathbf{r}'|}d\mathbf{r}' + \mu_{XC}[\rho] \right\} \Psi_{\mathbf{k},i}(\mathbf{r}) = \varepsilon_{\mathbf{k},i}\Psi_{\mathbf{k},i}(\mathbf{r}) \quad (2.54)$$

The coupling arises through the electronic density, which is now expressed as a BZ average,

$$\rho(\mathbf{r}) = \sum_{\mathbf{k} \in BZ} \omega_{\mathbf{k}} \sum_{i=1}^{N_{\mathbf{k}}} |\Psi_{\mathbf{k},i}(\mathbf{r})|^2 \quad (2.55)$$

where the sum runs over all \mathbf{k} vectors in the BZ of the unit cell, $N_{\mathbf{k}}$ is the number of electronic states that are occupied at that particular \mathbf{k} -point and $\omega_{\mathbf{k}}$ are weight factors that depend on the symmetry of the unit cell. If the system is insulating, then $N_{\mathbf{k}}$ is independent of \mathbf{k} and equal to the number of electrons N (if there is spin degeneracy the number of independent eigenfunctions is $N/2$, so that the sum is performed up to $N/2$, and the result multiplied by 2. For metallic systems the occupation numbers $N_{\mathbf{k}}$ are determined by asking that the associated eigenvalues $\{\varepsilon_{\mathbf{k},i}\}$, $i = 1 \dots N_{\mathbf{k}}$, be smaller than a certain value ε_F (the Fermi level). This latter is self-consistently adjusted to fulfill the normalization condition: $\sum_{\mathbf{k} \in BZ} N_{\mathbf{k}}\omega_{\mathbf{k}} = N$.

The external potential $v_{ext}(\mathbf{r})$ represents the interaction between the electrons and the nuclei, and is expressed in the following way:

$$v_{ext}(\mathbf{r}) = -e^2 \sum_{I=1}^P \frac{Z_I}{|\mathbf{r}-\mathbf{R}_I|} \quad (2.56)$$

The representation of the wave functions implies the choice of a basis set. Many possibilities have been explored since the early times of solid state theory and quantum chemistry, which can be divided into four main groups:

1. Extended basis sets: basis functions are delocalized, floating or centered at the nuclear positions.
2. Localized basis sets: basis functions are localized, mainly centered at the nuclear positions, but not uniquely.
3. Mixed basis sets: a combination of extended and localized basis functions.

4. Augmented basis sets: an extended or localized basis set is augmented with atomic-like wave functions in some region around the nuclei.

When dealing with extended systems (solids or liquids), it has to be ensured that Bloch's theorem is verified, in the sense that the combination of basis orbitals representing a solution to the Schrödinger equation must have the periodicity of the supercell. Expanding the wave functions on some generic basis set $|\phi_{\mathbf{k}_n}\rangle$:

$$\Psi_{\mathbf{k},j}(\mathbf{r}) = \sum_{n=1}^M C_{\mathbf{k}_n,j} \phi_{\mathbf{k}_n}(\mathbf{r}), \quad (2.57)$$

the Schrödinger equation becomes a matrix equation (*secular equation*):

$$\sum_{m=1}^M (H_{nm}^{\mathbf{k}} - \varepsilon_{\mathbf{k},j} S_{nm}^{\mathbf{k}}) C_{\mathbf{k}_m,j} = 0 \quad (2.58)$$

where $H_{nm}^{\mathbf{k}} = \langle \phi_{\mathbf{k}_n} | \hat{H} | \phi_{\mathbf{k}_m} \rangle$ and $S_{nm}^{\mathbf{k}} = \langle \phi_{\mathbf{k}_n} | \phi_{\mathbf{k}_m} \rangle$. In the above expressions, M is the size of the basis set and j is a band index which labels the eigenvalues at fixed \mathbf{k} according to their energy. The number of occupied bands is $N/2$ (in the following we focus on the spin unpolarized case) with N the number of electrons in the unit cell. The overlap matrix $S_{nm}^{\mathbf{k}}$ appears in the secular equation because the basis functions do not need to be mutually orthogonal. In fact, in many electronic structure methods the basis set is non-orthogonal.

The electron-nuclear interaction is given by the bare Coulomb interaction. A first class of methods deals with all the electrons in the system, both those participating in the chemical bonding (*valence electrons*) and those tightly bound to the nuclei, which are almost unchanged with respect to the atomic case (*core electrons*). These are generically named *all-electron methods*. They can be constructed in a straightforward way by using finely tuned localized basis sets, like in quantum chemistry methods, or by separating the space in atomic spheres (as closely packed as possible) plus an interstitial region. In this latter, the wave functions of the valence electrons are expanded in some basis set in the interstitial region, and are augmented with atomic-like solutions inside the spheres while the wave functions for the core electrons are obtained as solutions of the atomic problem but taking into account the perturbation produced by the presence of the other atoms. Such a sphere is often called a *Muffin Tin sphere* (MT) and are schematically shown in Fig. 2.1, the part of space occupied by the spheres is the MT region (I); the remaining space outside the spheres is called the interstitial region (II).

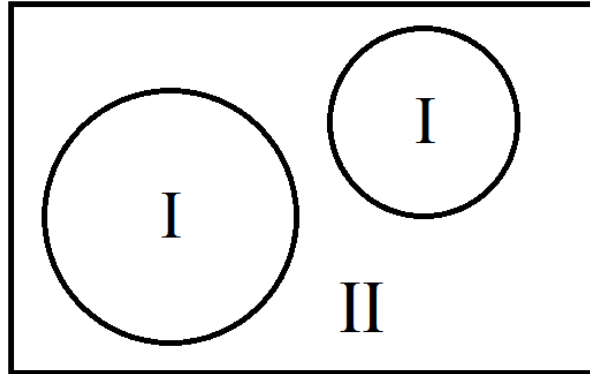


Figure 2.1.: Partitioning of the unit cell into atomic spheres (I) and interstitial region (II)[82].

Since core electrons usually do not participate in chemical bonding, it is possible to integrate out the corresponding degrees of freedom by considering a screened interaction between the valence electrons and the ionic cores, i.e. nuclei plus core electrons. A good description of the valence wave functions inside the ionic cores is, in most cases, unnecessary, because one is usually concerned with bonding properties. In that case, there is no lack of crucial information if the inner solution (inside the core radius) is replaced with a smooth, nodeless pseudo-wave function, which behaves much better from the numerical point of view. This pseudo-wave function is not the solution of the original atomic problem, but the solution of a pseudo-atomic problem where the true potential has been replaced by a pseudopotential. This type of approximations receive the name of *pseudopotential* methods.

The *pseudopotential* methods is extremely useful to study physical properties of solids, because most of them depend mainly on valence electrons. But, if you are interested in information that is related with the region near the nucleus, like core level excitations, hyperfine fields, etc. you need to deal with the *all-electron methods*. The main interest of the present thesis is related with the hyperfine fields, then the *all-electron method* programed in the WIEN2k code [82] is used. These methods and the one implemented in WIEN2k will be discussed in detail below.

2.5. All-electron methods

There are three main all-electron methodologies according to the basis set used in the interstitial region [71]:

- **Localized basis sets:** This methodology is the most widely used in the quantum chemistry community and is better describing molecular systems than solids.
- **Muffin Tin Orbitals (MTO):** The wave functions in the interstitial region are expanded in spherical Hankel functions centered at the nuclear positions. Hankels are solutions of the spherically symmetric Schrödinger equation in the absence of a potential (as it is the case in the interstitial region) which are regular at the origin, rapidly varying inside the Muffin Tin (MT), and exponentially decaying outside.

The method using nonlinear matching conditions [83] is due to Korringa, Kohn and Rostocker (**KKR**) [84, 85]. The linear method, or **LMTO**, was originally proposed by O. K. Andersen [86] and is one of the most popular all-electron methods because it is very fast. The fastness arises from the fact that the basis functions can be finely tuned so that a small number of them is enough to have a reasonable description of the system. The treatment of the potential in the interstitial region is an expensive part of the calculation with MTO's. Methods that include self-consistently this contribution receive the name of *full-potential* (e.g. **FP-LMTO** [87]). A much faster method, although not very accurate, consists of approximating the potential in the interstitial region with a constant value, and increasing the size of the MT spheres until they touch each other (optimal close packing). This method is known as the atomic sphere approximation (**LMTO-ASA**), and has been very widely used in the past. Nowadays, FP methods have superseded it. MTO have a drawback when they are used to study open structures. The interstitial vacuum is poorly described unless empty spheres (MT spheres with zero charge) to fill the empty space are included in the basis set. However, this renders more difficult the comparison of different structures at the level of the energetics, and forces on the nuclei cannot be computed. Modern developments along the LMTO line have very recently overcome these difficulties.

- **Augmented Plane Waves (APW):** the wave functions in the interstitial region are expanded in plane waves, which are the solutions of the Schrödinger equation for free electrons in a box, and matched to atomic-like solutions inside the spheres. Only the lowest angular momenta ($l = 0, 1, 2, \dots, l_{max}$) are present inside the spheres,

so that only these projections of the plane waves (PW) are matched [88]. The components of the PW with angular momentum $l > l_{max}$ are allowed to penetrate inside the spheres without forcing any matching condition. This is the full-potential version of the APW (**FP-APW**) method.

The version which linearizes the logarithmic derivatives is called Linearized augmented plane waves (**LAPW**), is presently one of the most accurate electronic structure method available and is the basis of the WIEN2k code [82]. The expansion of the wave functions in the interstitials in PW gives a great flexibility because there is no need of empty spheres as in LMTO methods.

2.6. The full potential augmented plane wave (APW) methods

As mentioned before, the APW method uses a modified plane wave basis in the expansion of $\Psi_{\mathbf{k}_n, j}(\mathbf{r})$ (Eq. (2.57)). In the interstitial region a plane wave expansion is used and inside the atomic sphere, the wave functions are expanded by radial functions times spherical harmonics [82, 89]:

$$\phi_{\mathbf{k}_n}(\mathbf{r}, E_l) = \begin{cases} \frac{1}{\sqrt{\Omega}} e^{i\mathbf{k}_n \cdot \mathbf{r}} & \mathbf{r} \in \mathbf{I} \\ \sum_{lm} [A_{lm, \mathbf{k}_n} u_l(r, E_l)] Y_{lm}(\hat{\mathbf{r}}) & \mathbf{r} \in \mathbf{II} \end{cases} \quad (2.59)$$

where $\mathbf{k}_n = \mathbf{k} + \mathbf{G}_n$; \mathbf{G}_n are the reciprocal lattice vectors, \mathbf{k} is the wave vector inside the first Brillouin zone, Ω is the unit cell volume and $u_l(r, E_l)$ is the (at the origin) regular solution of the radial Schroedinger equation for energy E_l (chosen normally at the center of the corresponding band with l -like character) and the spherical part of the potential inside the sphere. The coefficients A_{lm, \mathbf{k}_n} in the expansion are determined by a matching conditions between the wave functions at the MT and the interstitial region at the MT boundary.

In this approximation, the electron potential $V(r)$ is expanded in the following form:

$$V(r) = \begin{cases} \sum_{\mathbf{G}} V_{\mathbf{G}} e^{i\mathbf{G} \cdot \mathbf{r}} & \mathbf{r} \in \mathbf{I} \\ \sum_{lm} V_{lm}(r) Y_{lm}(\hat{\mathbf{r}}) & \mathbf{r} \in \mathbf{II} \end{cases} \quad (2.60)$$

The APW-method itself is of no practical use any more due to its computationally inefficiency. It can not get the eigenvalues from a single diagonalization because the unknown parameter E_l in Eq. (2.59) and the exact value is needed to describe the eigenstate $\Psi_{\mathbf{k}_n}(\mathbf{r})$. The resulting eigenvalue problem is non-linear in energy, since E_l depends on the function $u_l(r, E_l)$. Nevertheless, based on this method other approximations appear.

2.6.1. The linearized augmented plane wave (LAPW) method

To overcome this APW method non-linearity problem the LAPW method propose to expand the radial function in Taylor series around E_l [82, 89]:

$$u_l(r, E_l) = u_l(r, E_l^0) + (E_l - E_l^0)\dot{u}_l(r, E_l^0) + O((E_l - E_l^0)^2) \quad (2.61)$$

where

$$\dot{u}_l(r, E_l^0) = \left. \frac{\partial u_l(r, E_l)}{\partial E_l} \right|_{E_l=E_l^0} \quad (2.62)$$

In this case, if E_l^0 is set near E_l the radial function and energy errors are negligible. Then the LAPW basis set can be defined as [82, 89]:

$$\phi_{\mathbf{k}_n}(\mathbf{r}, E_l) = \begin{cases} \frac{1}{\sqrt{\Omega}} e^{i\mathbf{k}_n \cdot \mathbf{r}} & \mathbf{r} \in \mathbf{I} \\ \sum_{lm} [A_{lm, \mathbf{k}_n} u_l(r, E_l) + B_{lm, \mathbf{k}_n} \dot{u}_l(r, E_l)] Y_{lm}(\hat{\mathbf{r}}) & \mathbf{r} \in \mathbf{II} \end{cases} \quad (2.63)$$

The linear combination of u_l and \dot{u}_l functions constitute the linearization of the radial function; and they are obtained by numerical integration of the radial Schroedinger equation on a radial mesh inside the sphere. The coefficients A_{lm, \mathbf{k}_n} and B_{lm, \mathbf{k}_n} are determined by requiring that this basis function matches (in value and slope) each plane wave (PW) the corresponding basis function of the interstitial region. Each plane wave is augmented by an atomic-like function in every atomic sphere.

The solutions to the Kohn-Sham equations are expanded in this combined basis set of LAPW's according to the linear variation method (Eq. (2.57)) and the coefficients $C_{\mathbf{k}_n, j}$ are determined by the Rayleigh-Ritz variational principle. The convergence of this basis set is controlled by a cutoff parameter $R_{mt} K_{max} = 6 - 9$, where R_{mt} is the smallest

atomic sphere radius in the unit cell and K_{max} is the magnitude of the largest \mathbf{k} vector in equation (2.57).

The linearized augmented plane wave with local orbitals (LAPW+LO) method

In order to improve the linearization, to make possible a consistent treatment of semicore and valence states, additional basis functions can be added. This can be done by introducing “local orbitals” (LO) [82, 89, 90]:

$$\phi_{lm}^{LO} = [A_{lm}u_l(r, E_{1,l}) + B_{lm}\dot{u}_l(r, E_{1,l}) + C_{lm}u_l(r, E_{2,l})]Y_{lm}(\hat{\mathbf{r}}) \quad (2.64)$$

The coefficients A_{lm} , B_{lm} and C_{lm} are determined considering that ϕ^{LO} should be normalized and has zero value and slope at the sphere boundary.

2.6.2. The augmented plane wave with local orbitals (APW+lo) method

Another efficient way to linearize the APW method is achieved by introducing “local orbitals” (lo) to the basis [91], but with $u_l(r, E_l)$ at a fixed energy E_l [82, 89]:

$$\phi_{lm}^{lo} = [A_{lm}u_l(r, E_{1,l}) + B_{lm}\dot{u}_l(r, E_{1,l})]Y_{lm}(\hat{\mathbf{r}}) \quad (2.65)$$

This lo (which are distinct from the LO given in Eq. (2.64)) looks almost like the LAPW-basis set, but A_{lm} and B_{lm} do not depend on \mathbf{k}_n and are determined considering that the lo is zero at the sphere boundary and normalized.

2.7. Hyperfine interaction parameters calculation through density functional theory

2.7.1. Hyperfine electric parameters calculation

Section 1.2 describes that in order to obtain the isomer shift δ of a given atom in a sample one has to compare its electron density at the nucleus ρ_0 with a reference. The

ρ_0 value is calculated by the WIEN2k code as a contact density evaluated at the first radial mesh point [82]. In this approach, the isomer shifts can be calculated using the following expression [92, 93]:

$$\delta = \alpha(\rho_0^{sample} - \rho_0^{reference}) \quad (2.66)$$

where α , is the nuclear calibration constant. Several reports of this calibration constant exist in the literature for ^{57}Fe and other nucleus [92–96]. In the present study, the value $\alpha = -0.291 \text{ a.u.}^3 \text{ mm/s}$ reported by Wdowik and Ruebenbauer [92] for the ^{57}Fe Mössbauer transition is used. The bcc Fe (with lattice constant $a = 2.865 \text{ \AA}$) was taken as reference, as in the experimental reports for Si [20], ZnO [27, 28] and $\text{YBa}_2\text{Cu}_{3-x}\text{Fe}_x\text{O}_{7-y}$ [39–42] samples implanted or doped with ^{57}Fe .

In order to evaluate Eq. 2.66 in a consistent way the same R_{mt} value and number of radial mesh points are used for Fe, in the studied case and in the bcc Fe reference calculation. The DFT calculation for the bcc Fe is performed with 286 k -points in the irreducible part of the Brillouin zone; and the number of radial mesh points is fixed to 781 in all cases.

The EFG is defined as the second derivative of the electrostatic potential (Eq. (1.15)), evaluated at the nuclear site of the probe atom ($\mathbf{r} = \vec{0}$) embedded in the material. The EFG is a traceless symmetric tensor of rank 2, due to the Poisson equation:

$$\sum_{\alpha} V_{\alpha\alpha} = \rho(0) = 0 \quad (2.67)$$

Due to the permutation of partial derivatives the tensor has to be symmetric, then in order to determine the tensor unambiguously five independent quantities have to be provided. In WIEN2k the potential is calculated using a spherical notation and the five spherical components of the EFG tensor are calculated ($L=2$, $M=-2, -1, 0, 1, 2$). The code finally evaluates the Cartesian components of the EFG tensor using the following expressions [97]:

$$(V_{\alpha\beta}) = \sqrt{\frac{15}{16\pi}} \lim_{r \rightarrow 0} \frac{1}{r^2} \cdot \begin{pmatrix} V_{22}(r) - \frac{1}{\sqrt{3}}V_{20}(r) & V_{2,-2}(r) & V_{21}(r) \\ V_{2,-2}(r) & -V_{22}(r) - \frac{1}{\sqrt{3}}V_{20}(r) & V_{2,-1}(r) \\ V_{21}(r) & V_{2,-1}(r) & \frac{2}{\sqrt{3}}V_{20}(r) \end{pmatrix} \quad (2.68)$$

The principal component V_{zz} can be obtained from the charge density $\rho(\mathbf{r})$ as:

$$V_{zz} = \int \rho(\mathbf{r}) \frac{2P_2(\cos \theta)}{r^3} d\mathbf{r} \quad (2.69)$$

where P_2 is the second order Legendre polynomial.

The WIEN2k code give as an output V_{zz} and η . Then the quadrupole splitting (Δ) can be obtained using the following expression for the $\frac{1}{2} \rightarrow \frac{3}{2}$ transition of ^{57}Fe [66]:

$$\Delta = \frac{1}{2} eQV_{zz} \left(1 + \frac{1}{3} \eta^2 \right)^{\frac{1}{2}} \quad (2.70)$$

where e is the electron charge and Q is the ^{57}Fe nuclear quadrupole moment, which was determined by Dufek *et al.* [98] to be $Q=0.16$ b (1 b= 10^{-28} m²). The Δ values obtained from Eq. (2.70) are expressed in eV, then to compare the results with the experimental reports was considered that, for ^{57}Fe MS, 48.14 neV is equivalent to 1 *mm/s*.

In the PAC experiments the spectra is decomposed in the frequency domain, obtaining the characteristic quadrupole frequencies ν_Q values, that are proportional to V_{zz} (see section 1.4.2) [70]:

$$\nu_Q = \frac{eQV_{zz}}{h} \quad (2.71)$$

where e is the electron charge, h is the Planck constant and Q is the nuclear electric quadrupole moment; reported as $Q = 0.83(13)$ b for the $I^\pi = 5/2^+$ intermediate level of ^{111}Cd [99].

The contributions to V_{zz} from a given type of electronic states of harmonic character l ($l = 0; 1; 2$ for s , p and d electrons) can also be taken into account, which can be estimated using the following equation [54, 58]:

$$V_{zz}^l = (4\pi/5)^{1/2} \int_0^{R_{mt}} \frac{\rho_{20}^l}{r^3} r^2 dr \quad (2.72)$$

where ρ_{20}^l is the non-spherical charge densities of the corresponding l electronic state.

The EFG expresses the deviation from the spherical symmetry of the electron density around the probe atom. This asymmetry or anisotropy for p and d electrons can be

calculated by the following expressions [51, 52, 100]:

$$\Delta n_p(E) = \frac{1}{2}n_{p_{xy}}(E) - n_{p_z}(E) \quad (2.73)$$

$$\Delta n_d(E) = n_{d_{xy}}(E) + n_{d_{x^2-y^2}}(E) - \frac{1}{2}(n_{d_{xz}}(E) + n_{d_{yz}}(E)) - n_{d_{z^2}}(E) \quad (2.74)$$

where n_{p_i} ($i = x, y, z$) and n_{d_i} ($i = xy, x^2 - y^2, xz, yz, z^2$) are the number of electrons in the p_i and d_i orbitals respectively. These quantities can be obtained from the local DOS of p_i and d_i electrons as [51, 52, 100]:

$$n_{p_i}(E_1) = \int_{-\infty}^{E_1} p_i(E) dE \quad (2.75)$$

$$n_{d_i}(E_1) = \int_{-\infty}^{E_1} d_i(E) dE \quad (2.76)$$

These integrals count the number of p_i and d_i electrons with energy less than E_1 . Furthermore, it has been reported that these p and d electron anisotropies evaluated at the Fermi energy (ε_F) is proportional to the corresponding V_{zz}^l expressed by Eq. (2.72) [51, 52, 100]:

$$V_{zz}^{pp} \propto \Delta n_p(\varepsilon_F) \quad (2.77)$$

$$V_{zz}^{dd} \propto \Delta n_d(\varepsilon_F) \quad (2.78)$$

These proportionality relations can help to understand the origin of the EFG temperature dependence in some materials, or with other factors that alter the Fermi energy position or the DOS distribution.

2.7.2. Hyperfine magnetic parameters calculation

The internal hyperfine field on a nuclei of an atom can be written from Eq. (1.22) as:

$$\mathbf{B}_{Int} = \mathbf{B}_c + \mathbf{B}_{orb} + \mathbf{B}_{dip} \quad (2.79)$$

These terms are evaluated in standard spin-polarized WIEN2k calculation [82], using the following expressions [101]:

$$\mathbf{B}_{orb} = 2\mu_B \left\langle \Phi_l \left| \frac{S(r)}{r^3} \mathbf{l} \right| \Phi_l \right\rangle \quad (2.80)$$

$$\mathbf{B}_{dip} = 2\mu_B \left\langle \Phi_l \left| \frac{S(r)}{r^3} [3(\mathbf{s}\hat{\mathbf{r}})\hat{\mathbf{r}} - \mathbf{s}] \right| \Phi_l \right\rangle \quad (2.81)$$

$$\mathbf{B}_c = \frac{8\pi}{3} \mu_B \mathbf{m}_{av} \quad (2.82)$$

where, $\mu_B = e\hbar/2mc$, m is the electron mass, Φ_l is the large component of the relativistic wave function, \mathbf{l} the orbital moment of an electron localized on the atom in question (expressed in units of \hbar), \mathbf{s} is the electron spin, $S(r)$ is reciprocal of the relativistic mass enhancement [101], and \mathbf{m}_{av} is defined as:

$$\mathbf{m}_{av} = \int d\mathbf{r}' \delta_T(\mathbf{r}') \langle \Phi_l | \boldsymbol{\sigma} \delta(\mathbf{r} - \mathbf{r}') | \Phi_l \rangle \quad (2.83)$$

here $\boldsymbol{\sigma}$ are the Pauli matrices and,

$$\delta_T(r) = \frac{1}{4\pi r^2} \frac{r_T/2}{[(1 + \epsilon/2mc^2)r + r_T/2]^2} \quad (2.84)$$

where $r_T = Ze^2/mc^2$ is the Thomas radius (see Ref. [101] for more details).

2.8. Calculation Methodology

To study the electronic structure of the materials investigated in the thesis the WIEN2k code is used [82]. This code is based on the full potential linearized augmented plane wave (FP-LAPW) method described in section 2.6, within the DFT.

To apply this calculation method, the WIEN2k code needs as an input the crystal structure details of the material and a set of parameters related with the FP-LAPW method. The materials crystal structure is considered as known and reported values are used. In the case of implanted materials the reported structure parameters are used if they exist, otherwise the values reported for the non-implanted or doped material are used and optimized if necessary. The presence of crystalline defects is also considered in the cases where they are expected to occur, mainly Frenkel pair types of defects (vacancies and interstitials) [102, 103] are taken into account. The implantation and damage creation in

the sample is simulated using the Binary Collision Approximation (BCA) [103] within the Monte Carlo method. Several computer simulation codes designed to calculate the damage structure in cascades have been developed [104–107].

In the present study the ion implantation in the target materials and the radiation damage created in it is simulated using the SRIM(TRIM) code [107–109]. This code needs as input information on the target composition, density, thickness, threshold energy, etc.; as well as the incident ion data: energy, angle of incidence, etc. Then, as result the ion implantation and generated vacancies profiles, energy loss, phonon's, etc. are obtained. More information about the SRIM code can be found in [108, 109].

Starting from the known material crystal structure, and considering the ion implantation and generated vacancy profiles for the reported experimental condition, some probable implantation configurations are proposed and its electronic structure is evaluated. In general these implantation configurations are recreated in supercells (SCs) that are produced by the repetition of the crystallographic cell of the material. These SCs are created to reproduce the impurity concentration in the case of concentrated alloys or they are taken as big as possible to simulate dilute systems.

The electronic structure calculation with the WIEN2k code give information about the hyperfine parameters. In the calculation procedure the following set of parameters are optimized because the accuracy of the calculated hyperfine parameters depend on them. They are the plane-wave cutoff value $R_{mt}K_{max}$, the magnitude of the largest vector in the charge-density Fourier expansion G_{max} , the maximum l quantum number for the wave function expansion inside the atomic spheres and the number of k points used in the irreducible Brillouin zone (they are defined in sections 2.5 and 2.6). These calculations are computationally expensive, because big SCs are generally needed.

The comparison between the calculated hyperfine parameters and the experimental reports is established considering the Δ and δ values and its distribution, characterized by the spectral lines width. Then a proposed configuration is correlated with a certain experimental line if the calculated Δ and δ values stay within the experimental parameters distribution.

Part II.

NUMERICAL RESULTS AND VALIDATION OF EXPERIMENTS

Chapter 3.

Radiation damage and calculation of hyperfine parameters in ZnO implanted with ^{57}Mn (^{57}Fe) and ^{111}In (^{111}Cd)

The work presented in this chapter have been published in the following papers: Y. Abreu, C. M. Cruz, I. Piñera, A. Leyva, A. E. Cabal and P. Van Espen. *DFT study of the hyperfine parameters and magnetic properties of ZnO doped with ^{57}Fe* . Solid State Commun. 185, 2014, pp. 25-29. And, Y. Abreu, C.M. Cruz, P. Van Espen, C. Pérez, I. Piñera, A. Leyva and A. E. Cabal. *Electric field gradient calculations in ZnO samples implanted with ^{111}In (^{111}Cd)*. Solid State Commun. 152(5), 2012, pp. 399-402.

3.1. Introduction

Recently, the semiconductor ZnO has attracted considerable attention in the research community in part due to the availability of high-quality substrates, and new reports of p-type conduction and ferromagnetic behavior when doped with transitions metals. Dilute magnetic semiconductors are of current interest as potential semiconductor-compatible magnetic components for spintronic applications. In ZnO semiconductor, it is possible to achieve a partial replacement of cations by magnetic transition-metal ions [62]. However, the origin of magnetism in these cases is poorly understood and there are inconsistent reports in the literature [26–31, 62, 110].

Through Mössbauer spectroscopy several authors studied the hyperfine parameters and magnetization of ^{57}Fe in ZnO [26–31]. In [27–29], the Mössbauer spectra of dilute

^{57}Mn (^{57}Fe) impurities implanted in ZnO samples were measured at temperatures from 300 to 800 K, showing: 1) two doublets (D2 and D3) assigned, respectively, to substitutional and interstitial configuration sites and, 2) three sextets corresponding to magnetic ordered state configurations of the implanted ions. The authors suggested as well that the magnetic ordered state can be related to the presence of Zn vacancies in the probe atom neighborhood, considering that Zn vacancies are mobile above 300 K while for oxygen they are stable up to ≈ 600 K. It was also reported in [28] that at temperatures over 700 K the doublet D2 is dominant in the spectra. In Fig 3.1 the Mössbauer spectra measured at different temperatures in ZnO samples implanted with ^{57}Mn (^{57}Fe) are shown.

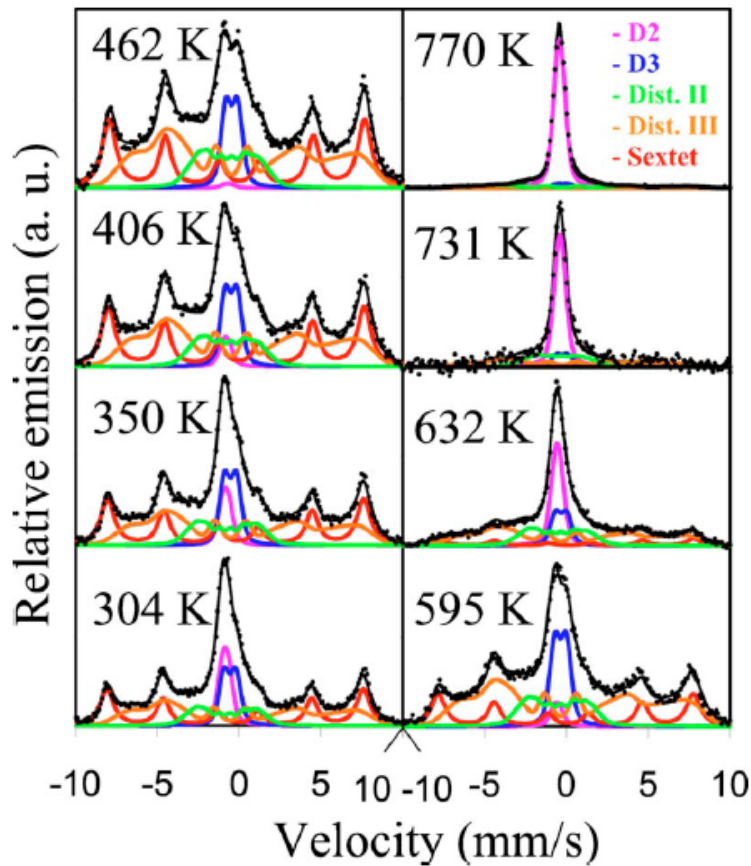


Figure 3.1.: Mössbauer spectra measured at different temperatures in ZnO samples implanted with ^{57}Mn (^{57}Fe), reported in [28].

Other authors also reported the Mössbauer hyperfine parameters in ZnO samples doped with ^{57}Fe showing two main quadrupole lines and a weak sextet at low temperature [30, 31]. Those samples were annealed at high temperatures (923 and 1473 K) and measured from 4.2 to 295 K by Mössbauer Spectroscopy and magnetic methods. Then,

the observation of a magnetic ordered sextet only at low temperature, in this case, also supports the previous mentioned idea that the presence of a magnetic ordered phase at higher temperatures [27–29] could be related to the occurrence of $^{57}\text{Mn}(^{57}\text{Fe})$ implantation induced defects.

Recently, in [26] the lattice locations and electronic configurations of high fluence ^{57}Fe and $^{57}\text{Co}(^{57}\text{Fe})$ implanted into ZnO was reported, showing a broad Mössbauer spectrum. The spectra acquired upon room temperature implantation show two doublets, which were experimentally related with perturbed Zn substitutional sites and damage complexes of interstitial character. Then, when the sample is annealed at 773 K the substitutional fraction remains, while the damage component decreases and a new doublet appears; whose hyperfine parameters are similar to those of D3 in [28]. In general, a dependence of the hyperfine parameters on the temperature is also observed in most of the cases [26, 28–31].

The semiconductor ZnO is also an interesting material for optoelectronic applications [25, 62, 111–114]. Indium is known as one of the most efficient donor impurity used to improve optoelectronic properties of ZnO [25, 62, 111]. Dogra *et al.* [25] studied the radiation damage annealing of ^{111}In probe atoms implanted in ZnO samples. They measured the EFG, at room temperature, through PAC at the ^{111}In site in as-implanted samples and after subsequent furnace annealing in ambient nitrogen at various temperatures between 200 °C and 1000 °C. The as-implanted samples showed a broad distribution of EFG at the probe atoms, characterized by two main quadrupole interaction frequencies: $\nu_{Q1} = 30.9(5)$ MHz and $\nu_{Q2} = 113(2)$ MHz [25]. The sample annealing at temperatures above of 400 °C reduced the EFG distribution width and produced a diminution of the ν_{Q2} component in favor of ν_{Q1} ; indicating a majority fraction of probe atoms occupying a unique lattice site with equal surroundings. This site was ascribed to substitutional incorporation of probe atoms at cations-sites of ZnO [25].

In the current experimental situation, the ^{57}Fe Mössbauer spectra measured in both, Fe implanted and doped ZnO materials, remain with some ambiguous identification and structural assignments regarding the impurity location sites and the influence of defects and temperature on their hyperfine parameters and magnetic properties. In addition, the calculation of the hyperfine parameters values emerging from $^{111}\text{In}(^{111}\text{Cd})$ radioactive probe implanted in the ZnO matrix could give a better understanding of the experimental observations in this case. In the present work some possible implantation configurations are suggested and evaluated using Monte Carlo simulation and electronic structure calculations with DFT techniques. The main aim is to calculate and report the hyperfine

parameters at the probe sites in both cases, and to study the magnetic properties of Fe in ZnO, considering the presence of implantation induced defects. Previous DFT studies have been done in ZnO [112–118], but no report was found for hyperfine parameters calculations of ^{57}Mn (^{57}Fe) and ^{111}In (^{111}Cd) doped or implanted ZnO samples. Regarding the magnetic properties of Fe into ZnO some reports exist using DFT [119, 120], however, in the current study other possible implantation configurations, including the presence of defects, are studied. For ^{111}In (^{111}Cd) in ZnO, two EFG calculation are available but not through DFT calculations, one was reported by Dogra *et al.* [25] using the classic point charge model (PCM) and other by Mitchell *et al.* [121] within the Hartree-Fock (HF) cluster procedure.

3.2. Calculation Details

The implantation of ^{57}Mn and ^{111}In ions in a ZnO target with beam energies of 60 keV and up to 8 MeV respectively, was simulated using the SRIM Monte Carlo code [109]. The ions range and vacancies generated in the sample for each case are presented in Figs. 3.2 and 3.3 respectively. In the experiment the $^{57}\text{Mn}^+$ ion implantation fluence was $10^{12} \text{ ion}/\text{cm}^2$ [28] resulting in a maximal vacancy concentration of $\approx 1.86 \times 10^{20} \text{ Vac.}/\text{cm}^3$. This means, an average distance d_{V-V} between vacancies of 17.5 Å, and a low radiation damage of 4.5×10^{-4} displacements per atom (DPA), regarding the atomic density of ZnO ($4.14 \times 10^{23} \text{ atom}/\text{cm}^3$). Applying the In transport simulation with SRIM on a ZnO matrix and considering the experimental ^{111}In ion implantation fluence of $10^{11} \text{ ion}/\text{cm}^2$ [25], one expects a maximal vacancy concentration of $\approx 1.85 \times 10^{19} \text{ Vac.}/\text{cm}^3$, due to atom displacements, which represent a low radiation damage of 4.5×10^{-5} DPA. This means that, in this case the average distance between two vacancies should be $d_{V-V} \approx 37.8$ Å. Under the thermal annealing treatment, the radiation damage will be even lower and, consequently, d_{V-V} will be significantly higher in both cases. Then, the probability of the presence of vacancies in a crystal unit cell due to the direct ^{57}Mn and ^{111}In irradiation process is very low under the circumstances seen before. However, it is also important to take into account that the recoiled ^{57}Fe atoms with an average energy of 40 eV, as a result of the ^{57}Mn β decay, can produce also vacancies in the probe atoms neighborhood. On the contrary, the ^{111}Cd recoil energy is less than 1 eV during the radioactive ^{111}In (^{111}Cd) decay compared to typical lattice binding energies (10-20 eV) and the ^{111}Cd should remain in the same lattice location of its precursor. Then, it will be considered as possible that one vacancy can be present in the ^{57}Mn (^{57}Fe) and ^{111}In (^{111}Cd) vicinity. For the

moment the vacancies analysis will be focused on the Zn atomic positions because they are considered as mobile at room temperature and this increases the probability of been trapped in the probe atom neighborhood.

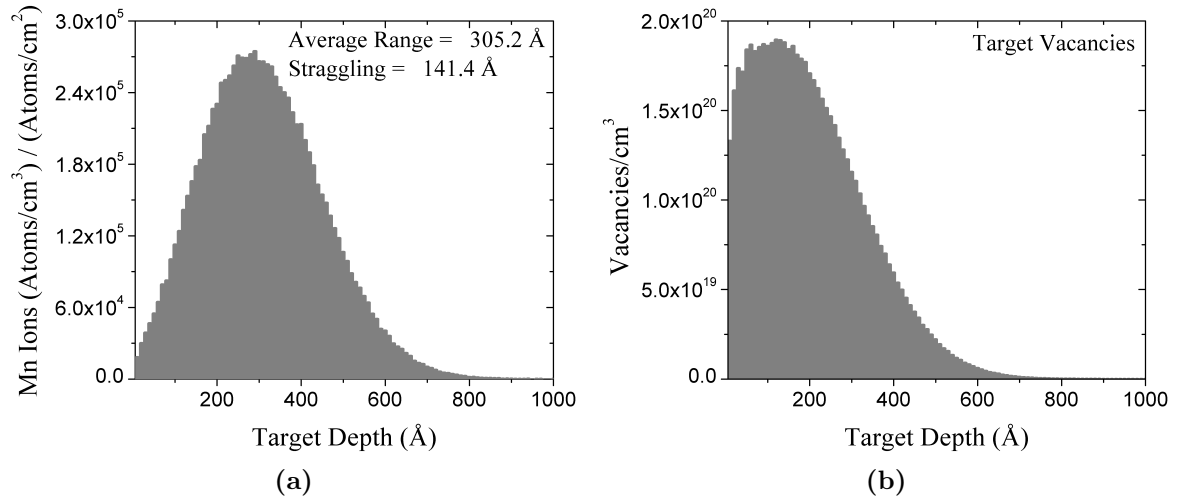


Figure 3.2.: Range of 60 keV Mn ions in a ZnO target (a) and vacancies generated in the ZnO target by the implantation process (b), simulated by SRIM-2010.

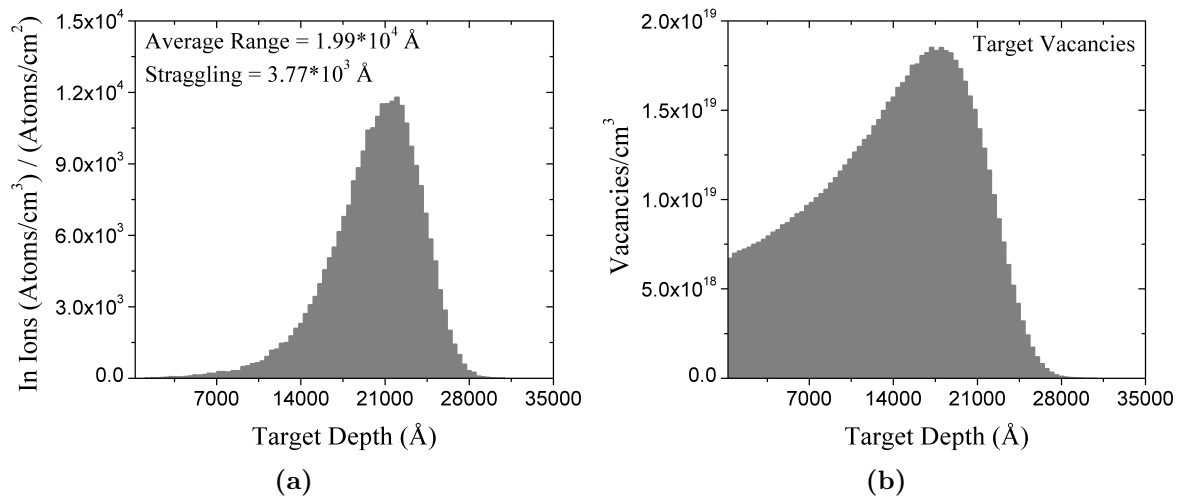


Figure 3.3.: Range of 8 MeV In ions in a ZnO target (a) and vacancies generated in the ZnO target by the implantation process (b), simulated by SRIM-2010.

ZnO normally crystallizes in a wurtzite crystal structure with hexagonal symmetry and P63mc space group. The experimental lattice parameters for this material reported in [122], $a = 3.249 \text{ \AA}$ and $c = 5.205 \text{ \AA}$, are used in the present research to describe the ^{111}In (^{111}Cd) implantation configuration, as justified in [123]. These configurations are recreated in two supercells (SCs) of 2x2x2 and 3x3x2 unit cells.

It was experimentally found that the crystalline structure of $\text{Zn}_{0.95}\text{Fe}_{0.05}\text{O}$ has also wurtzite hexagonal symmetry as the non-doped case, with lattice constants $a = 3.255 \text{ \AA}$ and $c = 5.207 \text{ \AA}$ at room temperature [31]. Then, in order to reproduce some of the possible ^{57}Mn (^{57}Fe) implantation environments in the ZnO material three SCs configurations starting from this crystal structure are considered, involving: 2x2x1, 2x2x2 and 3x3x2 unit cells. The 2x2x1 SC is included in this case to evaluate the possibility of Fe pair formation reported in [124]. Within this approach, the ZnO lattice parameters, including the Fe atom presence in the substitutional configurations, are optimized by minimizing the total energy as function of volume and c/a ratio. Then, the optimized lattice parameters are fixed to these values for each SC. Finally, for all the studied Fe and Cd configurations recreated in the SCs the internal atomic positions are minimized to a force limit below 1 mRy/ \AA .

In the Mössbauer experiment the hyperfine parameters were measured at the ^{57}Fe probe site produced by the ^{57}Mn β decay and in the PAC experiment it was measured at the ^{111}Cd site. Then, in the electronic structure calculations a Fe or a Cd atom, in addition, is incorporated into the considered SC configuration. Taking into account the Fe and Cd atomic radius and the bond distances in the ZnO crystal structure three possible implantation sites are evaluated: substitutional in a cation site (Fe_{sub} , Cd_{sub}), tetragonal interstitial site (Fe_{tet} , Cd_{tet}) and octahedral interstitial site (Fe_{oct} , Cd_{oct}). These possible implantation sites are schematically presented in Fig. 3.4, each one is studied for the proposed SC's configurations. The presence of cation vacancy (V_{Zn}) located at different distances from the probe site is also considered, with the following classifications: $\text{Fe}_{sub}\text{-}V_{Zn}$, $\text{Fe}_{tet}\text{-}V_{Zn}$ and $\text{Fe}_{oct}\text{-}V_{Zn}$ for Fe, as well as $\text{Cd}_{sub}\text{-}V_{Zn}$, $\text{Cd}_{tet}\text{-}V_{Zn}$ and $\text{Cd}_{oct}\text{-}V_{Zn}$ for the Cd case.

The electronic structure calculations were performed using the WIEN2k code [82]; based on the full-potential (linearized)-augmented-plane-wave plus local orbitals method (L/APW+lo) [125] within the DFT. In the study, the atomic spherical radii were set to 1.9, 1.55, 1.8 and 2.1 a.u. for Zn, O, Fe and Cd respectively. Good convergence in the results were obtained with the following set of parameters: the plane-wave cutoff value $R_{mt}K_{max} = 7.0$, the magnitude of the largest vector in the charge-density Fourier

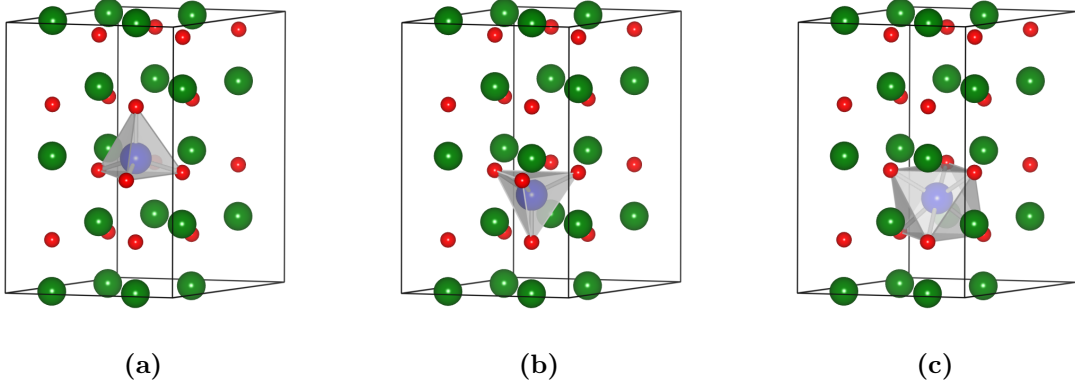


Figure 3.4.: Schematic representation of the ^{57}Fe and ^{111}Cd implantation sites considered in the ZnO structure: substitutional cation site (a), tetragonal interstitial site (b), and octahedral interstitial site (c). The green balls indicate the Zn cations sites, the blue ones the Fe or Cd location site and the red balls the O anions sites.

expansion $G_{max} = 16\sqrt{Ry}$ and the maximum l quantum number for the wave function expansion inside the atomic spheres was confined to $l_{max} = 12$. The number of k points in the whole (irreducible) Brillouin zone was set to 100, 50 and 27 for $2 \times 2 \times 1$, $2 \times 2 \times 2$ and $3 \times 3 \times 2$ SC's respectively. And, the generalized gradient approximation (GGA) due to Perdew *et al.* [80] was applied. The DFT study is done considering *non spin polarized* configurations in both cases, and in order to study the magnetic ordered state properties in the ^{57}Mn (^{57}Fe) implanted samples the *spin polarized* configuration was treated as well.

Finally, the following calculation results are obtained: the magnetic moment, the magnetic hyperfine field (B_{hf}), the electron density present at the probe nucleus position (ρ_0) and the EFG expressed by its main component (V_{zz}) and the asymmetry parameter (η). From ρ_0 , V_{zz} and η the hyperfine electrical parameters of ^{57}Fe (isomer shift (δ) and quadrupole splitting (Δ)) can be obtained using Eqs. (2.66) and (2.70). To express the δ values the same reference of the experiment is used, the bcc Fe (lattice constant $a = 2.865 \text{ \AA}$), giving $\rho_0^{reference} = 15310.102 \text{ a.u.}^{-3}$. For Cd the corresponding quadrupole frequency values, ν_Q , obtained by evaluation of Eq. (2.71), are compared to the experimental reports.

In Table 3.1 the hyperfine parameters reported in [26–28] for ^{57}Mn (^{57}Fe) embedded in ZnO are summarized. As well as, in Table 3.2 the quadrupole hyperfine parameters measured in [25] for ^{111}In (^{111}Cd) into ZnO are presented. These values are taken as a reference for the following comparison with the present calculation results.

Table 3.1.: Hyperfine parameters experimental values (magnetic hyperfine field (B_{hf}), isomer shift (δ), quadrupole splitting (Δ) and lines width (Γ)) reported in [26–28] for ^{57}Fe implanted into ZnO.

Experimental line	B_{hf} (T)	δ (mm/s)	Δ (mm/s)	Γ (mm/s)
D2		0.80(1)	0.3(2)	0.2
D3		0.55(2)	0.73(3)	0.5
Fe_C		0.91(1)	-0.82(1)	–
Fe_D		0.77(1)	-1.6(4)	–
Sextet I	48.3(2)	0.20(2)	0.13(3)	0.6
Sextet II	12(3)	0.82(5)	-0.11(8)	–
Sextet III	37(2)	0.13(4)	-0.83(5)	–

Table 3.2.: Hyperfine parameters experimental values (quadrupole frequency (ν_Q) and width of the frequency distribution (Γ)) reported in [25] for ^{111}In (^{111}Cd) implanted into ZnO.

Experimental Line	ν_Q (MHz)	Γ (MHz)
ν_{Q1}	30.6(3)	3.8
ν_{Q2}	113(2)	74.6

3.3. Results and Discussion

The obtained EFG values for the ZnO ideal crystalline structure parameter are shown in Table 3.3. The individual contributions from s , p and d electrons are also summarized in the table. In Zn and O crystal positions the EFG tensor is axially symmetric ($\eta = 0$) and its symmetry axis is oriented along the $\langle 001 \rangle$ lattice direction. Then, only the EFG principal component (V_{zz}) is analyzed. In this table the EFG measured by high precision nuclear magnetic resonance (NMR) ($V_{zz}(\text{exp.})$) in ZnO samples [126] and the calculated values for this case using HF cluster procedure ($V_{zz}(\text{HF})$) [121] are also shown for comparison.

Table 3.3.: Theoretical electrical field gradient component V_{zz} (in 10^{21} V/m²) calculated for the ZnO crystalline structure. The V_{zz} main electronic contributions are also shown. The previously measured (exp.) and calculated EFG values using HF cluster procedure [121] are also included for comparison.

Site	$V_{zz}(10^{21} \text{ V/m}^2)$					
	V_{zz}^{sd}	V_{zz}^{pp}	V_{zz}^{dd}	V_{zz}^{Total}	$V_{zz}(\text{HF})[121]$	$V_{zz}(\text{exp.})[126]$
Zn	-0.004	0.521	-0.006	0.511	0.73	0.659(2)
O	0.011	-0.258	0.001	-0.270	–	-0.233(1)

The V_{zz} values calculated with the WIEN2k code for the ZnO experimental structure parameters show a good agreement with measured values [126]. From the table it is also clear that the dominant contribution to the EFG in Zn and O atoms comes from electrons with strong p character. The $V_{zz}(\text{HF})$ value for Zn becomes closer to $V_{zz}(\text{exp.})$ than the here presented results; but in the present study the hyperfine electric parameters were calculated for both Zn and O sites.

3.3.1. Results for ^{57}Mn (^{57}Fe) into ZnO

The optimized ZnO lattice parameters considering the Fe located in a cation substitutional position of the crystal are shown in Table 3.4 for the three SC's configurations studied. Both parameters (a and c) are less than 1 % bigger than the experimental values and in the same range of other DFT studies [127]. The parameters shown on this table present a close to linear behavior with the Fe concentration in the sample, as is indicated in Fig 3.5 for the $d_{\text{Fe-O}}$ case. Extrapolating the values presented in the table to the infinite dilution of Fe in ZnO (Fe concentration for $x \rightarrow 0$) shows that the $x = 2.8\%$ configuration is an adequate representation of this case, because it has a , c and $d_{\text{Fe-O}}$ values that are maximum 0.4 % different from the $x \rightarrow 0$ ones, furthermore the $d_{\text{Fe-Fe}}$ value is 5.1 % smaller. On the other hand, the concentrations cases of $x = 12.5$ and 6.2% have $d_{\text{Fe-Fe}}$ values that are respectively 49.6 and 36.9 % smaller, indicating that these configurations are more representative of concentrated $\text{Zn}_{1-x}\text{Fe}_x\text{O}$ solid solutions than an infinite dilution of Fe into ZnO.

Table 3.4.: Optimized $\text{Zn}_{1-x}\text{Fe}_x\text{O}$ lattice parameters (a and c) obtained for the different Fe doping levels studied in the three given SC configurations. The minimum distance obtained between Fe atoms ($d_{\text{Fe-Fe}}$) and between Fe and the near neighborhood O atoms ($d_{\text{Fe-O}}$) for each case is also reported.

Composition	Supercell	$a(\text{\AA})$	$c(\text{\AA})$	$d_{\text{Fe-Fe}}(\text{\AA})$	$d_{\text{Fe-O}}(\text{\AA})$
$\text{Zn}_{0.875}\text{Fe}_{0.125}\text{O}$	2x2x1	3.277	5.241	5.24	1.91(1)
$\text{Zn}_{0.938}\text{Fe}_{0.062}\text{O}$	2x2x2	3.282	5.250	6.56	1.89(1)
$\text{Zn}_{0.972}\text{Fe}_{0.028}\text{O}$	3x3x2	3.287	5.285	9.86	1.88(1)
$\text{Zn}_{0.95}\text{Fe}_{0.05}\text{O}^\ddagger$		3.255	5.207		

‡ Experimental report [31].

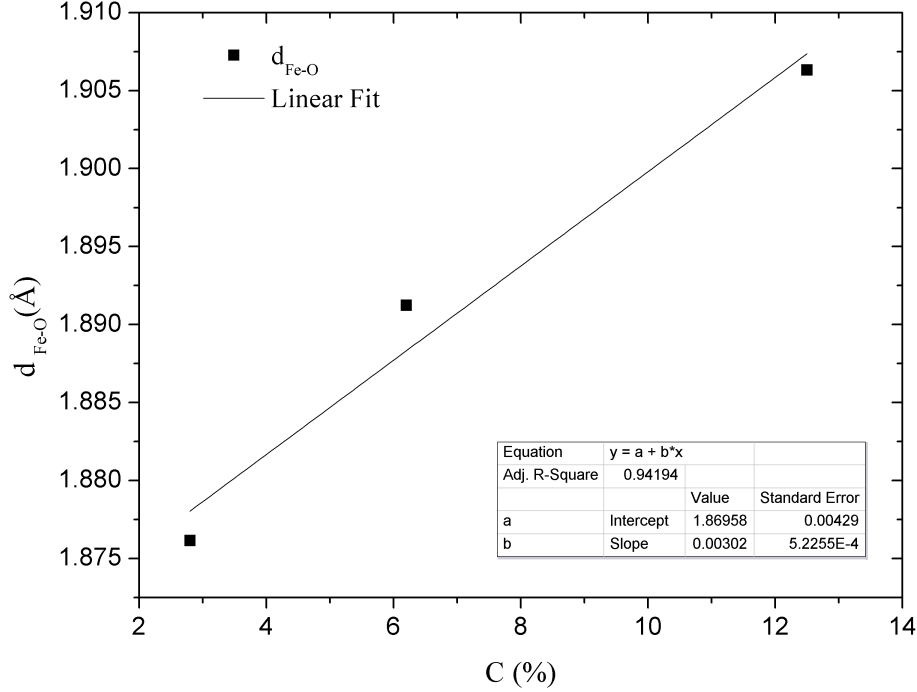


Figure 3.5.: Behavior of d_{Fe-O} with the Fe concentration in the ZnO samples. The linear regression is indicated by the solid line.

The calculated hyperfine parameters for the ^{57}Mn (^{57}Fe) configurations under study are shown in Table 3.5. The largest EFG component (V_{zz}) will be analyzed; because in most of the cases the EFG tensor is axially symmetric ($\eta = 0$). Only some vacancy configurations present $\eta \neq 0$ that were considered in the Δ value. The EFG symmetry axis is oriented along the $\langle 001 \rangle$ lattice direction in most cases, except when presence of a vacancy is considered. In those cases the EFG axis orientation depends on the vacancy position.

The values of Table 3.5 indicate that, in general, for all configurations the hyperfine parameters depend strongly on the distance between nearest Fe atoms, making it difficult to establish a unique relationship among the calculated values and the experimental observations. Nevertheless, some comparisons can be made. As it was already mentioned, the configurations where the Fe is less concentrated ($x = 2.8\%$) are generally the ones where the results can be extended to real embedded (in the low concentration limit) Fe in ZnO cases, because the influence of one Fe atom on other Fe ones is minimal; but as it was reported by Gu *et al.* [124], the Fe atoms in ZnO can tend to form pairs. Therefore, this possibility of configuration with shorter d_{Fe-Fe} is also considered in the

Table 3.5.: Theoretical hyperfine parameters, magnetic hyperfine field B_{hf} (T), electric field gradient V_{zz} (10^{21} V/m²), quadrupole splitting Δ (mm/s) and isomer shift δ (mm/s) values for the Fe studied implantation sites in ZnO. According to the distance between near Fe atoms d_{Fe-Fe} (Å) and between Fe and a cation vacancy $d_{V_{Zn}}$ (Å).

Site	d_{Fe-Fe}	$d_{V_{Zn}}$	non spin polarized			spin polarized			
			V_{zz}	Δ	δ	B_{hf}	V_{zz}	Δ	δ
Fe _{sub}	5.24	-	1.226	0.20	0.69	-26.9	-0.040	-0.01	0.64
	6.56	-	4.966	0.83	0.64	-27.7	-0.685	-0.11	0.57
	9.86	-	3.026	0.50	0.55	-29.4	0.137	0.02	0.46
Fe _{tet}	5.24	-	-0.724	-0.12	0.27	-19.6	-8.189	-1.36	0.27
	6.56	-	0.953	0.16	0.52	-24.0	-3.116	-0.51	0.54
	9.86	-	1.830	0.30	0.48	-25.8	-3.975	-0.66	0.62
Fe _{oct}	5.24	-	-4.262	-0.71	0.78	-29.6	1.771	0.29	0.79
	6.56	-	-5.835	-0.97	0.73	-30.5	0.897	0.15	0.73
	9.86	-	-0.925	-0.15	1.02	-24.3	6.888	1.15	1.08
Fe _{sub} -V _{Zn}	5.24	≈3.3	6.311	1.19	0.10	-20.2	5.965	0.99	0.08
	6.56	≈5.2	3.528	0.59	0.21	-25.7	8.320	1.38	0.27
	9.86	≈7.8	0.239	0.04	0.15	-26.6	-0.692	-0.12	0.15
Fe _{tet} -V _{Zn}	5.24	≈3.9	-7.860	-1.31	0.43	-16.2	-9.365	-1.56	0.57
	6.56	≈5.8	-2.476	-0.41	0.34	-21.5	-2.033	-0.34	0.67
	9.86	≈8.7	-0.850	-0.16	0.33	-18.0	9.805	1.63	0.67
Fe _{oct} -V _{Zn}	5.24	≈3.9	-1.241	-0.21	0.71	-28.2	-6.405	-1.06	0.70
	6.56	≈5.4	-12.91	-2.15	0.61	-34.4	-1.614	-0.27	0.60
	9.86	≈7.6	-0.932	-0.18	0.92	-28.7	-6.253	-1.16	0.82

analysis. In the case of the spin polarized configurations the correlation of the spectral lines with certain implantation configurations is done on the base of the electric hyperfine parameters (Δ and δ); because the hyperfine magnetic field values (B_{hf}) are not well reproduced in the current approach (see Table 3.5). Additional approximations and corrections should be taken into account in future studies.

In Fig. 3.6 the dependence of δ values with the Fe–O average bond distance is shown for the Fe located at the cation substitutional site in ZnO. It presents a near to linear

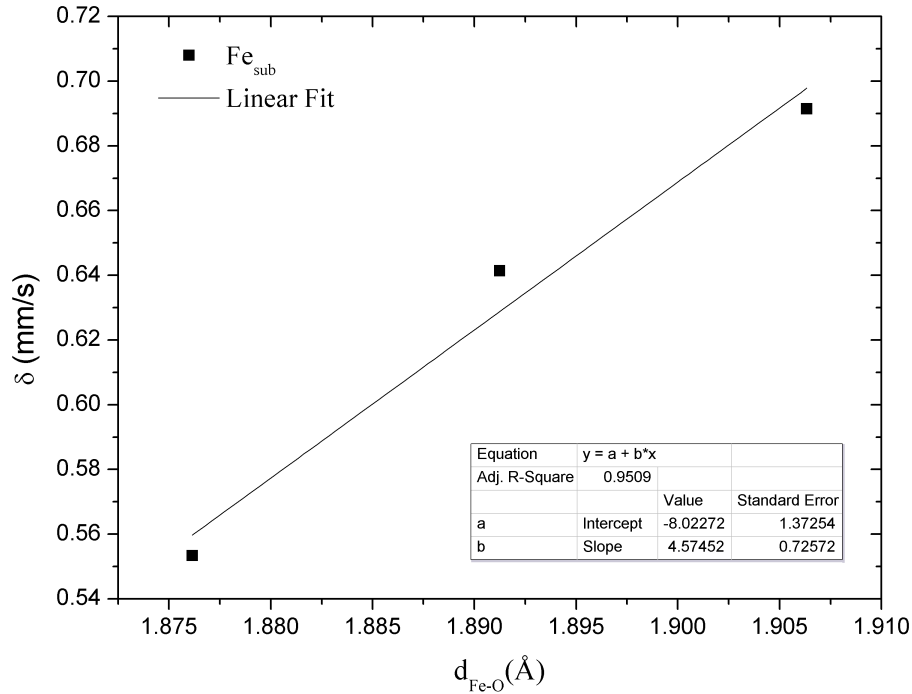


Figure 3.6.: Dependency of δ values with the Fe–O average bonds distance for Fe located at the cation substitutional site of ZnO.

behavior, as indicated by the linear fit in the graph. Evaluating this linear relation for the $d_{\text{Fe-O}}$ value that correspond with the infinite dilute system give $\delta = 0.53 \text{ mm/s}$ which is close to the value obtained for the calculated smallest Fe concentration ($x = 2.8\%$). This represents another confirmation of the proper description of an infinite dilute system by the bigger SC here considered.

In Fig. 3.7 a graphical comparison among the experimental data and the calculated values corresponding to the different considered configurations is established. In each case, the calculated δ and Δ values for each configuration are represented by a symbol, and each experimental line is represented by a square which sides correspond to the experimental line width. This comparison shows a clear correlation between the experimental lines and some of the calculated configurations, which will be analyzed in detail.

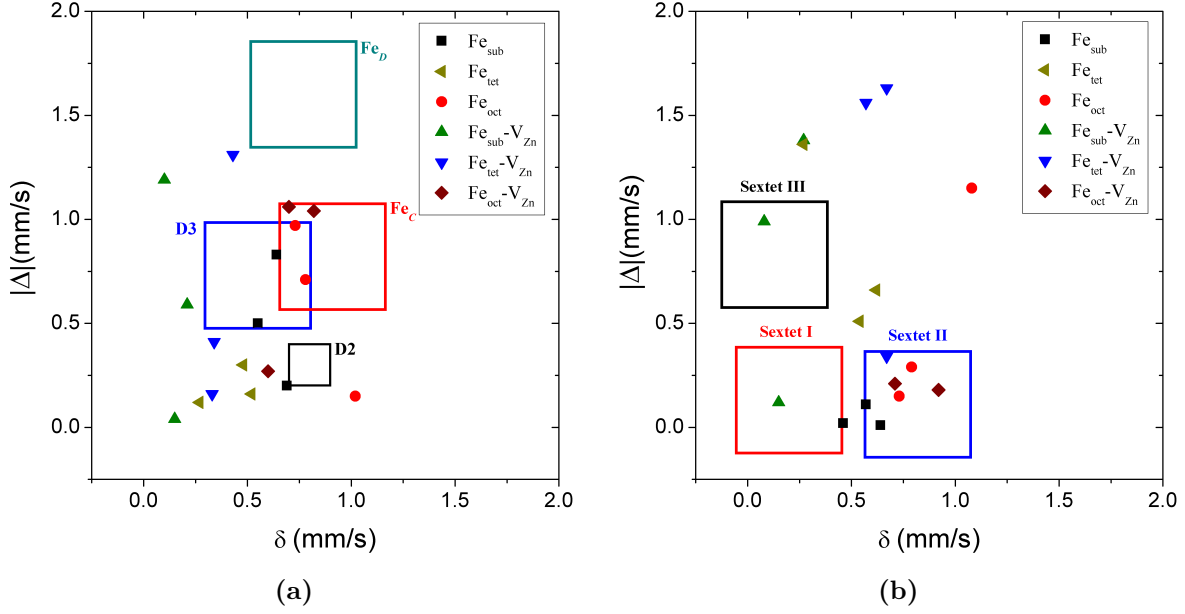


Figure 3.7.: Comparison between experimental and calculated hyperfine parameters Δ and δ for ZnO implanted or doped with ^{57}Fe : a) *non spin polarized* configurations and b) *spin polarized* configurations. Each experimental line is represented by a square which sides correspond to the experimental line width.

Table 3.6.: Correlation between the experimental reports for ZnO implanted with ^{57}Fe and the studied configurations, comparing the hyperfine electric parameters values.

Experimental Line	Theoretical Configurations
D2	Fe_{sub}^n
D3	$\text{Fe}_{\text{sub}}^{m,f}, \text{Fe}_{\text{oct}}^{n,m}$
Fe _C	$\text{Fe}_{\text{oct}}^{n,m}, \text{Fe}_{\text{oct}-\text{V}_{\text{Zn}}}^{n,f}$
Fe _D	$\text{Fe}_{\text{tet}-\text{V}_{\text{Zn}}}^n$
Sextet I	$\text{Fe}_{\text{sub}-\text{V}_{\text{Zn}}}^f, \text{Fe}_{\text{sub}}^f$
Sextet II	$\text{Fe}_{\text{oct}-\text{V}_{\text{Zn}}}^{n,f}, \text{Fe}_{\text{oct}}^{n,m}, \text{Fe}_{\text{sub}}^{n,m}$
Sextet III	$\text{Fe}_{\text{sub}-\text{V}_{\text{Zn}}}^n$

ⁿNearest distances: $d_{\text{Fe}-\text{Fe}} = 5.24 \text{ \AA}$ and $3.3 \text{ \AA} \leq d_{\text{V}_{\text{Zn}}} \leq 3.9 \text{ \AA}$ (if vacancy present).
^mIntermediate distances: $d_{\text{Fe}-\text{Fe}} = 6.56 \text{ \AA}$ and $5.2 \text{ \AA} \leq d_{\text{V}_{\text{Zn}}} \leq 5.8 \text{ \AA}$ (if vacancy present).
^fFar distances: $d_{\text{Fe}-\text{Fe}} = 9.86 \text{ \AA}$ and $d_{\text{V}_{\text{Zn}}} > 7.6 \text{ \AA}$ (if vacancy present).

In Table 3.6 the resulting hyperfine parameters correlation between the observed Mössbauer experimental lines and the analyzed configurations is presented. The Fe_{sub} configuration with the shortest distance $d_{\text{Fe}-\text{Fe}}$ presents electric hyperfine parameters in agreement with the doublet D2, that is experimentally associated with the Fe in that position [28]. This result also agrees with the already mentioned statement of Gu *et al.* [124]; that the Fe doped ZnO has a ground state configuration of Fe atoms when they form pairs with a separation of $\approx 5.3 \text{ \AA}$. This is also well related with the report done by Weyer *et al.* [28] that the D2 doublet is dominant at high temperatures (over 700 K), in which case it is possible that the Fe atom diffusion and defects annealing can enhance this pair formation mechanism.

The D3 experimental Mössbauer doublet is also in agreement with the Fe_{sub} site but with a greater distance between Fe atoms (6.56 \AA), this comparison also seems to agree with the experimental findings done in [31] for a $\text{Zn}_{0.95}\text{Fe}_{0.05}\text{O}$ sample where the average distance between Fe atoms should be in the same range and the doublet D3 also appears. This line is additionally in partial agreement with the Fe_{oct} site, which might mean that this doublet could also be related with an interstitial configuration. The attribution of this line to both sites could be linked with the fact reported in [28], that when the sample is annealed the doublet D3 population decrease and the D2 increases. This behavior might also be related to the previous correlation of doublet D2 to the minimal energetic configuration of Fe in ZnO [28, 124]. Then, it could be possible that during the annealing process the Fe atoms located in the interstitial and substitutional sites ascribed to the D3 doublet diffuse and take the minimal energy configuration that corresponds to the D2 line as was explained before.

The doublet Fe_C reported in [26] is in good agreement with the hyperfine parameters obtained for the Fe_{oct} and $\text{Fe}_{oct}-V_{\text{Zn}}$ configurations. This can be also justified by the fact that a high irradiation fluence could produce more interstitial implantation sites, including also vacancies, in the material. The second contribution observed in [26], Fe_D , presented a wide distribution of Δ values, nevertheless no clear correlation is found with the studied configurations, only the $\text{Fe}_{tet}-V_{\text{Zn}}$ interstitial configuration is in its proximity. In conclusion, this doublet spread seems to be produced by probe atoms located in interstitial sites with different defect complexes configurations around it. Further studies will be necessary to clarify the possible origin of the Fe_D doublet.

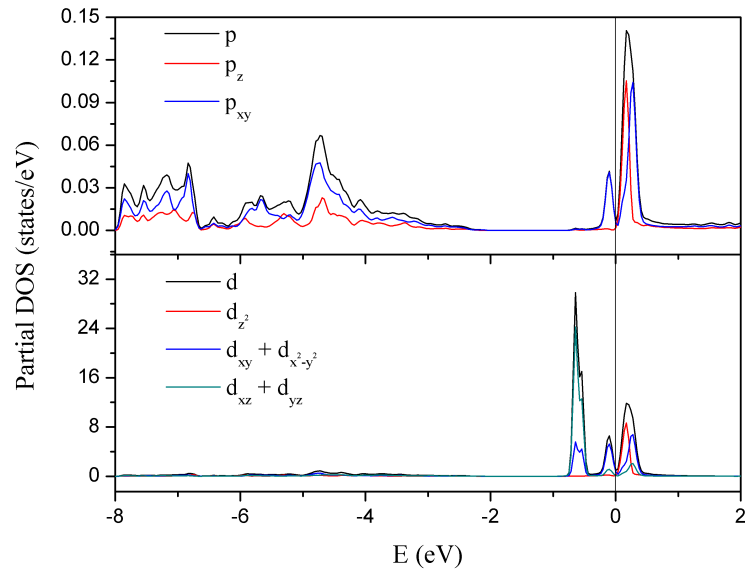
The main sextet line reported in [28] (Sextet I) presents an acceptable agreement with the Fe_{sub} and $\text{Fe}_{sub}-V_{\text{Zn}}$ configurations hyperfine electric parameters in the more dilute cases ($x = 2.8 \%$) and with a vacancy in the third vicinity ($d_{V_{\text{Zn}}} \approx 7.8 \text{ \AA}$). The Sextet III

Table 3.7.: Contributions to V_{zz} from a given type of electronic states of harmonic character l for the main ^{57}Fe implantation configurations studied in ZnO.

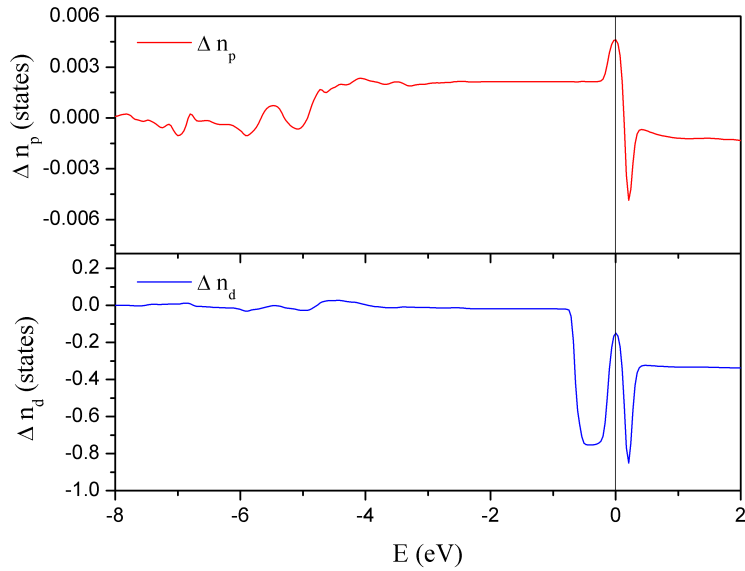
Site	$V_{zz}^l (10^{21} \text{ V/m}^2)$			
	V_{zz}^{sd}	V_{zz}^{pp}	V_{zz}^{dd}	V_{zz}^{Total}
Fe_{sub}	-0.013	1.333	3.702	5.007
Fe_{tet}	-0.056	-23.206	22.176	-1.294
Fe_{oct}	-0.051	7.634	-11.818	-4.163
$\text{Fe}_{sub}-V_{Zn}$	-0.043	-1.963	8.323	6.264
$\text{Fe}_{tet}-V_{Zn}$	-0.026	-20.804	12.577	-8.399
$\text{Fe}_{oct}-V_{Zn}$	-0.031	9.502	-22.389	-12.809

also seems to agree with the $\text{Fe}_{sub}-V_{Zn}$ configuration but when the Fe atoms are more close to each others ($\approx 5.2 \text{ \AA}$) and the vacancy is located in the first vicinity. On the other hand, Sextet II presents various possible contributions, the Fe_{sub} and the Fe_{oct} sites in a solid dilution configuration, and also with the Fe_{oct} interstitial site including a vacancy. These results are consistent with the experimental reports [27, 28], namely that the Fe can stabilize a vacancy in the second or third neighborhood and that complex configurations including defects can appear in these cases.

The contributions to V_{zz} from a given type of electronic states of harmonic character l , estimated using Eq. (2.72), are presented in Table 3.7. It is clear that in all cases the main contribution to V_{zz} comes from electrons with strong p and d character.



(a)



(b)

Figure 3.8.: Partial density of states (PDOS) for p and d electrons present in the Fe_{sub} site on ZnO (a), p and d electron anisotropies (Δn_p and Δn_d) (b). The Fermi energy is at 0 eV.

In all cases a step behavior is found around the Fermi level of the p and d electron anisotropies (Δn_p and Δn_d), calculated by Eqs. (2.73) and (2.74). Fig 3.8 presents the partial density of states (PDOS) and the electron anisotropies calculated for the Fe_{sub} configuration site on ZnO. This step behavior supports the experimental dependency found of the hyperfine parameters, especially Δ [26, 28–31], with the measurement temperature.

The calculated magnetic moments of transition metals and oxygen atoms for the different studied implantation configurations in $\text{Zn}_{0.972}\text{Fe}_{0.028}\text{O}$ are shown in Table 3.8. The main contribution to the total magnetic moment comes from Fe atoms, representing more than the 70% in all cases. The rest contribution comes from the O atoms near the Fe. The other O and Zn atoms have no contribution to the magnetization. It is interesting that for the interstitial sites the presence of vacancies increases up to 35 % the Fe and total magnetic moments. For all the studied configurations the calculated total magnetic moments are in the reported experimental range [28].

Table 3.8.: Calculated magnetic moments of atoms in $\text{Zn}_{0.972}\text{Fe}_{0.028}\text{O}$ for the different studied implantation configurations, including the presence of cation vacancies.

Config.	Magnetic Moment (μ_B)				
	Zn	Fe	O(near Fe)	O(others)	Total
Fe_{sub}	< 0.01	3.67	0.15	< 0.01	4.77
Fe_{tet}	< 0.01	2.65	0.12	< 0.01	3.12
Fe_{oct}	< 0.01	3.05	0.05	< 0.01	3.63
$\text{Fe}_{sub}\text{-V}_{Zn}$	< 0.01	3.27	0.15	< 0.01	4.51
$\text{Fe}_{tet}\text{-V}_{Zn}$	< 0.01	3.15	0.16	< 0.01	4.13
$\text{Fe}_{oct}\text{-V}_{Zn}$	< 0.01	3.26	0.14	< 0.01	4.03
Exp.					3 – 5

3.3.2. Results for ^{111}In (^{111}Cd) into ZnO

In the studied Cd configurations, the EFG tensor is axially symmetric ($\eta = 0$) and its symmetry axis is oriented along the $\langle 001 \rangle$ lattice direction for the ideal sites; while for some vacancy configurations $\eta \neq 0$ and the EFG is randomly oriented, as previously discussed for Fe. The EFG components (V_{zz} and η) and the corresponding quadrupole frequency (ν_Q) calculated values for the studied Cd implantation sites are indicated in Table 3.9. These values shows a dependency with the distance between implanted Cd ions and with the presence of Zn vacancies.

Table 3.9.: Theoretical EFG components (V_{zz} and η) and the quadrupole frequency (ν_Q) values for the studied Cd implantation sites in ZnO, according to the distance between near Cd atoms $d_{\text{Cd}-\text{Cd}}$ and between Cd and the cation vacancy $d_{\text{V}_{\text{Zn}}}$.

Site Config.	$d_{\text{Cd}-\text{Cd}}$ (Å)	$d_{\text{V}_{\text{Zn}}}$ (Å)	V_{zz} ($10^{21}\text{V}/\text{m}^2$)	η	ν_Q (MHz)
Cd_{sub}	6.50	-	1.38	0	27.8
	9.75	-	1.57	0	31.4
Cd_{tet}	6.50	-	-9.48	0	190.2
	9.75	-	-10.24	0	205.5
Cd_{oct}	6.50	-	-1.00	0	20.1
	9.75	-	4.27	0	85.6
$\text{Cd}_{\text{sub}}-\text{V}_{\text{Zn}}$	6.50	≈ 3.2	1.68	0.07	33.7
	9.75	≈ 7.7	1.12	0	22.6
$\text{Cd}_{\text{tet}}-\text{V}_{\text{Zn}}$	6.50	≈ 5.2	-11.87	0	238.3
	9.75	≈ 8.6	-10.64	0.09	213.6
$\text{Cd}_{\text{oct}}-\text{V}_{\text{Zn}}$	6.50	≈ 4.8	8.83	0	177.3
	9.75	≈ 7.5	5.82	0.24	116.9

Fig. 3.9 shows a graphical comparison between the experimental and calculated quadrupole frequency in ZnO samples implanted with ^{111}In (^{111}Cd). The measured values with error bars represent the experimental lines and their respective widths. The comparison of the calculated and experimental values is shown separately for the substitutional and interstitial sites.

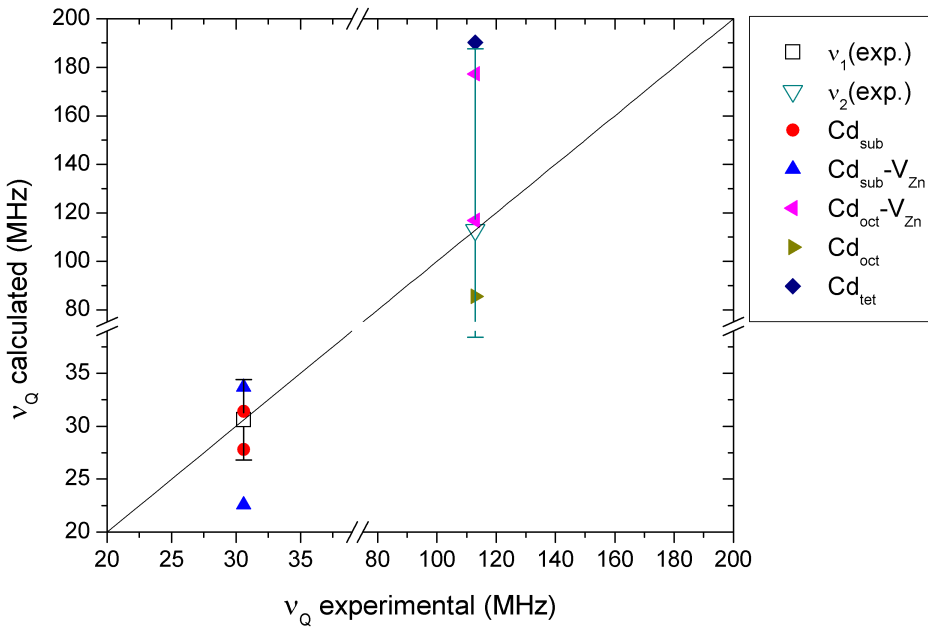


Figure 3.9.: Comparison between experimental and calculated hyperfine parameter: quadrupole frequency (ν_Q), for ZnO implanted with ^{111}Cd . The solid line shows the ideal match between the theoretical results and the experiment.

The observed correspondence of these calculated values with the experimental lines (see Table 3.2) is summarized in Table 3.10. For the cation substitutional site (Cd_{sub}) the ν_Q calculated values are closer to the experimental line ν_{Q1} in comparison to the values calculated for the interstitial sites (Cd_{oct} and Cd_{tet}). The $\text{Cd}_{\text{sub}}-\text{V}_{\text{Zn}}$ configuration present also ν_Q values close to this experimental line and a close to zero asymmetry parameter. The difference between the ν_{Q1} and the values for Cd_{sub} site are around 2.6 to 9.1 %, while it rises for both interstitial sites to over 30 %. The better agreement is found for the 3x3x2 SC, which is more representative of a dilute Cd implantation in ZnO, as in the experiment, and similar to the Fe previous case. On the other hand, the experimental line ν_{Q2} is in good agreement with the Cd_{oct} and $\text{Cd}_{\text{oct}}-\text{V}_{\text{Zn}}$ implantation sites. These correspondence could represent some of the local environments that characterize the ν_{Q2}

line because the formation of interstitial sites and local defects complex around it is more probable during the implantation process, when this line is observed. The observed correspondence for ν_{Q1} and ν_{Q2} also agree with the annealing behavior of these lines [25].

Table 3.10.: Correlation between the experimental reports for ZnO implanted with ^{111}Cd and the studied configurations, comparing the EFG values.

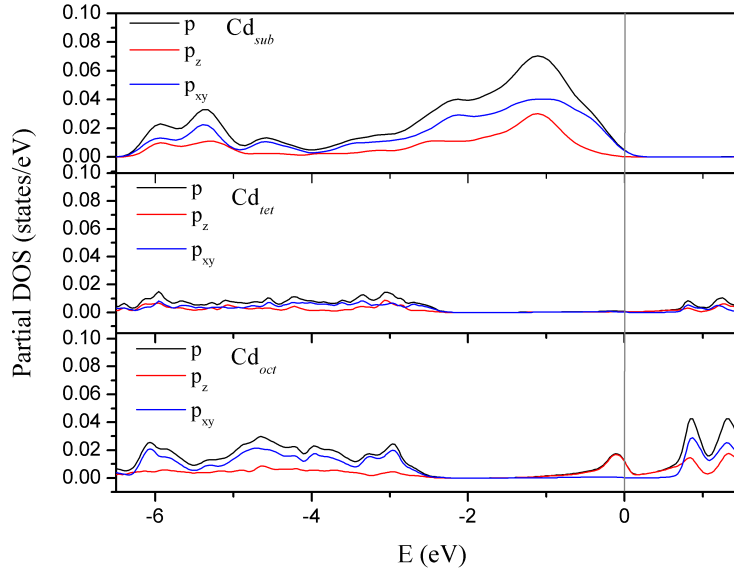
Experimental Line	Theoretical Configurations
ν_{Q1}	$\text{Cd}_{sub}, \text{Cd}_{sub}\text{-V}_{Zn}$
ν_{Q2}	$\text{Cd}_{oct}, \text{Cd}_{oct}\text{-V}_{Zn}$

From Table 3.11 is clear that the main contribution to the V_{zz} values of Cd atoms comes from electrons with a strong p -character. The partial DOS for the p electrons of Cd incorporated in ZnO and the p electrons anisotropy (Δn_p) as function of energy are shown in Figure 3.10 for the studied implantation sites. The Δn_p value at the Fermi energy is positive in the Cd_{sub} site and negative in the other two cases. This is perfectly consistent with the V_{zz}^{pp} sign observed in those cases. This implies that for the Cd_{sub} site the largest contribution to V_{zz}^{pp} comes from p_{xy} electrons and for the Cd_{oct} and Cd_{tet} sites comes from the p_z electrons. The Δn_p steep behavior observed in the Cd_{sub} and Cd_{oct} cases near the Fermi energy suggest that the EFG of Cd occupying these sites could be sensitive to small Fermi level changes due to temperature variations or other effects.

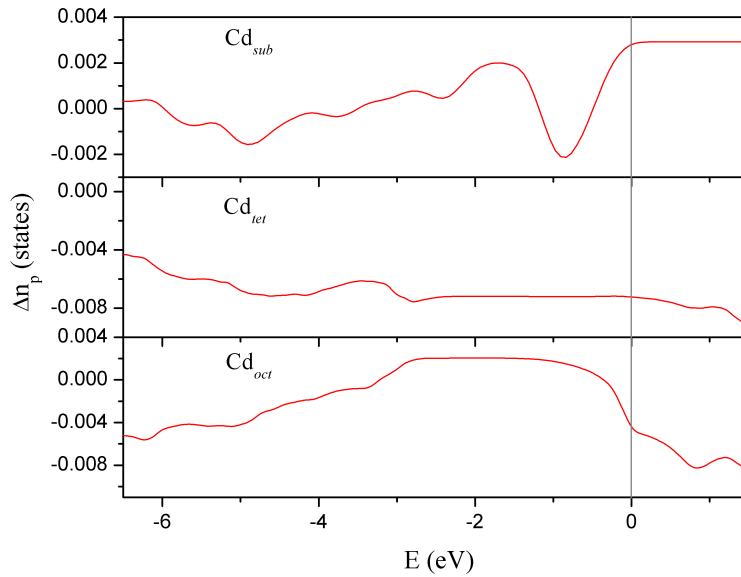
Table 3.11.: Contributions to V_{zz} from a given type of electronic state of harmonic character l for the studied ^{111}Cd implantation sites.

Site	$V_{zz}^{ll} (10^{21} \text{ V/m}^2)$			
	V_{zz}^{sd}	V_{zz}^{pp}	V_{zz}^{dd}	V_{zz}^{Total}
Cd_{sub}	-0.009	1.630	-0.227	1.398
Cd_{tet}	0.206	-12.546	2.892	-9.455
Cd_{oct}	-0.012	-1.691	0.667	-1.046

Regarding the V_{zz} previously reported with the PCM approximation, the values presented here increase the precision in the electronic structure description; giving a better understanding of the EFG origin in the ^{111}In (^{111}Cd) implanted ZnO samples.



(a)



(b)

Figure 3.10.: Partial density of states (PDOS) for p electrons present in the Cd sites of ZnO (a), and p electrons anisotropy (Δn_p) (b). The Fermi energy is at 0 eV.

3.4. Conclusions

The V_{zz} values calculated with the WIEN2k code for the ZnO experimental structure parameters show a good agreement with measured values for both Zn and O sites [126]. The hyperfine parameters and the magnetic properties of ZnO samples implanted and doped with ^{57}Fe , including some defect configurations were also calculated. A good agreement of the obtained hyperfine parameters in the studied configurations with the doublets and sextets reported in [26–28] was found.

The doublet D2 seems to be correlated with the Fe in a substitutional cation site forming Fe pairs with $d_{\text{Fe}-\text{Fe}} \approx 5.3 \text{ \AA}$. The doublet D3 is also in agreement with the Fe substitutional cation site but with a larger distance between them and, also, with the octahedral interstitial site. This correlation is also supported by the hyperfine parameters behavior observed during the samples annealing [28]. The doublet Fe_C reported in [26] appears to be related with the octahedral interstitial site and with this site including vacancies; while the Fe_D doublet is not clearly explained in the present study, but could be related with defect complex where the Fe seems to be located in the tetrahedral interstitial site.

The main sextet (Sextet I) seems to be originated from a dilute substitutional site, including also the presence of vacancies between the second and third neighborhoods, in agreement with the experimental observation. The Sextet III presents a good agreement also with the substitutional site but with vacancies in the near neighborhoods. And, the Sextet II could be correlated with substitutional and octahedral interstitial sites in a magnetic ordered configuration, including this last site with a vacancy. Besides, it seems that the presence of vacancies increases the Fe and total magnetic moments in the sample.

In general, the obtained results agree with the experimental statement that Fe could stabilize a vacancy in the neighborhood of the implantation site in the ZnO material [28]; and that these defects could enhance the Fe magnetic ordered state in this case. It is important to note that the present hyperfine parameters assignment represent some of the possible or probable configurations that might occur in reality, which means that they are not the unique possibility.

The EFG parameters and ν_Q values obtained for various $^{111}\text{In}(^{111}\text{Cd})$ implantation configurations in ZnO samples were studied in details. Three possible $^{111}\text{In}(^{111}\text{Cd})$

implantation configurations were considered: one substitutional incorporation at a cation site and two interstitials; including the presence on Zn vacancies.

Some correlations were found between the proposed configurations and the two experimental lines observed. The obtained ν_Q values for the cation substitutional configuration and this site including a cation vacancy are in good agreement with the experimental component ν_{Q1} . The second measured line ν_{Q2} could be represented by the ^{111}Cd located in the octahedral interstitial site and also by this site including a cation vacancy. Other defects configurations can also occur during the implantation process that can be related with the ν_{Q2} line, but they were not considered here. The obtained results are also in agreement with the observed diminution of the ν_{Q2} component in favor of ν_{Q1} during the sample annealing. Finally, the present electronic structure study suggests a large presence of substitutional incorporation of the ^{111}Cd probe atoms, as well as, is expected that the implanted ^{111}In ions also occupy the ZnO cation site after annealing over 400 °C in ambient nitrogen.

Chapter 4.

Radiation damage and hyperfine parameters calculation results in Si samples implanted with ^{57}Mn (^{57}Fe)

The work presented in this chapter have been published in the following papers: Y. Abreu, C. M. Cruz, I. Piñera, A. Leyva, A. E. Cabal, P. Van Espen and N. Van Remortel. *Hyperfine electric parameters calculation in Si samples implanted with ^{57}Mn (^{57}Fe)*. Physica B, 2014, doi: 10.1016/j.physb.2014.03.028. And, Y. Abreu, C. M. Cruz, P. Van Espen, I. Piñera, A. Leyva and A. E. Cabal. *Multiscale modeling of radiation damage and annealing in Si samples implanted with 57-Mn radioactive ions*. IEEE Nuclear Science Symposium Conference Record, 2011, pp. 1754-1756. doi: 10.1109/NSSMIC.2011.6154676.

4.1. Introduction

The radiation damage produced in silicon (Si) materials by ^{57}Mn (^{57}Fe) ion implantation, at temperatures between 77–500 K, was reported in [17–21]. Those samples were characterized by Mössbauer spectroscopy during implantation observing four main contributions that were attributed to different local configurations of the implanted ions in the Si crystalline structure: substitutional (Fe_s), interstitial (Fe_i) and two damage doublet configurations (Fe_D and Fe_N). The Fe_D doublet is present in the MS at low temperature, while the Fe_N one appears at temperatures above 300 K. Nevertheless, the origin, characteristics and annealing evolution of these two damage configurations is not completely clear and requires, in addition, a complementary study where the

characteristic defects local environments of the probe atoms must be recreated and evaluated.

In the present work some possible implantation configurations are suggested, including defects in the first and second neighborhoods, and its electronic structure is studied in details. Through Monte Carlo simulations the implantation process and the displacement cascades are studied. Then, the electronic structure of the proposed configurations is studied by the density functional theory (DFT) establishing the connections between the proposed implantation sites, with different ^{57}Mn (^{57}Fe) neighborhoods, and the measured hyperfine electrical parameters. These results allow a better understanding of the reported hyperfine electrical parameters and their variation during the annealing process [17–21].

4.2. Calculation Details

The implantation of ^{57}Mn ions with 60 keV of energy in a Si target was simulated using the SRIM Monte Carlo code [109]. In Fig. (4.1a) and (4.1b) the obtained ^{57}Mn ion ranges and vacancy generated in the target are shown. Considering that the $^{57}\text{Mn}^+$ ions fluence used in the experiment was $10^{12} \text{ ion}/\text{cm}^2$ [20, 21], a maximal vacancies concentration of $\approx 2.2 * 10^{20} \text{ Vac}/(\text{cm}^3)$ can be estimated. The Si density is $\approx 5 * 10^{22} \text{ atom}/\text{cm}^3$, implying an average distance d_{V-V} between vacancies of 16.6 Å and a low radiation damage of $4.4 * 10^{-3}$ DPA are expected. Taking into account that at room-temperature about 99% of the Si crystal damage almost instantly anneals, it can be assumed that vacancies and interstitials induced by the ^{57}Mn implantation and recoil process in the sample are far from each other; and that the more probable implantation configurations should include those where only one of these defects are present. In the present study the analyzed implantation configurations will include the presence of a vacancy, an interstitial atom and the combination of both defects.

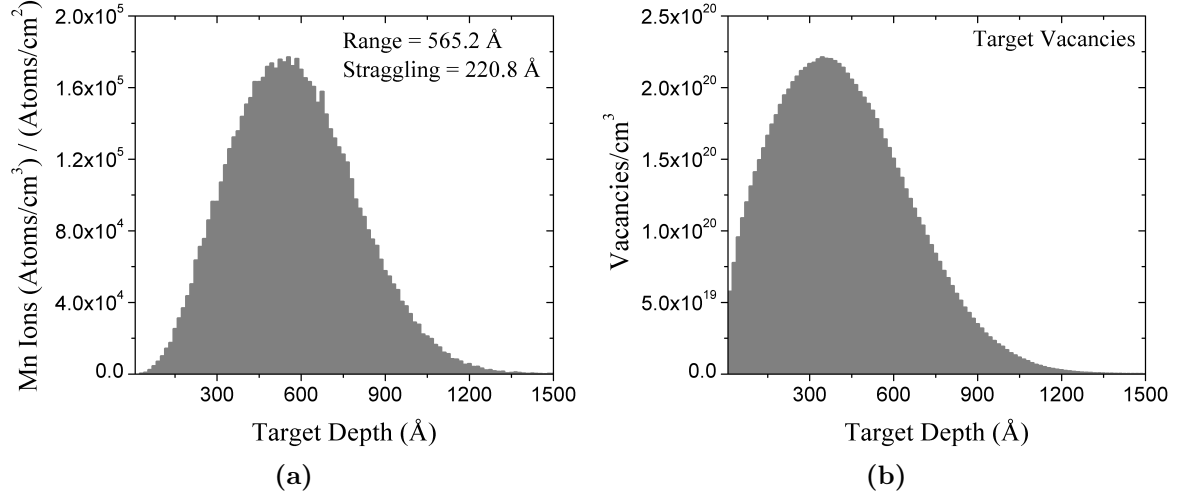


Figure 4.1.: Range of 60 keV Mn ions in the Si target (a) and vacancy generated in the Si target by implantation process (b), simulated by SRIM-2010.

Considering the Si crystal structure [128], the ^{57}Fe ions can be located in two different main sites: substitutional ($\text{Fe}(S)$) and interstitial ($\text{Fe}(I)$). Those sites are represented in Fig. (4.2). From these two main sites several combinations of defect configurations can be created. Among them, the following cases will be considered in the present study.

For the substitutional site:

1. Including a vacancy ($\text{Fe}(S)-V$).
2. Including a Si interstitial ($\text{Fe}(S)-\text{Si}(I)$).
3. Both defects combined ($\text{Fe}(S)-\text{Si}(I)-V$)

For the interstitial site:

1. Including a vacancy ($\text{Fe}(I)-V$).
2. Including a Si atom in other interstitial site ($\text{Fe}(I)-\text{Si}(I')$).
3. Both defects combined ($\text{Fe}(I)-\text{Si}(I')-V$)

In those configurations, different distances between the implanted ion and the vacancy ($d_{\text{Fe}-V}$) and between the implanted ion and the Si interstitial ($d_{\text{Fe}-\text{Si}_I}$) are studied. In each case, the $d_{\text{Fe}-V}$ value represents the distance from the implanted Fe cation to a chosen representative position where the vacancy is created, among several possible non equivalent ones in different vicinities. The $d_{\text{Fe}-\text{Si}_I}$ value is the distance to the site where

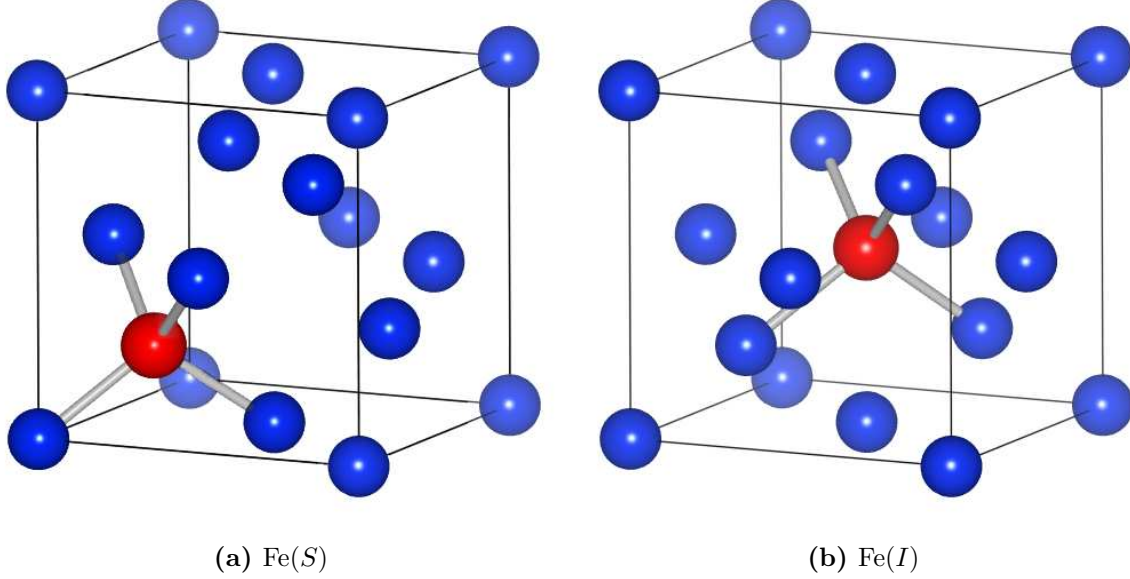


Figure 4.2.: Representation of the main Si crystalline sites where the ^{57}Mn (^{57}Fe) ions can be located: (a) substitutional ($\text{Fe}(S)$), (b) interstitial ($\text{Fe}(I)$). The red balls indicates the Fe atoms and the blue balls the Si atoms.

the interstitial atom is located after the structure optimization. The configurations can be classified as centered or expanded, when the defects are located respectively in the Fe first vicinity or not. Starting from the Si cubic crystal structure [128], a $2 \times 2 \times 2$ supercell (SC) is constructed to reproduce the analyzed local implantations and defects configurations.

The electronic structure of the proposed configurations is studied with the WIEN2k code [129] based on the DFT approach. Good convergences of the hyperfine electrical parameters were found in the calculations with the following set of parameters. The non-overlapping muffin-tin spheres radii R_{mt} were set to 2.3 and 2.0 a.u. for Fe and Si respectively. For the interstitial region, the plane wave expansion was carried out with a cut-off value of $R_{mt}K_{max} = 7.0$. The maximum multipolarity quantum number was confined to $l_{max} = 12$, for the wave function expansion within the atomic sphere. The electrical charge density was Fourier expanded up to $G_{max} = 16\sqrt{Ry}$. The number of k -points in the irreducible part of the Brillouin zone was set to 44 for the $2 \times 2 \times 2$ SC's. And to describe the exchange and correlation effects, the generalized gradient approximation (GGA) due to Perdew *et al.* [80] was used.

The code computes the EFG tensor, expressed in its main component V_{zz} and the asymmetry parameter η , and the electronic concentration present at the nucleus position

ρ_0 . From these quantities the hyperfine electrical parameters (isomer shift (δ) and quadrupole splitting (Δ)) can be obtained using Eqs. (2.66) and (2.70). The bcc Fe was taken as reference [130] in Eq.(2.66), like in the experimental measurements. Then, it was calculated with the same R_{mt} of 2.3 a.u. and 286 k points in the irreducible Brillouin zone, giving $\rho_0^{reference} = 15309.887649 \text{ a.u.}^{-3}$.

Within this approach, the Si lattice parameters including the Fe atom presence were optimized by minimizing the total energy as function of volume. The optimized lattice parameter obtained for the studied SC stoichiometry $\text{Si}_{0.98}\text{Fe}_{0.02}$ in the main substitutional configuration is $a = 5.4646 \text{ \AA}$. This lattice parameter was used in all the studied configurations and the internal atomic positions were also minimized to a force limit below 1 mRy/ \AA .

In Table 4.1 the hyperfine electric parameters reported in [17–21] for ^{57}Mn (^{57}Fe) implanted in Si are summarized; used as reference for the comparison with the present calculation results.

Table 4.1.: Experimental values of isomer shift (δ), quadrupole splitting (Δ) and line width (Γ) reported in [17–21] for ^{57}Mn (^{57}Fe) implanted in Si.

Experimental Line	$\delta(mm/s)$	$\Delta(mm/s)$	$\Gamma(mm/s)$
Fe_s	-0.06(2)	–	0.12(2)
Fe_i	0.76(2)	–	0.12(2)
Fe_D	0.33(3)	1.02(3)	–
Fe_N	0.48(4)	0.38(4)	0.27(4)

4.3. Results and Discussion

The calculated hyperfine electrical parameters values and the relative configuration energy of each analyzed case are shown in Table 4.2. The EFG asymmetry parameter η is null in all the studied configurations as expected from Fe local configuration and Si crystal structure symmetries.

Table 4.2.: Relative configuration energy ($\Delta E(eV)$), calculated isomer shift (δ) and quadrupole splitting (Δ) values for the studied configurations of Fe implanted in Si. According to the distance between Fe and a vacancy d_{Fe-V} (\AA) and between Fe and a Si interstitial d_{Fe-Si_I} (\AA). Previous reported hyperfine values are included for comparison (δ^* and Δ^*). The hyperfine parameters are expressed in mm/s . The energy of the most stable configuration is used as reference (set to 0).

Config.	d_{Fe-V}	d_{Fe-Si_I}	ΔE	δ	Δ	δ^*	Δ^*
Fe(S)	–	–	–	-0.06	<0.01	0.13 ^a , -0.06 ^b	–
Fe(S)-V	2.4	–	0	0.35	0.46		
	7.1	–	0.1	-0.09	<0.01		
Fe(S)-Si(I)	–	3.1	0	-0.13	-1.81		
	–	4.9	2.4	-0.11	0.02		
Fe(S)-Si(I)-V	2.4	3.0	0	0.50	1.00		
	2.4	5.4	1.9	0.31	0.67		
Fe(I)	–	–	–	0.72	<0.01	0.89 ^a , 0.63 ^b	–
Fe(I)-V	2.4	–	0	0.44	1.10		
	7.1	–	2.5	0.71	-0.05	0.43 ^c	0.51 ^c
Fe(I)-Si(I')	–	3.0	0	0.47	0.36		
	–	5.5	0.8	0.82	<0.01		
Fe(I)-Si(I')-V	2.4	3.0	0	0.20	0.77		
	2.4	5.7	2.5	0.46	0.49		

^aReported in [63], ^bReported in [131], ^cReported in [17]

Comparing the present results with previous theoretical reports [63, 131, 132], it can be seen that the δ calculated values stay in the same range for the Fe(S), Fe(I) and Fe(I)-V configurations. On the contrary, the Δ value calculated here for Fe(I)-V is approximately two times bigger than the one reported in [17]. This could be related with the fact that in [17] the Fe position in this configuration was displaced in the direction of the vacancy by about $\frac{1}{6}$ of the distance between the interstitial site and the substitutional site; while in the present study the observed displacement in this direction is smaller, approximately $\frac{1}{12}$ after the structural optimization.

In Fig. 4.3 a graphical comparison among the experimental and calculated hyperfine parameters is established, for Si samples implanted with ^{57}Fe . The calculated δ and Δ values for each configuration is represented by a symbol, and each experimental line is represented by a square with sides equal to the respective experimental line widths. The comparison shows a clear correspondence between the experimental lines and some of the calculated configurations, as will be analyzed in detail below.

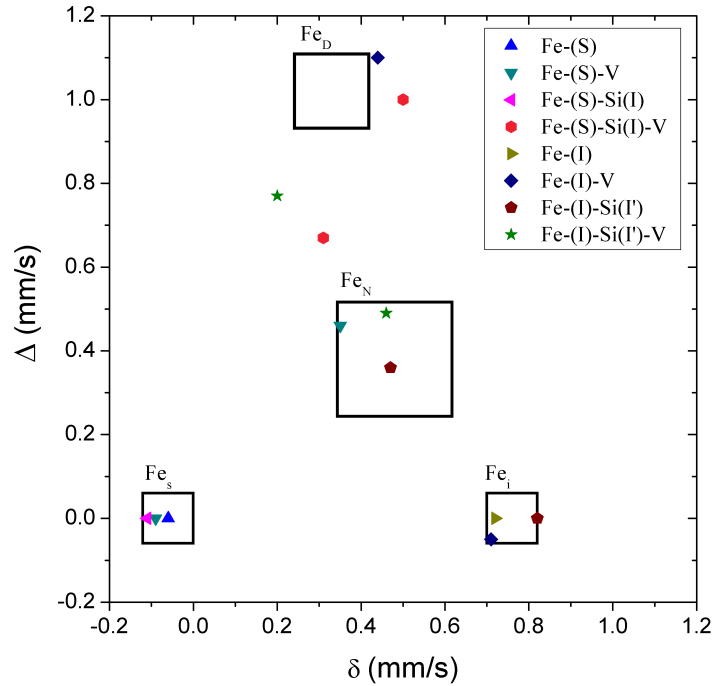


Figure 4.3.: Comparison between experimental and calculated hyperfine parameters δ and Δ for Si implanted with ^{57}Fe . The experimental lines distribution region is represented by a square within the corresponding line width interval.

From the present results one can see that the main substitutional and interstitial configurations ($\text{Fe}(S)$ and $\text{Fe}(I)$) give results close to the experiment for δ values, and a near zero Δ , as expected. This confirms the previously shown correspondence of these two lines to those sites [63, 131]. Furthermore, for the $\text{Fe}(S)-V$, $\text{Fe}(S)-\text{Si}(I)$, $\text{Fe}(I)-V$ and $\text{Fe}(I)-\text{Si}(I')$ configurations, the hyperfine parameters values are close to the ones for primary sites ($\text{Fe}(S)$ and $\text{Fe}(I)$) when the respective vacancy or interstitial is located far from the implantation sites. However, those configurations are not the most energetically stable.

The hyperfine electric parameters of Fe_D spectral component are in relatively good agreement with the $\text{Fe}(I)-V$ and $\text{Fe}(S)-\text{Si}(I)-V$ configurations, when the point defects

are located in the near neighborhood of the implanted Fe site. The agreement is better for Δ , within 8 % maximum difference; but δ values are deviated 33 to 52 % from the experimental one. These configurations are also in the more energetically stable state.

On the other hand, the Fe_N spectral component appears to be well described by configurations $\text{Fe}(S)-V$ and $\text{Fe}(I)-\text{Si}(I')$, when the vacancy or the Si interstitial are located in the first vicinity of ^{57}Fe , being the more energetically stable state of each one. The $\text{Fe}(I)-\text{Si}(I')-V$ configuration is also in agreement with the Fe_N spectral component; but it will be excluded from the analysis because it is in a less stable state, which means that it is less probable to occur. In general these results show that the Si vacancy and interstitial influence on the calculated parameters is more significant when they are located close to the Fe implantation site, as expected. In Table 4.3 the observed correspondence between the Mössbauer experimental lines and the studied configurations is summarized.

Table 4.3.: Correlation between the experimental reports and the studied configurations, comparing the hyperfine electric parameters values.

Experimental Line	Theoretical Configurations
Fe_s	$\text{Fe}(S), \text{Fe}(S)-V^f, \text{Fe}(S)-\text{Si}(I)^f$
Fe_i	$\text{Fe}(I), \text{Fe}(I)-V^f, \text{Fe}(I)-\text{Si}(I')^f$
Fe_D	$\text{Fe}(I)-V^n, \text{Fe}(S)-\text{Si}(I)^n-V^n$
Fe_N	$\text{Fe}(S)-V^n, \text{Fe}(I)-\text{Si}(I')^n$

^fThe point defect is located far from the Fe site.

ⁿThe point defect is located near to the Fe site.

In [20] an interpretation of the temperature dependence of the proposed defect local environments around the ^{57}Fe was introduced. It was based on behavior of the measured Mössbauer spectra components in dependence of the target temperature. This approach involves possible temperature activated migration movements of Si vacancies and interstitial defects, as well as, atom probe site changes from interstitial to substitutional ones. As expected, present results support partially the proposed migration model with a theoretical background. However, new aspects and interpretations about the experimental data have arisen as a contribution of present research to the discussed subject.

According to present calculation, it seems that at low irradiation temperature (77 K) ^{57}Fe implanted ions could occupy mainly interstitial site defect configurations. In this case, it was found that it occupies preferably the $\text{Fe}(I)\text{-}V$ sites, but also $\text{Fe}(I)$ and $\text{Fe}(S)\text{-Si}(I)\text{-}V$ sites with a lower concentration. It follows directly from present results in Tables 4.2 and 4.3, but it was also proposed by Gunnlaugsson et al. (see Fig 4.4).

However, as the sample temperature rises up to 200 K, Si atom thermal diffusive motions start to play a role. On this way, it seems that Si atoms start to occupy Si vacancies in $\text{Fe}(I)\text{-}V$ sites. Hence, the Fe_i site concentration rises. On the other hand, at higher temperature, up to 450 K, in addition to Si diffusive processes, Fe diffusive motions might allow Fe migration from interstitial site I to substitutional position of Si. As a result, the $\text{Fe}(S)$, $\text{Fe}(S)\text{-}V$ and $\text{Fe}(S)\text{-Si}(I)$ configurations rise their populations and Fe_s site concentration increases.

In addition to foregoing migration movements, at temperature above 300 K, the present theoretical interpretations of the experimental observations also confirm the formation of Si defects complex around Fe implantation sites, which was assigned in [20] to the doublet Fe_N . These were simulated here by the calculated configurations $\text{Fe}(S)\text{-}V$ and $\text{Fe}(I)\text{-Si}(I')$. It was here considered, that the vacancy or interstitial Si atom is present in the first vicinity of the ^{57}Mn (^{57}Fe) implantation site. In these cases, it might be mediated through to Si atom and vacancy migration processes at room and higher temperatures. In this way, the proposed annealing behavior could explain the origin of doublet Fe_N , observed at those temperatures, which have hyperfine parameters close to the ones of $\text{Fe}(S)\text{-}V$ and $\text{Fe}(I)\text{-Si}(I')$ configurations.

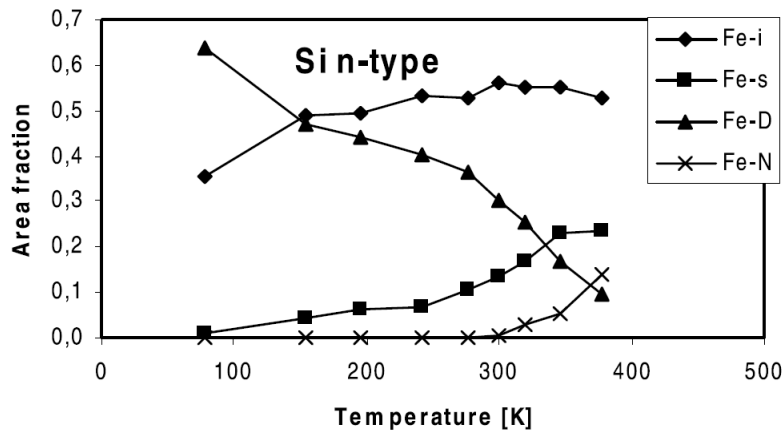


Figure 4.4.: Site populations as function of the measurement temperature during ^{57}Mn (^{57}Fe) implantation into n-type Si. Taken from [20].

4.4. Conclusions

The hyperfine electric parameters of various proposed $^{57}\text{Mn}(^{57}\text{Fe})$ local implantation configurations in Si are calculated and their correspondence with experimental observation is established. The obtained results for the main substitutional and interstitial sites ($\text{Fe}(S)$ and $\text{Fe}(I)$) agree with the corresponding measured values (Fe_s and Fe_i). The presence of ^{57}Fe ions in those Si crystallographic sites, and presumably the ^{57}Mn also, is confirmed, in agreement with previous theoretical reports [63, 131].

The main low temperature damage quadrupole doublet (Fe_D in [20]) could be characterized by configurations where the ^{57}Fe are located in an interstitial or substitutional site with a nearby Si vacancy or a Frenkel pair of defects, respectively. This agreement is also well supported by the observed experimental transition, first from Fe_D to Fe_i and then to Fe_s sites when the sample was annealed between 77 and 450 K, as a result of Fe diffusive motions and Si vacancy-interstitial Frenkel pair direct or indirect annihilation.

The Fe_N spectral line, observed at high temperature, could be related with various defect complex configurations, including the ^{57}Fe located in a substitutional site with a near vacancy, as well as with the ^{57}Fe located in the interstitial site with a Si interstitial atom in the near neighborhood.

The obtained results show that vacancies and interstitials influence the hyperfine parameters more significantly when these defects are located in the first vicinity of the ^{57}Fe implantation site; and that those types of configurations are more energetically stable. In general the proposed damage configurations give a good insight of the highly distorted environments produced by the $^{57}\text{Mn}(^{57}\text{Fe})$ implantation into silicon; and characterize some of the possible local implantation environments.

Chapter 5.

Hyperfine parameters calculations in $\text{YBa}_2\text{Cu}_{3-x}\text{Fe}_x\text{O}_{7-y}$

The work presented in this chapter is related with the following publication: C. M. Cruz, I. Piñera, A. Leyva and Y. Abreu. *Studies on the Gamma Radiation Responses of High Tc Superconductors*. In: Superconductor, Adir Moyses Luiz (Ed.), InTech, 2010, pp. 135-160. doi:10.5772/10122.

5.1. Introduction

The Mössbauer spectra of $\text{YBa}_2\text{Cu}_{3-x}\text{Fe}_x\text{O}_{7-y}$ samples synthesized by high pressure [39–41] and under gamma irradiation [42] present some variations in the measured quadrupole doublet parameters in comparison to the ones observed in the non-irradiated sample synthesized at normal pressure. Namely, the doublet A (see Table 5.1 below) completely disappears as result of the high pressure synthesis, and the population of doublet A decreases in favor of D one due to the ^{60}Co gamma irradiation.

In an initial study [133], we consider the structural defects influence on the quadruple splitting observed values; through the calculation of the EFG components in this situation by the point charge model [46, 133]. Specifically the point defects were taken into consideration through different oxygen configurations, like cluster formation around the ^{57}Fe position and vacancies, as well as trapped electrons near this position, behaving like negative vacancies. Although, the results obtained in [133] clarify that the local configurations near the Fe occupation sites in the crystalline structure are responsible for the observation of several contributions in the Mössbauer spectra of the $\text{YBa}_2\text{Cu}_{3-x}\text{Fe}_x\text{O}_{7-y}$;

it is necessary to carry out this analysis using a better description of the crystal and electronic structure of the material with methods based on better approximations, like DFT.

Then, in the present study, a new theoretical description of the local environments and electronic structure of Fe in the $\text{YBa}_2\text{Cu}_{3-x}\text{Fe}_x\text{O}_{7-y}$ crystalline sites is proposed. The calculations are done using the DFT method within the full-potential (linearized)-augmented-plane-wave plus local orbitals (L/APW+lo) [125] approximation, including the Hubbard correction (GGA+U) [134–137]. Several studies have been reported concerning the $\text{YBa}_2\text{Cu}_3\text{O}_{7-y}$ high T_c superconductor using this method [138–140], even EFG parameters calculations [100, 141], including YBaFe_2O_5 [142], but no report was found for the partially doped $\text{YBa}_2\text{Cu}_{3-x}\text{Fe}_x\text{O}_{7-y}$ material.

Up to now, a complete study and comparison is lacking between the type of oxygen coordinations that preferably surrounds the ^{57}Fe and the Mössbauer spectra. Previous attempts have not been conclusive, in particular those that are based on relating the experimental results with the hyperfine parameters of other well-known materials [64], through finger print ascription method.

With this study we attempt a structural classification of the ^{57}Fe hyperfine parameters based on quantum mechanical calculation simulations of the atomic and the related electronic spatial distributions taking into account different local disorder environments around the ^{57}Fe occupied sites in the $\text{YBa}_2\text{Cu}_{3-x}\text{Fe}_x\text{O}_{7-y}$ oxygen rich tetragonal phase. Moreover, it should be possible to identify the main Mössbauer spectra contributions reported in the literature [39–42, 64, 65] in a consistent way. Finally, an interpretation of the structural changes observed in the high pressure synthesized and the gamma irradiated samples is proposed.

5.2. Calculation Details

The ideal well ordered $\text{YBa}_2\text{Cu}_3\text{O}_{7-y}$ crystal cell structure is orthorhombic (Fig. 5.1) with the Pmmm space group when $7 - y \geq 6.65$, where oxygen site O(5) along the a axis is almost completely unoccupied [143]. For lower oxygen content ($7 - y < 6.65$) this material undergoes an orthorhombic to tetragonal phase transition [144]. In this case the O(4) and O(5) sites are equally probable to be occupied. This phase transition occurs, for example, when the sample is heated over 950 K.

By doping this material with Fe ($\text{YBa}_2\text{Cu}_{3-x}\text{Fe}_x\text{O}_{7-y}$), the doping element occupies mainly the Cu(1) sites at the basal plane, but also, the Cu(2) sites with lesser probability. In this case, the foregoing phase transition occurs at room temperature at doping levels higher than 0.1. Nevertheless, when the sample is synthesized at 1273.15 K under high pressure of 6 GPa for 0.5 h it presents a tetragonal crystal structure for all Fe impurity levels [39–41], with the P4/mmm space group. The Fe doping and the high pressure synthesis of the sample increases the oxygen content [39–41] at the O(4) and O(5) basal plane sites.

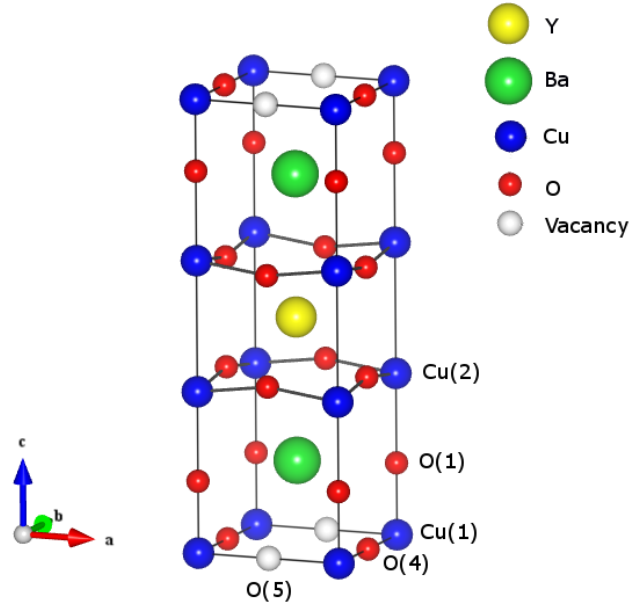


Figure 5.1.: $\text{YBa}_2\text{Cu}_3\text{O}_{7-y}$ crystal unit cell.

Taking into account these effects and the $\text{YBa}_2\text{Cu}_{3-x}\text{Fe}_x\text{O}_{7-y}$ crystal structure symmetry, a group of possible oxygen configurations around the Fe when it occupies the Cu(1) site are proposed. As an approximation, this description will be based on the $\text{YBa}_2\text{Cu}_{3-x}\text{Fe}_x\text{O}_{7-y}$ tetragonal phase, which allows to simulate the electric hyperfine interactions of the ambient pressure (AM) and high pressure (HP) synthesized samples in a simultaneous way, as well as to consider the samples subjected to the gamma irradiation. Then, the structural disorder present in the $\text{YBa}_2\text{Cu}_3\text{O}_{7-y}$ basal plane will be considered, particularly among the O(4) and O(5) positions.

Under this condition, and considering that Fe doping increase the oxygen content of the sample, certain oxygen configurations (OCs) are proposed, as shown in Fig. 5.2. The

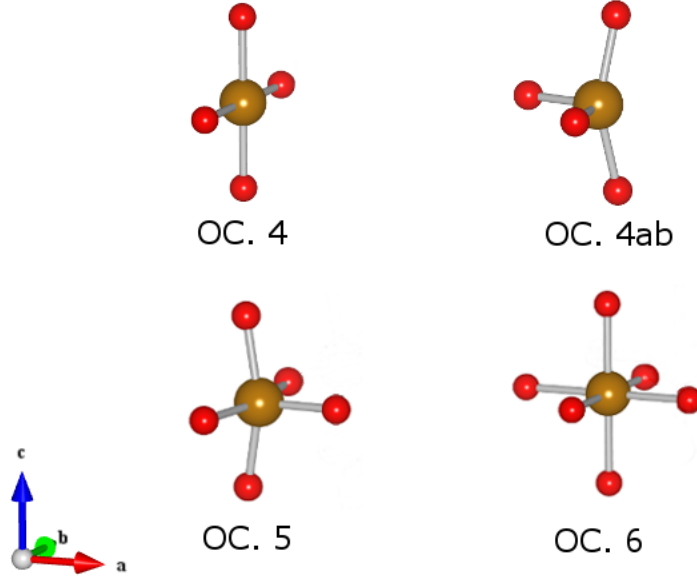


Figure 5.2.: Oxygen configurations (OC) formation considered around Fe in the Cu(1) site.

nomenclature OC. N indicates a OC with coordination number N. It can be observed that different oxygen occupation values are considered, including the ideal case $N = 4$, as well as oxygen rich cases in the samples through coordination values of $N = 5$ and 6 . The OC. 4ab is a quasi-tetrahedral configuration that has been also experimentally reported when the $\text{YBa}_2\text{Cu}_3\text{O}_{7-y}$ sample is doped with Fe [39–42, 64, 65] and is also considered in the current study. Higher oxygen content is taken into account by partially occupation of the O(5) sites around Cu atoms; in this way two oxygen content values will be analyzed for each OC. They will be named normal and high oxygen content configurations. The Fe dopant possibility of been located in the Cu(2) site is also studied with the ideal oxygen coordination $N=5$.

Each proposed ^{57}Fe local configuration is recreated in a supercell(SC) of $2 \times 2 \times 1$ unit cells (see Fig. 5.1). These SCs were initially built from the experimental lattice parameters reported for the normal pressure synthesized sample with a Fe doping concentration of $x = 0.5$ [41], which has tetragonal symmetry. This is equivalent to include two Fe atoms in the $2 \times 2 \times 1$ SC. Then, the SCs lattice parameters were optimized by minimizing the total energy as function of volume and c/a ratio with the ideal OC. 4 and the Fe located in the Cu(1) site. Later, the internal atomic positions were minimized to a force limit below $1 \text{ mRy}/\text{\AA}$ for all the OCs cases. The optimized lattice parameters obtained are $a = 3.8879 \text{ \AA}$ and $c = 11.7098 \text{ \AA}$.

In the electronic structure calculations with the WIEN2k code [82] the non-overlapping muffin-tin spheres radii R_{mt} were set to 2.39, 2.5, 1.85, 1.7 and 1.5 a.u. for Y, Ba, Cu, Fe and O respectively. For the interstitial region, the plane wave expansion was carried out with a cut-off value of $R_{mt}K_{max} = 7.5$. The maximum multipolarity l quantum number for the wave function expansion within the atomic sphere was confined to $l_{max} = 12$. The electrical charge density was Fourier expanded up to $G_{max} = 16\sqrt{Ry}$. The number of k -points in the irreducible part of the Brillouin zone was set to 30. The generalized gradient approximation (GGA) due to Perdew *et al.* [80] was used to describe the exchange and correlation effects, including an effective Coulomb interaction correction ($U_{eff} = U - J$) to describe the strong on-site correlation between the Fe d electrons. The U_{eff} value is taken as 7 eV, determined as an optimal value for Fe in the YBaFe_2O_5 sample [142].

The hyperfine electrical parameters values (isomer shift (δ) and quadrupole splitting (Δ)) are calculated using Eqs. (2.66) and (2.70) from the WIEN2k output parameters (V_{zz} , η and ρ_0). The obtained reference value to evaluate Eq. (2.66) in this case is $\rho_0^{reference} = 15309.841 \text{ a.u.}^{-3}$.

In Table 5.1 the range of hyperfine electric parameters for the main doublets reported in [39–42] are summarized for a later comparison. This table includes the reported values for $\text{YBa}_2\text{Cu}_{3-x}\text{Fe}_x\text{O}_{7-y}$ ($x \geq 0.1$) AM and HP samples, as well as the AM ones subjected to ^{60}Co gamma irradiation.

Table 5.1.: Experimental hyperfine parameters (isomer shift (δ), quadruple splitting (Δ) and line width (Γ)) of the ^{57}Fe main lines in the Mössbauer spectra of $\text{YBa}_2\text{Cu}_{3-x}\text{Fe}_x\text{O}_{7-y}$ ($x \geq 0.1$) samples synthesized at both, ambient pressure (AM) and high pressure (HP) conditions, as well as for AM samples under ^{60}Co gamma irradiation [39–42]. The notation $\text{Cu}(i)n$ denotes that in the experiment was considered that the Fe occupies the (i) site and has n -fold oxygen coordination.

Doublet	$\delta(mm/s)$	$\Delta(mm/s)$	$\Gamma(mm/s)$	AM	HP	$\text{Cu}(i)n$
A	0.06	2.00	0.14	×		$\text{Cu}(1)4$
B	0.33	0.60	0.15	×	×	$\text{Cu}(2)5$
C	-0.05	0.89	0.16	×	×	$\text{Cu}(1)5$
D	0.24	0.16	0.10	×		$\text{Cu}(1)6$

5.3. Results and Discussion

The calculated hyperfine parameter values for the ^{57}Fe located at the Cu sites for the proposed OCs in the $\text{YBa}_2\text{Cu}_{3-x}\text{Fe}_x\text{O}_{7-y}$ are presented in Table 5.2. As expected, it shows that the ^{57}Fe located at the Cu(1) with the considered OCs have different hyperfine parameters values for each coordination number. The increase of the oxygen content in the sample also produce a significant variation in the calculated EFG values.

Table 5.2.: Calculated hyperfine parameters (V_{zz} , η , δ and Δ) for ^{57}Fe located at the Cu sites, considering different OCs and oxygen content in the $\text{YBa}_2\text{Cu}_{3-x}\text{Fe}_x\text{O}_{7-y}$. The average bond distance between Fe and O atoms in the ab plane is also shown.

Site	Config.	$7-y$	$V_{zz}(10^{21}\text{V}/\text{m}^2)$	η	$\delta(\text{mm}/\text{s})$	$\Delta(\text{mm}/\text{s})$	$d_{\text{Fe}-\text{O}_{ab}}(\text{\AA})$	
Cu(1)	OC. 4	7.0	7.31	0.23	0.30	1.23	1.94	
		7.25	5.86	0.76	0.25	1.06	1.91	
	OC. 4ab	7.0	7.51	0.79	-0.11	1.37	1.72	
		7.25	-7.36	0.54	0.00	-1.28	1.80	
	OC. 5	7.25	-10.83	0.03	-0.01	-1.80	1.76	
		7.5	-6.39	0.52	0.23	-1.11	1.96	
	OC. 6	7.5	-2.32	0.23	0.27	-0.39	1.97	
		7.75	2.76	0.88	0.29	0.51	2.00	
	Cu(2)	OC. 5	7.0	3.82	0.88	0.35	0.71	1.93
			7.25	-4.03	0.96	0.13	-0.77	1.89

In Fig. 5.3 a graphical comparison between the experimental and theoretical hyperfine parameters is established. The calculated δ and Δ values for each OC is represented by a symbol, and each experimental line is represented by a square with sides equals to the experimental line width. The comparison shows some correlation between the experimental lines and the calculated OCs, as will be explained in detail below.

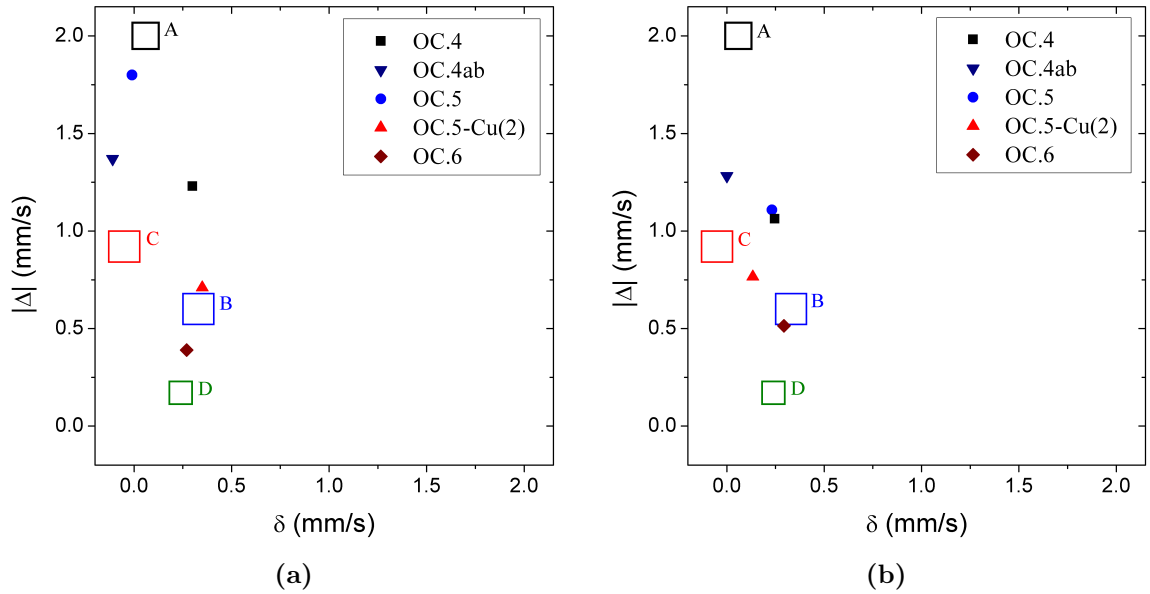


Figure 5.3.: Comparison between experimental and calculated hyperfine parameters δ and Δ for the $\text{YBa}_2\text{Cu}_{3-x}\text{Fe}_x\text{O}_{7-y}$: a) normal oxygen content and b) high oxygen content. The experimental lines distribution region is represented by a square within the corresponding line width interval.

For the AM samples, the correspondence between the doublet D and the OC.6 is in agreement with the experimental statements [42]. However, from the present calculation, it results that the OC.5 seems to be correlated with Doublet A; while the OC.4 and OC.4ab are in partial agreement with doublet C, contrarily to previous arguments [39–42, 133, 144]. Hence, by doping the $\text{YBa}_2\text{Cu}_3\text{O}_{7-y}$ with Fe the occurrence of different OCs in the first Fe neighborhoods are favored and consistent with the observed increase of the oxygen content, specially for $x > 0.4$, as it is shown in Fig. 5.4. The hyperfine parameters obtained for Fe located at the Cu(2) are in good agreement with the ones of line B (see Table. 5.1) as is considered in the experiments [39–42], but also with the OC.6 in the Cu(1) site.

In the case of the HP samples, it seems that local configurations with higher oxygen content dominate the first neighborhoods around Fe and Cu positions. In this case, the

Δ value of OC.5 is 45% smaller than the doublet A and becomes closer to doublet C, showing a clear separation. On the other hand, the OC.6 hyperfine parameters are also in agreement with doublet B as in the AM samples case. This particular finding might be connected to the following fact (see also Fig. 5.4): by HP treatment the oxygen content in $\text{YBa}_2\text{Cu}_3\text{O}_{7-y}$ basal planes increases over 1 atom per formula ($1 + y \geq 1.2$), favoring the O(5) site occupation and the occurrence of the related oxygen configurations OC.5 and OC.6 around Cu and Fe sites. The different oxygen content behaviors between HP- and AM- $\text{YBa}_2\text{Cu}_{3-x}\text{Fe}_x\text{O}_{7-y}$ samples with Fe content seems to be the cause of the total extinction of doublet A observed in the experiment for the HP samples, as was previously stated [39–41]. Finally, the obtained correlation between the doublets experimental hyperfine parameters and the calculated values for the Fe in $\text{YBa}_2\text{Cu}_{3-x}\text{Fe}_x\text{O}_{7-y}$ is summarized in Table 5.3.

Table 5.3.: Correlation between the calculated ^{57}Fe hyperfine parameters for the different OCs and the experimental doublets of the AM and HP $\text{YBa}_2\text{Cu}_{3-x}\text{Fe}_x\text{O}_{7-y}$ samples. The OCs are related to the Cu(1) site, unless the Cu(2) site is indicated.

Doublet	AM	HP
A	OC. 5	–
B	OC. 5 (Cu(2)), OC. 6	OC. 6
C	OC. 4ab, OC. 4	OC. 5, OC. 5 (Cu(2)), OC. 4ab, OC. 4
D	OC. 6	–

On the other hand, in the Mössbauer spectra of AM- $\text{YBa}_2\text{Cu}_{3-x}\text{Fe}_x\text{O}_{7-y}$ samples irradiated with ^{60}Co gamma rays [42], it was observed that the doublet A area decrement is essentially equals to the increment in doublet D, as it is shown in Fig. 5.5. In accordance with the present analysis and the OCs correspondence with the mentioned doublets, this effect can be justified due to possible changes in the oxygen coordinations of the sites associated with doublet A as a result of the DPAs provoked by the gamma radiation through secondary particles. This idea is also supported by recent studies where oxygen atoms DPAs presented a large effect in comparison with other atoms of this material for the ^{60}Co gamma energies [145, 146]. In this way, the OC. 5 sites can become in OC. 6 if an oxygen atom displaced in another crystalline site occupies the vacancy present in the OC. 5.

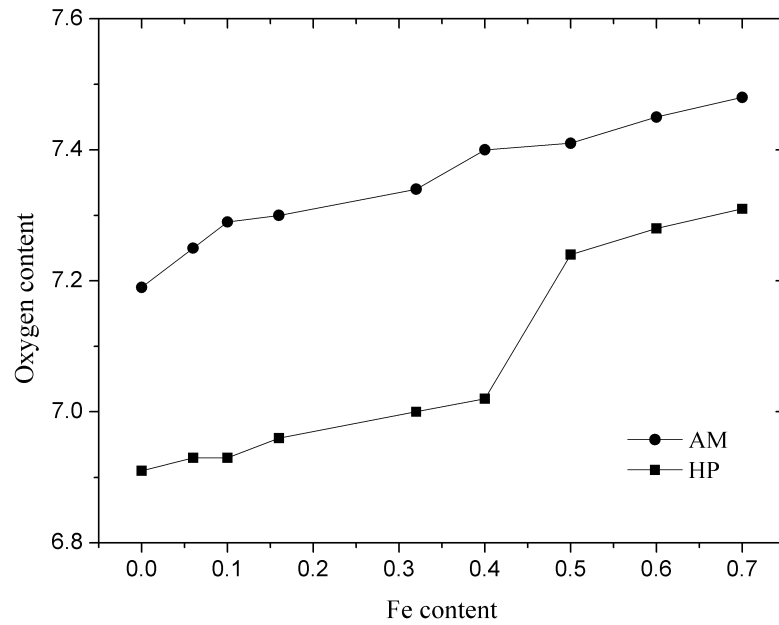


Figure 5.4.: Dependency of the oxygen content on Fe content for the HP and AM samples of $\text{YBa}_2\text{Cu}_{3-x}\text{Fe}_x\text{O}_{7-y}$. The values are taken from [39–41].

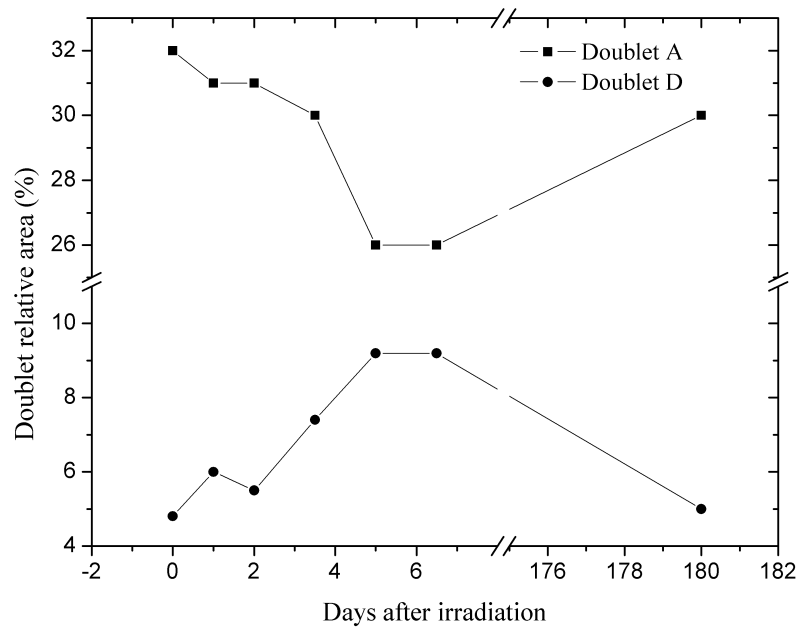


Figure 5.5.: Temporal behavior of the Doublets A and D relative area after the irradiation. The values are taken from [42].

5.4. Conclusions

The ^{57}Fe electrical hyperfine parameters in $\text{YBa}_2\text{Cu}_{3-x}\text{Fe}_x\text{O}_{7-y}$ samples are calculated by introducing different first neighborhood oxygen configurations, OCs, around the ^{57}Fe sites; in order to characterize the measured Mössbauer spectral components in these systems obtained at ambient pressure (AM), high pressure (HP) and under ^{60}Co gamma irradiation conditions. Thus, the hyperfine parameters values calculated for the ^{57}Fe located at those OCs in the Cu(1) site and for the ideal Cu(2) site give a complete microscopic description of the reported main doublets of the $\text{YBa}_2\text{Cu}_{3-x}\text{Fe}_x\text{O}_{7-y}$ Mössbauer spectra, especially their connections with the oxygen disorder in the basal plane sites of their structures.

For AM samples the doublet D agrees with N=6 oxygen coordination in the Cu(1) site and the doublet B with the ideal Cu(2) site, both cases are in concordance with previous experimental arguments. On the contrary, for the HP samples the doublet B agrees with N=6 oxygen coordination in the Cu(1) site. However, a fundamental difference is found for the main doublet A in the AM samples, which seems to be related to a N=5 oxygen coordination environment in the Cu(1) site, and the doublet C corresponds to the one with N=4, in opposite assignments to previous studies [39–42, 133, 144]. But for the HP samples, the N=4 and N=5 OCs are correlated only with doublet C, in connection to the reported extinction of doublet A in these case [39–41]. The HP sample oxygen content increase with respect to the non doped and AM samples seems to support the above mentioned results. This effect imply a relatively higher occurrence of the oxygen rich configuration around Cu and Fe atoms, in agreement the present results.

Finally, for ^{60}Co γ -irradiated AM $\text{YBa}_2\text{Cu}_{3-x}\text{Fe}_x\text{O}_{7-y}$ samples, the proposed structural assignment of hyperfine parameters allows a microscopic interpretation of, the reported population migration from doublet A to D [42], presumably due to coordination changes from N=5 to 6 as a result of OC.5 configuration trapping of oxygen atoms released by atoms displacements induced by the gamma secondary particles.

Summary

Hyperfine interaction techniques have been used for a long time to study radiation effects and defects in solids [1, 2]. Microscopic details of defects and impurities have been studied by these techniques [3–27, 32–43]. It is known that defects in solids can induce characteristic EFGs in the neighboring lattice sites. However, a lot of experimentally well characterized defects via their EFG have remained unidentified. In this content, the current study try to achieve a better understanding of the crystallographic disorder present in some material and establish its correlation with the measured hyperfine parameters.

As studied cases, the following materials were selected: the semiconductors zinc oxide (ZnO) and silicon (Si), and the superconductor yttrium barium copper oxide ($\text{YBa}_2\text{Cu}_{3-x}\text{Fe}_x\text{O}_{7-y}$). In the semiconductors cases the radiation damage is mainly produced by the implantation of hyperfine interaction probe atom, ^{57}Mn (^{57}Fe) and ^{111}In (^{111}Cd) in ZnO, as well as ^{57}Mn (^{57}Fe) in Si. In the superconductor, the crystal structure presents some intrinsic disorder changes caused by high pressure synthesis or gamma irradiation of the material. More details on the specific related problems are analyzed in the thesis.

Several local configurations of the probe atoms, including defects, were proposed and its electronic structure was calculated for the studied materials. The ions implantation process in the semiconductors was simulated by Monte Carlo method obtaining the produced ion and vacancy profiles, used as a criteria in the selection of the possible implantation configurations.

The electronic structure was calculated using the all electrons full-potential (linearized)-augmented-plane-wave plus local orbitals method (L/APW+lo), within DFT, as implemented in the WIEN2k code. On this way, the hyperfine parameters predicted at the probe atoms locations. These results permit to establish a correlation between the experimental reported values and the evaluated local structure neighborhoods, providing a possible crystallographic origin for these observation.

In chapter 3, the calculated EFG values for the ideal ZnO crystal structure show a good agreement with the measured values for both Zn and O sites [126]. The obtained electrical hyperfine parameters and the magnetic properties of ZnO samples in the studied ^{57}Fe configurations are in good agreement with the reported doublets and sextets [26–28]. It results that, the ^{57}Fe could be located in ideal substitutional or interstitial sites, as well as in those sites including point defects (vacancy) in different neighborhoods. After annealing the sample, at temperatures over 700 K, it seems that the predominant configuration is the substitutional site correlated with doublet D2 [26–28]. In general, the obtained results agree with the experimental statement that Fe could stabilize a vacancy in the neighborhood of the implantation site in the ZnO material [28]; and that these defects could enhance the Fe magnetic ordered state in this case.

The EFG and ν_Q values obtained for the proposed $^{111}\text{In}(^{111}\text{Cd})$ implantation configurations in ZnO samples present some clear correlations with the two experimental lines observed. The obtained ν_Q values for the cation substitutional site and including a cation vacancy are in good agreement with the experimental component ν_{Q1} . The line ν_{Q2} seems to be represented by the ^{111}Cd located in the octahedral interstitial site and including a cation vacancy also. This correspondence is in agreement with the observed diminution of the ν_{Q2} component in favor of ν_{Q1} during the sample annealing [25].

The hyperfine electric parameters of various $^{57}\text{Mn}(^{57}\text{Fe})$ local implantation configurations in Si are calculated and reported in chapter 4. The obtained results for the main substitutional and interstitial sites are in correspondence with the measured values and in agreement with previous theoretical reports [63, 131]. The main low temperature damage quadrupole doublet (Fe_D in [20]) could be characterized by configurations where the ^{57}Fe are located in an interstitial or substitutional site with a nearby Si vacancy or a Frenkel pair of defects, respectively. On the other hand, the Fe_N spectral line could be related with various defect complex configurations, including the ^{57}Fe located in a substitutional site with a near vacancy, as well as with the ^{57}Fe located in the interstitial site with a Si interstitial atom in the near neighborhood. This results are in agreement with the observed hyperfine parameters variations with the sample temperature.

The ^{57}Fe electrical hyperfine parameters in $\text{YBa}_2\text{Cu}_{3-x}\text{Fe}_x\text{O}_{7-y}$ samples are calculated in chapter 5. The obtained results give a microscopic description of the reported main Mössbauer spectral components in these systems, obtained at ambient pressure (AM), high pressure (HP) and under ^{60}Co gamma irradiation conditions. For doublets D and B the correlated oxygen coordination is in concordance with previous experimental arguments. However, a fundamental difference is found for the main doublet A in the AM

samples, which seems to be related to a N=5 oxygen coordination environment in the Cu(1) site, while the doublet C corresponds to the one with N=4, contrary to previous studies [39–42, 133, 144]. But for the HP samples, the N=4 and N=5 OCs are correlated only with doublet C, in connection to the reported extinction of doublet A in these case [39–41]. The HP sample oxygen content increases with respect to the AM samples seems to support the above mentioned results. For ^{60}Co γ -irradiated AM $\text{YBa}_2\text{Cu}_{3-x}\text{Fe}_x\text{O}_{7-y}$ samples, the reported population migration from doublet A to D [42], can be due to coordination changes from N=5 to 6 as a result of OC.5 configuration trapping of oxygen atoms released by atoms displacements induced by the gamma secondary particles.

Recommendations for future studies

It can be interesting to study the possible isomer shift dependency with the cell volume. For that purpose volumetric optimizations for each studied configuration, related with different local vicinities, should be done.

The use of a different exchange-correlation functional in the DFT calculations to evaluate the hyperfine parameters could be interesting. In that case we suggest an preliminarily study of the selected functional to save calculation time.

From the experimental point of view, it could be interesting to study ZnO samples doped or implanted with Fe, or with another transition metal, to a later process of irradiation with another type of ionizing radiation that can produce crystalline defects in a controllable way. For example neutrons, protons or slight ions irradiation can be used. This can offer additional information on the effect of the crystalline defects in the magnetic properties of these materials.

In the case of Si implanted with ^{57}Mn (^{57}Fe) a review of the hyperfine parameters experimental measurements can be useful to get a better understanding of the material in this case.

Samenvatting

Technieken gebaseerd op de meting van hyperfine interacties zijn reeds lange tijd in gebruik om stralingseffecten en defecten in de vaste stof te bestuderen [1, 2]. Microscopische details van defecten en onzuiverheden werden met deze technieken bestudeerd [3–27, 32–43]. Het is bekend dat defecten in de vaste stof een gradiënt in het elektrische veld van naburige rooster sites kunnen induceren. Echter, vele, via hun elektrische veld gradiënt (EFG) experimenteel goed gekarakteriseerde defecten, blijven ongeïdentificeerd. In deze context probeert de huidige studie een beter inzicht te verwerven in de kristallijne afwijkingen aanwezig in sommige materialen en een verband te zoeken met de gemeten hyperfine parameters.

De volgende materialen werden geselecteerd als studieobjecten: de halfgeleiders zinkoxide (ZnO) en silicium (Si), en de supergeleider yttrium-barium-koperoxide ($\text{YBa}_2\text{Cu}_{3-x}\text{Fe}_x\text{O}_{7-y}$). In het geval van de halfgeleiders wordt de stralingsschade hoofdzakelijk veroorzaakt door de implantatie van een probe-atoom met hyperfine interactie, ^{57}Mn (^{57}Fe) and ^{111}In (^{111}Cd) in ZnO alsook ^{57}Mn (^{57}Fe) in Si. In de supergeleider vertegenwoordigt de kristalstructuur een zekere intrinsieke wanorde verandering veroorzaakt door synthese onder hoge druk of door bestraling met gammastralen. Details van de specifieke problemen worden geanalyseerd in deze thesis.

Verschillende locale configuraties van de probe-atoom, inclusief defecten, werden vooropgesteld en hun elektronische structuur in de bestudeerde materialen werd berekend. Het ionenimplantatieproces in de halfgeleiders werd bestudeerd via Monte-Carlo simulatie om de geproduceerde ion- en vacatureprofielen te bekomen. Deze werden gebruikt als criteria voor de selectie van mogelijke implantatie configuraties.

De elektronische structuur werd berekend gebruikmakend van de L/APW+lo (linearized augmented plane wave plus local orbitals) methode voor alle elektronen binnen DFT (density functioneel theory) zoals geïmplementeerd in de WIEN2K code. Hierdoor is het mogelijk de hyperfine parameters te voorspellen op de locatie van de probe-atomen. Deze resultaten laten toe een verband vast te stellen tussen de gerapporteerde experimentele

waarden en de geëvalueerde lokale structurele omgeving wat de basis vormt voor een mogelijke kristallografische verklaring voor deze waarnemingen.

In hoofdstuk 3 wordt aangetoond dat de berekende elektrische veld gradiënt (EFG) waarden voor een ideaal ZnO kristal een goede overeenkomst vertoont met de gemeten waarden voor zowel de Zn- als de O-sites [126]. De bekomen elektrische hyperfine parameters and de magnetische eigenschappen van ZnO monsters in de bestudeerde ^{57}Fe configuraties zijn in goede overeenkomst met de waargenomen doubletten en sextets [26–28]. Met als resultaat dat ^{57}Fe kon gelokaliseerd worden in ideale substitutionele of interstitionele sites, alsook in die sites die een puntdefect (vacature) vertonen in verschillende omgevingen. Na temperen van het monster bij temperaturen boven 700 K, is blijikbaar de overheersende configuratie de substitutionele site gecorreleerd met het D2 doublet [26–28]. In het algemeen komen de bereikte resultaten overeen met de experimentele vaststelling dat Fe een vacature in de nabijheid van een geïmplanteerde site kan stabiliseren in ZnO en dat deze defecten de geordende magnetische toestand van Fe kunnen versterken in dit geval.

The EFG and de ν_Q -waarden verkregen voor de voorgestelde $^{111}\text{In}(^{111}\text{Cd})$ implantatie configuraties in ZnO monsters toont een duidelijke correlatie met de twee experimenteel waargenomen lijnen. The verkregen ν_Q -waarden voor de kation substitutionele site met inbegrip van een kation vacature zijn in goede overeenstemming met de experimentele component ν_{Q1} . De ν_{Q2} -lijn wordt vertegenwoordigd door ^{111}Cd gelokaliseerd in de octaëderische interstitiële sites inclusief een kation vacature. Dit is in overeenstemming met de waargenomen vermindering van de ν_{Q2} component ten voordele van ν_{Q1} tijdens tempering van het materiaal.

De elektrische hyperfine parameters van verschillende $^{57}\text{Mn}(^{57}\text{Fe})$ lokale implantatie configuraties in Si worden berekend en besproken in hoofdstuk 4. De verkregen resultaten voor de belangrijkste substitutionele en interstitionele sites zijn in overeenstemming met de gemeten waarden en sluiten aan bij eerdere theoretische studies [63, 131]. De belangrijkste lage temperatuur schade quadrupool doublet (Fe_D in [20]) wordt gekarakteriseerd door een configuratie waarbij het ^{57}Fe gelokaliseerd is in een interstitiële of substitutionele site met een nabije Si vacature of een Frenkel-paar defect respectievelijk. Anderzijds kon de Fe_N spectrale lijn in relatie gebracht worden met verschillende configuraties van defect complexen, met inbegrip van het ^{57}Fe gelokaliseerd in een interstitiële site met een Si interstitieel atoom in de directe nabijheid. Deze resultaten zijn in overeenstemming met de waargenomen variaties van de hyperfine parameters in functie van de monstertemperatuur.

De elektrische hyperfine parameters van ^{57}Fe in $\text{YBa}_2\text{Cu}_{3-x}\text{Fe}_x\text{O}_{7-y}$ monsters werden berekend in hoofdstuk 5. De resultaten geven een microscopische beschrijving van de belangrijkste componenten in de Mössbauer spectra van deze systemen verkregen onder atmosferische (AM) en hoge druk (HP) en onder bestraling met ^{60}Co . Voor de D en B doubletten is de overeenstemmende zuurstof coördinatie in concordantie met vroegere experimentele argumenten. Echter, een fundamenteel verschil werd waargenomen voor doublet A in de AM monsters, dewelke blijkbaar gerelateerd is aan een $N = 5$ zuurstof coördinatie omgeving in de Cu(1) site, terwijl het C doublet overeenstemt met $N = 4$, in tegenstelling tot vorige studies [39–42, 133, 144]. Maar voor de HP monsters zijn de $N = 4$ en $N = 5$ zuurstof coördinaties enkel gecorreleerd met het C doublet, in connectie met de gerapporteerde uitdoving van het A doublet in dit geval [39–41]. Het toename van het zuurstofgehalte in de HP monsters in vergelijking tot de AM monsters ondersteunt de hierboven vermelde resultaten. Voor de $\text{YBa}_2\text{Cu}_{3-x}\text{Fe}_x\text{O}_{7-y}$ AM monsters bestraald met γ -straling afkomstig van een ^{60}Co -bron, kan de geobserveerde populatie migratie van doublet A naar D [42] veroorzaakt worden door de coördinatieverandering van $N = 5$ naar 6 tengevolge van de OC.5 configuratie trapping van zuurstof atomen vrijgesteld door atoomverplaatsingen geïnduceerd door secundaire deeltjes.

Bibliography

- [1] Th. Wichert. *J. Nucl. Mater.*, 216:199–219, 1994.
- [2] A. Zeman, V. Inozemtsev, R. Kamendje, and R. L. Beatty. *J. Nucl. Mater.*, 442: S77–S83, 2013.
- [3] D. A. Goldberg, Y. K. Lee, E. T. Ritter, R. R. Stevens Jr., and J. C. Walker. *Phys. Lett.*, 20(6):571–573, 1966.
- [4] H. Pattyn, R. Coussement, J. De Bruyn, J. Odeurs, and M. Van Rossum. *J. Nucl. Mater.*, 69–70:764–766, 1978.
- [5] W. Mansel, J. Marangos, and D. Wahl. *J. Nucl. Mater.*, 108–109:137–145, 1982.
- [6] E. Kuzmann and I. N. Spirov. *J. Nucl. Mater.*, 137:22–32, 1985.
- [7] R. Govindaraj and K. P. Gopinathan. *J. Nucl. Mater.*, 231:141–145, 1996.
- [8] T. Toriyama, N. Moser, S. Kruijer, W. Keune, W. Kiauka, W. A. A. Macedo, and D. Liljequist. *Nucl. Instr. Meth. B*, 129:474–482, 1997.
- [9] J. A. Sawicki. *J. Nucl. Mater.*, 264:169–179, 1999.
- [10] J. Lipka. *Czech. J. Phys.*, 51(5):503–511, 2001.
- [11] R. Ilola, V. Nadutov, M. Valo, and H. Hänninen. *J. Nucl. Mater.*, 302:185–192, 2002.
- [12] H. Okazawa, T. Yoshiie, T. Ishizai, K. Sato, Q. Xu, Y. Satoh, Y. Ohkubo, and Y. Kawase. *J. Nucl. Mater.*, 329–333:967–970, 2004.
- [13] A. Zeman, L. Debarberis, L. Kupča, B. Acosta, M. Kytka, and J. Degmová. *J. Nucl. Mater.*, 360:272–281, 2007.
- [14] B. Dj. Cekić, A. B. Umićević, J. N. Belošević-Čavor, V. J. Koteski, V. N. Ivanovski, and M. N. Stojković. *Solid State Commun.*, 145:465–468, 2008.
- [15] K. K. Kadyrzhanov, M. F. Vereshchak, I. A. Manakova, A. N. Ozernoy, and V. S. Rusakov. *J. Phys. Chem. Solids*, 74:1078–1085, 2013.
- [16] S. M. Dubiel, J. Cieślak, and H. Reuther. *J. Nucl. Mater.*, 434:235–239, 2013.
- [17] H. P. Gunnlaugsson, G. Weyer, N. E. Christensen, M. Dietrich, M. Fanciulli, K. Bharuth-Ram, R. Sielemann, A. Svane, and the ISOLDE Collaboration. *Physica*

- B*, 340–342:532–536, 2003.
- [18] G. Weyer, H. P. Gunnlaugsson, M. Dietrich, M. Fanciulli, K. Bharuth-Ram, R. Sielemann, and the ISOLDE Collaboration. *Nucl. Instr. Meth. B*, 206:90–94, 2003.
- [19] H. P. Gunnlaugsson, G. Weyer, M. Dietrich, the ISOLDE collaboration, M. Fanciulli, K. Bharuth-Ram, and R. Sielemann. *Appl. Phys. Lett.*, 80:2657–2659, 2002.
- [20] H. P. Gunnlaugsson, M. Fanciulli, M. Dietrich, K. Bharuth-Ram, R. Sielemann, G. Weyer, and ISOLDE Collaboration. *Nucl. Instr. Meth. B*, 186:55, 2002.
- [21] G. Weyer, A. Burchard, M. Fanciulli, V. N. Fedoseyev, H. P. Gunnlaugsson, V. I. Mishin, R. Sielemann, and the ISOLDE Collaboration. *Physica B*, 273-274:363–366, 1999.
- [22] Y. Yoshida, Y. Kobayashi, K. Hayakawa, K. Yukihiro, A. Yoshida, H. Ueno, F. Shimura, and F. Ambe. *Physica B*, 376–377:69–72, 2006.
- [23] R. Dogra, Z. S. Hussain, and A. K. Sharma. *Mater. Charact.*, 58:652 – 657, 2007.
- [24] R. Dogra, A. P. Byrne, Z. S. Hussain, and M. C. Ridgway. *Nucl. Instr. Meth. B*, 266:1460–1463, 2008.
- [25] R. Dogra, A.P. Byrne, and M.C. Ridgway. *Opt. Mater.*, 31:1443–1447, 2009.
- [26] H. P. Gunnlaugsson, K. Johnston, T. E. Møllholt, G. Weyer, R. Mantovan, H. Masenda, D. Naidoo, S. Ólafsson, K. Bharuth-Ram, H. P. Gíslason, G. Langouche, M. B. Madsen, and the ISOLDE Collaboration. *Appl. Phys. Lett.*, 100(4): 042109, 2012.
- [27] H. P. Gunnlaugsson, T. E. Møllholt, R. Mantovan, H. Masenda, D. Naidoo, W. B. Dlamini, R. Sielemann, G. Weyer, K. Johnston, G. Langouche, S. Ólafsson, H. P. Gíslason, Y. Kobayashi, Y. Yoshida, M. Fanciulli, and ISOLDE Collaboration. *Appl. Phys. Lett.*, 97:142501, 2010.
- [28] G. Weyer, H. P. Gunnlaugsson, R. Mantovan, M. Fanciulli, D. Naidoo, and T. Agne. *J. Appl. Phys.*, 102:113915, 2007.
- [29] T. E. Møllholt, R. Mantovan, H. P. Gunnlaugsson, K. Bharuth-Ram, M. Fanciulli, H. P. Gíslason, K. Johnston, Y. Kobayashi, G. Langouche, H. Masenda, D. Naidoo, S. Ólafsson, R. Sielemann, and G. Weyer. *Physica B*, 404:4820–4822, 2009.
- [30] G. Y. Ahn, S.-I. Park, I.-B. Shim, and C. S. Kim. *J. Magn. Magn. Mater.*, 282: 166–169, 2004.
- [31] S.-I. Park, G. Y. Ahn, and C. S. Kim. *J. Appl. Phys.*, 101:09H113, 2007.
- [32] L. Yang, L. Zhen, C. Y. Xu, X. Y. Sun, and W. Z. Shao. *Nucl. Instr. Meth. B*, 267:3084–3086, 2009.

- [33] A. Dogra, S. K. Srivastava, M. Singh, N. Kumar, P. Sen, and R. Kumar. *Radiat. Meas.*, 36:667 – 670, 2003.
- [34] A. Dogra, M. Singh, N. Kumar, P. Sen, and R. Kumar. *Nucl. Instr. Meth. B*, 212:190–196, 2003.
- [35] M. Dietrich, Ch. Buchal, J. G. Correia, M. Deicher, M. Schmid, M. Uhrmacher, U. Vetter, and U. Wahl. *Nucl. Instr. Meth. B*, 216:110–115, 2004.
- [36] A. C. Marques, U. Wahl, J. G. Correia, E. Rita, and J. C. Soares. *Nucl. Instr. Meth. B*, 249:882–885, 2006.
- [37] Y. Tokunaga, M. Osaka, S. Kambe, S. Miwa, H. Sakai, H. Chudo, Y. Homma, and Y. Shiokawa. *J. Nucl. Mater.*, 396:107–111, 2010.
- [38] D. Malczewski and A. Molak. *J. Nucl. Mater.*, 412:239–249, 2011.
- [39] Y. H. Liu, G. C. Che, K. Q. Li, and Z. X. Zhao. *Phys. Rev. B*, 71:104503, 2005.
- [40] Y. H. Liu, G. C. Che, K. Q. Li, Z. X. Zhao, Z. Q. Kou, N. L. Di, and Z. H. Cheng. *Physica C*, 418(1-2):63–67, 2005.
- [41] Y. H. Liu, G. C. Che, K. Q. Li, Z. X. Zhao, Z. Q. Kou, N. L. Di, and Z. H. Cheng. *Solid State Commun.*, 134(10):711–716, 2005.
- [42] M. Z. Jin, X. W. Liu, M. L. Liu, J. Xu, R. Liu, and Y. Q. Jia. *Physica C*, 288:226–230, 1997.
- [43] S. Kambe, H. Sakai, Y. Tokunaga, H. Chudo, H. Yasuoka, T. D. Matsuda, Y. Haga, S. Ikeda, A. Nakamura, E. Yamamoto, D. Aoki, Y. Homma, Y. Shiokawa, and Y. Ōnuki. *J. Nucl. Mater.*, 385:1–3, 2009.
- [44] G. Langouche, editor. *Hyperfine Interaction of Defects in Semiconductors*. Amsterdam, 1992.
- [45] Stavola, editor. *Semiconductors and Semimetals*. Academic Press, San Diego, 1999.
- [46] I. S. Lyubutin, V. G. Terziev, T. V. Dmitrieva, and V. P. Gor'kov. *Phys. Lett. A*, 137(3):144–148, 1989.
- [47] S. P. Walch and W. A. Goddard III. *Chem. Phys. Lett.*, 33(1):18–24, 1975.
- [48] D. R. Spearing. *Comput. Geosci.*, 20(4):615–624, 1994.
- [49] P. Blaha, K. Schwarz, and P. Herzig. *Phys. Rev. Lett.*, 54(11):1192, 1985.
- [50] S. Cottenier and H. Haas. *Phys. Rev. B*, 62:461–467, 2000.
- [51] S. Jalali Asadabadi, S. Cottenier, H. Akbarzadeh, R. Saki, and M. Rots. *Phys. Rev. B*, 66:195103, 2002.

- [52] S. Cottenier, V. Bellini, M. Çakmak, F. Manghi, and M. Rots. *Phys. Rev. B*, 70:155418, 2004.
- [53] V. Bellini, S. Cottenier, M. Çakmak, F. Manghi, and M. Rots. *Phys. Rev. B*, 70:155419, 2004.
- [54] D. Torumba, V. Vanhoof, and S. Cottenier. *Phys. Rev. B*, 74:014409, 2006.
- [55] D. Torumba, K. Parlinski, M. Rots, and S. Cottenier. *Phys. Rev. B*, 74(14):144304, 2006.
- [56] K. M. Wong, S. M. Alay-e Abbas, Y. Fang, A. Shaukat, and Y. Lei. *J. Appl. Phys.*, 114:034901, 2013.
- [57] K. M. Wong, S. M. Alay-e Abbas, A. Shaukat, Y. Fang, and Y. Lei. *J. Appl. Phys.*, 113:014304, 2013.
- [58] S. K. Mohanta, S. N. Mishra, S. K. Srivastava, and M. Rots. *Solid State Commun.*, 150:1789–1793, 2010.
- [59] A. Settels, T. Korhonen, N. Papanikolaou, R. Zeller, and P.H. Dederichs. *Phys. Rev. Lett.*, 83:4369, 1999.
- [60] S. Lany, P. Blaha, J. Hamann, V. Ostheimer, H. Wolf, and Th. Wichert. *Phys. Rev. B*, 62(4):2259–2262, 2000.
- [61] S. Lany, V. Ostheimer, H. Wolf, Th. Wichert, and ISOLDE Collaboration. *Physica B*, 308–310:980–984, 2001.
- [62] Ü. Özgür, Ya. I. Alivov, C. Liu, A. Teke, M. A. Reshchikov, S. Doğan, V. Avrutin, S. J. Cho, and H. Morkoç. *J. Appl. Phys.*, 98:041301, 2005.
- [63] J. Kübler, A. E. Kumm, H. Overhof, P. Schwalbach, M. Hartick, E. Kankeleit, B. Keck, L. Wende, and R. Sielemann. *Z. Phys. B*, 92:155–162, 1993.
- [64] P. Boolchand and D. McDaniel. *Hyperfine Interact.*, 72:125–152, 1992.
- [65] M. Sarkar, N. V. Patel, P. K. Mehta, and R. S. Somayajulu. *Hyperfine Interact.*, 136/137:587–592, 2001.
- [66] D. Barb. *Grundlagen und Anwendungen der Möessbauerspektroskopie*. Akademie-Verlag, Berlin, 1980.
- [67] A. Vértes, L. Korecz, and K. Burger. *Mössbauer spectroscopy*. Amsterdam: Elsevier Scientific, 1979. ISBN 0-444-99782-2.
- [68] M. K. Kubo, Y. Kobayashi, Y. Yamada, M. Mihara, T. Nagatomo, W. Sato, J. Miyazaki, S. Sato, and A. Kitagawa. *Rev. Sci. Instrum.*, 85:02C310, 2014.
- [69] J. M. Millet. *Adv. Catal.*, 51:309–350, 2007.

- [70] G. L. Catchen. *PAC: renaissance of a nuclear technique*, pages 37–46. MRS Bulletin, 1995.
- [71] J. Kohanoff. *Electronic Structure Calculations for Solids and Molecules: Theory and Computational Methods*. Cambridge University Press, 2006.
- [72] R. M. Martin. *Electronic Structure: Basic Theory and Practical Methods*. Cambridge University Press, 2003.
- [73] L. H. Thomas. *Proc. Cambridge Philos. Soc.*, 23:542, 1927.
- [74] E. Fermi. *Z. Phys.*, 48:73, 1928.
- [75] P. Hohenberg and W. Kohn. *Phys. Rev.*, 136:B864, 1964.
- [76] W. Kohn and L. J. Sham. *Phys. Rev.*, 140:A1133, 1965.
- [77] D. C. Langreth and J. P. Perdew. *Phys. Rev. B*, 15:2884, 1977.
- [78] U. von Barth and L. Hedin. *J. Phys. C*, 12:5419, 1979.
- [79] S. K. Ma and K. A. Brueckner. *Phys. Rev.*, 165:18, 1968.
- [80] J. P. Perdew, K. Burke, and M. Ernzerhof. *Phys. Rev. Lett.*, 77:3865, 1996.
- [81] C. Kittel. *Introduction to Solid State Physics (7th ed.)*. New York, Wiley, 1996.
- [82] P. Blaha, K. Schwarz, G. K. H. Madsen, D. Kvasnicka, and J. Luitz. *WIEN2k, An Augmented Plane Wave + Local Orbitals Program for Calculating Crystal Properties*. ISBN 3-9501031-1-2. Karlheinz Schwarz, Techn. Universität Wien, Austria, 2001.
- [83] O. K. Andersen and R. G. Wooley. *Mol. Phys.*, 26:905, 1973.
- [84] J. Korrynga. *Physica*, 13:392, 1947.
- [85] W. Kohn and N. Rostocker. *Phys. Rev.*, 94:1111, 1954.
- [86] O. K. Andersen. *Phys. Rev. B*, 12:3060, 1975.
- [87] M. Methfessel, C. O. Rodriguez, and O. K. Andersen. *Phys. Rev. B*, 40:2009, 1989.
- [88] T. L. Loucks. *Augmented Plane Wave Method*. Benjamin, NY, 1967.
- [89] S. Cottenier. *Density Functional Theory and the Family of (L)APW-methods: a step-by-step introduction*. Instituut voor Kern- en Stralingsfysica, KULeuven, Belgium, 2002. ISBN 90-807215-1-4. URL http://www.wien2k.at/reg_user/textbooks.
- [90] D. Singh. *Phys. Rev. B*, 43:6388, 1991.
- [91] E. Sjöstedt, L. Nordström, and D. Singh. *Solid State Commun.*, 114:15, 2000.
- [92] U. D. Wdowik and K. Ruebenbauer. *Phys. Rev. B*, 76:155118, 2007.

- [93] S. Shang, A. J. Böttger, M. P. Steenvoorden, and M. W. J. Crajé. *Acta Mater.*, 54: 2407–2417, 2006.
- [94] M. Filatov. On the calculation of Mössbauer isomer shift. *J. Chem. Phys.*, 127: 084101, 2007.
- [95] M. Filatov. *Coordin. Chem. Rev.*, 253:594–605, 2009.
- [96] R. Kurian and M. Filatov. *J. Chem. Phys.*, 130:124121, 2009.
- [97] K. Koch and S. Cottenier. Analysis of an Electric-Field Gradient(EFG): the EFG-switch in LAPW2, August 2011. URL http://www.wien2k.at/reg_user/textbooks.
- [98] P. Dufek, P. Blaha, and K. Schwarz. *Phys. Rev. Lett.*, 75(19):3545–3548, 1995.
- [99] P. Herzog et al. *Z. Phys. A*, 294:13, 1980.
- [100] K. Schwarz., C. Ambrosch-Draxl, and P. Blaha. *Phys. Rev. B*, 42(4):2051–2061, 1990.
- [101] S. Blügel, H. Akai, R. Zeller, and P.H. Dederichs. *Phys. Rev. B*, 35:3271, 1987.
- [102] COMPREHENSIVE NUCLEAR MATERIALS. In *Volume 1: Basic Aspects of Radiation Effects in Solids/Basic Aspects of Multi-Scale Modeling*. Elsevier Ltd., 2012. ISBN 978-0-08-056033-5.
- [103] R. S. Averbac and T. Diaz de la Rubia. *Solid State Phys.*, 51:281, 1998.
- [104] M. Yoshida. *J. Phys. Soc. Jpn.*, 16:44, 1961.
- [105] J. R. Beeler and D. G. Besco. *J. Appl. Phys.*, 34:2873, 1963.
- [106] M. T. Robinson and I. M. Torrens. *Phys. Rev.*, 9:5008, 1974.
- [107] J. P. Biersack and L. G. Haggmark. *Nucl. Instrum. Methods*, 174:257, 1980.
- [108] J. F. Ziegler, J. P. Biersack, and M. D. Ziegler. *The Stopping and Range of Ions in Solids (SRIM)*. 2010. URL <http://www.SRIM.org>.
- [109] J. F. Ziegler, M. D. Ziegler, and J. P. Biersack. *Nucl. Instr. Meth. B*, 268:1818–1823, 2010.
- [110] K. Ando. *Science*, 312(5782):1883–1885, 2006.
- [111] C. Klingshirn. *Phys. Status Solidi (b)*, 244(9):3027–3073, 2007.
- [112] M. Bouderbala, S. Hamzaoui, B. Amrani, Ali H. Reshak, M. Adnane, T. Sahraoui, and M. Zerdali. *Physica B*, 403:3326–3330, 2008.
- [113] Y. Saeed, A. Shaukat, N. Ikram, and M. Tanveer. *J. Phys. Chem. Solids*, 69: 1676–1683, 2008.

- [114] C. Persson, C.L. Dong, L. Vayssieres, A. Augustsson, T. Schmitt, M. Mattesini, R. Ahuja, J. Nordgren, C.L. Chang, A. Ferreira da Silva, and J.H. Guo. *Microelectron. J.*, 37:686–689, 2006.
- [115] G. C. Zhou, L. Z. Suna, X. L. Zhong, X. Chen, L. Wei, and J. B. Wang. *Phys. Lett. A*, 368:112–116, 2007.
- [116] M. Ferhat, A. Zaoui, and R. Ahuja. *Appl. Phys. Lett.*, 94:142502, 2009.
- [117] Y. Azzaz, S. Kacimi, A. Zaoui, and B. Bouhafs. *Physica B*, 403:3154–3158, 2008.
- [118] C. L. Dong, C. Persson, L. Vayssieres, A. Augustsson, T. Schmitt, M. Mattesini, R. Ahuja, C. L. Chang, and J.-H. Guo. *Phys. Rev. B*, 70:195325, 2004.
- [119] L. Wu, T. Hou, Y. Wang, Y. Zhao, Z. Guo, Y. Li, and S.-T. Lee. *J. Alloy. Compd.*, 541:250–255, 2012.
- [120] M. Bououdina, N. Mamouni, O. M. Lemine, A. Al-Saie, A. Jaafar, B. Ouladdiaf, A. El Kenz, A. Benyoussef, and E. K. Hlil. *J. Alloy. Compd.*, 536:6672, 2012.
- [121] D. W. Mitchell, S. B. Sulaiman, N. Sahoo, and T. P. Das. *Phys. Rev. B*, 44(13):6728, 1991.
- [122] A. Janotti and C. G. Van de Walle. *J. Cryst. Growth*, 287:58–65, 2006.
- [123] Y. Abreu, C. M. Cruz, P. Van Espen, C. Pérez, I. Piñera, A. Leyva, and A.E. Cabal. *Solid State Commun.*, 152:399–402, 2012.
- [124] G. Gu, G. Xiang, J. Luo, H. Ren, M. Lan, D. He, and X. Zhang. *J. Appl. Phys.*, 112:023913, 2012.
- [125] G. K. H. Madsen, P. Blaha, K. Schwarz, E. Sjöstedt, and L. Nordström. *Phys. Rev. B*, 64:195134, 2001.
- [126] G. Denninger and D. Reiser. *Phys. Rev. B*, 55(8):5073–5078, 1997.
- [127] J. Dai, C. Meng, and Q. Li. *Physica B*, 409:5 – 9, 2013.
- [128] H. Wu, M. R. Hartman, T. J. Udovic, J. J. Rush, W. Zhou, R. C. Bowman Jr, and J. J. Vajo. *Acta Crystallogr. B*, 63(1):63–68, 2007.
- [129] P. Blaha, K. Schwarz, P. Sorantin, and S. B. Trickey. *Comput. Phys. Commun.*, 59:399, 1990.
- [130] I. G. Wood, L. Voadlo, D. P. Dobson, G. D. Price, A. D. Fortes, F. J. Cooper, J. W. Neale, A. M. Walker, W. G. Marshall, M. G. Tucker, D. J. Francis, H. J. Stone, and C. A. McCammon. *J. Appl. Crystallogr.*, 41:886–896, 2008.
- [131] A. Svane. Hyperfine interactions of defects in semiconductors. page 391. Amsterdam: Elsevier, 1992.
- [132] G. Langouche and M. De Potter. *Nucl. Instr. Meth. B*, 19–20:322, 1987.

- [133] Y. Abreu, C. M. Cruz, I. Piñera, and A. Leyva. *Rev. Cub. Fis.*, 26(2A):179–185, 2009.
- [134] V. I. Anisimov, J. Zaanen, and O. K. Andersen. *Phys. Rev. B*, 44:943, 1991.
- [135] V. I. Anisimov, I. V. Solovyev, M. A. Korotin, M. T. Czyzyk, and G. A. Sawatzky. *Phys. Rev. B*, 48:16929, 1993.
- [136] V. I. Anisimov, F. Aryasetiawan, and A. I. Lichtenstein. *J. Phys.: Condensed Matter*, 9:767, 1997.
- [137] A. B. Shick, A. I. Liechtenstein, and W. E. Pickett. *Phys. Rev. B*, 60:10763, 1999.
- [138] U. Schwingenschlögl and C. Schuster. *Phys. Rev. B*, 79:092505, 2009.
- [139] R. Kouba and C. Ambrosch-Draxl. *Phys. Rev. B*, 56(22):14766–14770, 1997.
- [140] B. Zangger and C. Ambrosch-Draxl. *Z. Phys. B*, 104:779–781, 1997.
- [141] P. Blaha, K. Schwarz, and P. Novák. *Int. J. Quantum Chem.*, 101:550–556, 2005.
- [142] C. Spiel, P. Blaha, and K. Schwarz. *Phys. Rev. B*, 79:115123, 2009.
- [143] A. Santoro. *Chemistry of Superconductor Materials*. Noyes Publications, Park Ridge, New Jersey, USA, 1991.
- [144] C. M. Cruz, I. Piñera, A. Leyva, and Y. Abreu. chapter Studies on the Gamma Radiation Responses of High Tc Superconductors, page 135. InTech, 2010. doi: 10.5772/10122.
- [145] I. Piñera, C. M. Cruz, Y. Abreu, and A. Leyva. *Nucl. Instr. Meth. B*, 266(22): 4899–4902, 2008.
- [146] I. Piñera, C. M. Cruz, A. Leyva, and Y. Abreu. *Nucl. Instr. Meth. B*, 265:536–540, 2007.

List of figures

1.1.	Schematic spectrum of ^{57}Fe gamma emission for: a) weakly bound atom, and b) fixed atom.	17
1.2.	Representation of the typical outline of the Mössbauer effect measurement in the transmission geometry.	18
1.3.	Simplified disintegration scheme of ^{57}Mn (^{57}Fe).	19
1.4.	Schematic representation of the hyperfine interactions in the case of a transition $\frac{1}{2} \rightarrow \frac{3}{2}$, like that of ^{57}Fe	20
1.5.	Room-temperature transmission Mössbauer spectra of the normal pressure (AM) sample $\text{Fe}_{0.5}\text{Cu}_{0.5}\text{Ba}_2\text{YCu}_2\text{O}_{7.24}$ measured in [39].	21
1.6.	^{111}In (^{111}Cd) disintegration scheme.	22
2.1.	Partitioning of the unit cell into atomic spheres (I) and interstitial region (II)[82].	45
3.1.	Mössbauer spectra measured at different temperatures in ZnO samples implanted with ^{57}Mn (^{57}Fe), reported in [28].	58
3.2.	Range of 60 keV Mn ions in a ZnO target (a) and vacancies generated in the ZnO target by the implantation process (b), simulated by SRIM-2010.	61
3.3.	Range of 8 MeV In ions in a ZnO target (a) and vacancies generated in the ZnO target by the implantation process (b), simulated by SRIM-2010.	61
3.4.	Schematic representation of the ^{57}Fe and ^{111}Cd implantation sites considered in the ZnO structure.	63
3.5.	Behavior of $d_{\text{Fe-O}}$ with the Fe concentration in the ZnO samples.	67
3.6.	Dependency of δ values with the Fe-O average bonds distance for Fe located at the cation substitutional site of ZnO.	69
3.7.	Comparison between experimental and calculated hyperfine parameters Δ and δ for ZnO implanted or doped with ^{57}Fe	70

3.8. Partial density of states (PDOS) for p and d electrons present in the Fe_{sub} site on ZnO (a), p and d electron anisotropy (Δn_p and Δn_d) (b).	73
3.9. Comparison between experimental and calculated hyperfine parameter: quadrupole frequency (ν_Q), for ZnO implanted with ^{111}Cd	76
3.10. Partial density of states (PDOS) for p electrons present in the Cd sites of ZnO (a), and p electrons anisotropy (Δn_p) (b).	78
4.1. Range of 60 keV Mn ions in the Si target (a) and vacancy generated in the Si target by implantation process (b), simulated by SRIM-2010. . . .	83
4.2. Representation of the main Si crystalline sites where the ^{57}Mn (^{57}Fe) ions can be located.	84
4.3. Comparison between experimental and calculated hyperfine parameters δ and Δ for Si implanted with ^{57}Fe	87
4.4. Site populations as function of the measurement temperature during ^{57}Mn (^{57}Fe) implantation into n-type Si. Taken from [20].	89
5.1. $\text{YBa}_2\text{Cu}_3\text{O}_{7-y}$ crystal unit cell.	93
5.2. Oxygen configurations (OC) formation considered around Fe in the Cu(1) site.	94
5.3. Comparison between experimental and calculated hyperfine parameters δ and Δ for the $\text{YBa}_2\text{Cu}_{3-x}\text{Fe}_x\text{O}_{7-y}$	97
5.4. Dependency of the oxygen content on Fe content for the HP and AM samples of $\text{YBa}_2\text{Cu}_{3-x}\text{Fe}_x\text{O}_{7-y}$	99
5.5. Temporal behavior of the Doublets A and D relative area after the irradiation.	99

List of tables

3.1. Hyperfine parameters experimental values (magnetic hyperfine field (B_{hf}), isomer shift (δ), quadrupole splitting (Δ) and lines width (Γ)) reported in [26–28] for ^{57}Fe implanted into ZnO.	64
3.2. Hyperfine parameters experimental values (quadrupole frequency (ν_Q) and width of the frequency distribution (Γ)) reported in [25] for ^{111}In (^{111}Cd) implanted into ZnO.	64
3.3. Theoretical electrical field gradient component V_{zz} calculated for the ZnO crystalline structure.	65
3.4. Optimized $\text{Zn}_{1-x}\text{Fe}_x\text{O}$ lattice parameters (a and c) obtained for the different studied Fe doping levels.	66
3.5. Theoretical hyperfine parameters, magnetic hyperfine field B_{hf} , electric field gradient V_{zz} , quadrupole splitting Δ and isomer shift δ values for the Fe studied implantation sites in ZnO.	68
3.6. Correlation between the experimental reports for ZnO implanted with ^{57}Fe and the studied configurations, comparing the hyperfine electric parameters values.	70
3.7. Contributions to V_{zz} from a given type of electronic states of harmonic character l for the main ^{57}Fe implantation configurations studied in ZnO.	72
3.8. Calculated magnetic moments of atoms in $\text{Zn}_{0.972}\text{Fe}_{0.028}\text{O}$ for the different studied implantation configurations, including the presence of cation vacancies.	74
3.9. Theoretical EFG components (V_{zz} and η) and the quadrupole frequency (ν_Q) values for the studied Cd implantation sites in ZnO.	75
3.10. Correlation between the experimental reports for ZnO implanted with ^{111}Cd and the studied configurations, comparing the EFG values.	77
3.11. Contributions to V_{zz} from a given type of electronic state of harmonic character l for the studied ^{111}Cd implantation sites.	77
4.1. Experimental values of isomer shift (δ), quadrupole splitting (Δ) and line width (Γ) reported in [17–21] for ^{57}Mn (^{57}Fe) implanted in Si.	85

4.2. Relative configuration energy ($\Delta E(eV)$), calculated isomer shift (δ) and quadrupole splitting (Δ) values for the studied configurations of Fe implanted in Si.	86
4.3. Correlation between the experimental reports and the studied configurations, comparing the hyperfine electric parameters values.	88
5.1. Experimental hyperfine parameters (isomer shift (δ), quadruple splitting (Δ) and line width (Γ)) of the ^{57}Fe main lines in the Mössbauer spectra of $\text{YBa}_2\text{Cu}_{3-x}\text{Fe}_x\text{O}_{7-y}$ ($x \geq 0.1$) [39–42].	95
5.2. Calculated hyperfine parameters (V_{zz} , η , δ and Δ) for Fe located at the Cu sites, considering different OCs and oxygen content in the $\text{YBa}_2\text{Cu}_{3-x}\text{Fe}_x\text{O}_{7-y}$	96
5.3. Correlation between the calculated ^{57}Fe hyperfine parameters for the different OCs and the experimental doublets of the AM and HP $\text{YBa}_2\text{Cu}_{3-x}\text{Fe}_x\text{O}_{7-y}$ samples.	98

List of publications

Publications related with this thesis

1. Y. Abreu, C. M. Cruz, I. Piñera, A. Leyva, A. E. Cabal, P. Van Espen and N. Van Remortel. *Hyperfine electric parameters calculation in Si samples implanted with $^{57}\text{Mn} \rightarrow ^{57}\text{Fe}$* . Physica B, 2014, doi: 10.1016/j.physb.2014.03.028.
2. Y. Abreu, C. M. Cruz, I. Piñera, A. Leyva, A. E. Cabal and P. Van Espen. *DFT study of the hyperfine parameters and magnetic properties of ZnO doped with ^{57}Fe* . Solid State Commun. 185, 2014, pp. 25-29. doi: 10.1016/j.ssc.2014.01.010.
3. Y. Abreu, C.M. Cruz, P. Van Espen, C. Pérez, I. Piñera, A. Leyva and A. E. Cabal. *Electric field gradient calculations in ZnO samples implanted with ^{111}In (^{111}Cd)*. Solid State Commun. 152(5), 2012, pp. 399-402. doi: 10.1016/j.ssc.2011.12.001.
4. Y. Abreu, C. M. Cruz, P. Van Espen, I. Piñera, A. Leyva and A. E. Cabal. *Multiscale modeling of radiation damage and annealing in Si samples implanted with 57-Mn radioactive ions*. IEEE Nuclear Science Symposium Conference Record, 2011, pp. 1754-1756. doi: 10.1109/NSSMIC.2011.6154676.
5. C. M. Cruz, I. Piñera, A. Leyva and Y. Abreu, *Studies on the gamma radiation responses of high Tc superconductors*. In: Superconductor, Adir Moyses Luiz (Ed.), InTech, 2010, pp. 135-160. doi: 10.5772/10122.
6. Y. Abreu, C. M. Cruz, I. Piñera and A. Leyva. *Crystalline disorder influence in $\text{YBa}_2\text{Cu}_{3-x}\text{Fe}_x\text{O}_{7-y}$ Mössbauer spectra*. Rev. Cub. Fis. 26(2A), 2009, pp.179-185, ISSN: 0253-9268 (*In Spanish*).

Other publications

1. P. Arce, J. I. Lagares, L. Harkness, D. Pérez-Astudillo, M. Cañadas, P. Rato, M. de Prado, Y. Abreu, G. de Lorenzo, M. Kolstein and A. Díaz. *GAMOS: A framework to do GEANT4 simulations in different physics fields with an user-friendly interface*. Nucl. Instr. Meth. A 735, 2014, pp. 304313.

2. A. Leyva, I. Piñera, D. Leyva, Y. Abreu and C. M. Cruz. *Electron and positron contributions to the displacement per atom profile in bulk multi-walled carbon nanotube material irradiated with gamma rays*. Nucleus No. 53, 2013, pp. 5-9.
3. I. Piñera, C. M. Cruz, P. Van Espen, Y. Abreu and A. Leyva. *Study of dpa distributions in electron irradiated YBCO slabs through MCCM algorithm*. Nucl. Instr. Meth. B 274, 2012, pp. 191194. doi: 10.1016/j.nimb.2011.11.021.
4. A. Leyva, I. Piñera, D. Leyva, C. M. Cruz, Y. Abreu, A. Díaz and R. Martínez. *Monte Carlo calculation of carbon atom displacement damage in C60 fullerene bulk materials irradiated with gamma rays*. Nucleus 51, 2012, pp. 20-25.
5. R. Martínez, A. Díaz, Y. Abreu, J. Arteché and D. Leyva. *Comparative Analysis of the RSPECT scanner sensibility using GAMOS: a new Geant4 interface*. Nucleus 51, 2012, pp. 14-19.
6. A. Díaz, J. A. Rubio, J. M. Pérez, P. Arce, O. Vela, E. Arista, C. Willmott, Y. Abreu, A. Leyva, I. Piñera and L. Bolaños. *PET-COMPTON system. Comparative evaluation with PET system using Monte Carlo simulation*. Nucleus 51, 2012, pp. 6-13.
7. D. Leyva, A. E. Cabal, P. Van Espen, I. Piñera, A. Leyva and Y. Abreu, *Simulation and evaluation of the absorption edge subtraction technique in energy-resolved X-ray radiography applied to the cultural heritage studies*, Nucleus 50, 2011, pp. 24-30.
8. D. Leyva, A. E. Cabal, A. Leyva, I. Piñera, Y. Abreu and C. M. Cruz. *Quantum efficiency study of a silicon microstrip detector through mathematical modeling*. Nucleus 49, 2011, pp. 21-25. (In Spanish).
9. I. Piñera, Y. Abreu, P. Van Espen, A. Díaz, A. Leyva and C. M. Cruz. *Radiation damage evaluation on LYSO and LuYAP materials through dpa calculation assisted by Monte Carlo method*. IEEE Nuclear Science Symposium Conference Record, 2011, pp. 1609-1611. doi: 10.1109/NSSMIC.2011.6154643.
10. C. M. Cruz, I. Piñera, C. Correa, Y. Abreu and A. Leyva. *MCSAD: Monte Carlo Simulation of Atom Displacements induced by fast electrons in solids*. IEEE Nuclear Science Symposium Conference Record, 2011, pp. 4622-4626. doi: 10.1109/NSSMIC.2011.6154746.
11. P. Arce, J. Ignacio, L. Harkness, L. Desorgher, G. de Lorenzo, Y. Abreu and Z. Wang. *GAMOS: an easy and flexible way to use GEANT4*. IEEE Nuclear Science Symposium Conference Record, 2011, pp. 2230-2237. doi: 10.1109/NSSMIC.2011.6154455.
12. I. Piñera, C. M. Cruz, Y. Abreu and A. Leyva. *Study of the electrons and positrons contribution to the dpa distribution in solids*. Rev. Cub. Fis. 26(2A), 2009, pp.193-196. (In Spanish).
13. A. Leyva, L. M. Montañó, M. Fontaine, C. M. Cruz, I. Piñera and Y. Abreu. *Radiographs mammographic imaging from microcalcifications mannequins and fibrils*

- using a crystalline silicon microstrips detector*. Rev. Cub. Fis. 26(2A), 2009, pp. 133-136. (In Spanish).
14. A. Leyva, A. Cabal, I. Piñera, Y. Abreu, C. M. Cruz, L. M. Montaña, C. C. Díaz, M. Fontaine, C. M. Ortiz, F. Padilla and R. de la Mora. *Use of a c-Si microstrips semiconductor detector for digital radiographic imaging of mannequins and breast biological samples*. Rev. Mex. Fis. 55(4), 2009, pp. 327-331. (In Spanish).
 15. A. Leyva, I. Piñera, O. Dona, A. Díaz, C. M. Cruz, Y. Abreu and L. M. Montaña. *Dpa calculation in CZT matrix detectors exposed to gamma rays*. Nucleus 45, 2009, pp.32-36.
 16. Y. Abreu, I. Piñera, A. Leyva, A. E. Cabal, A. Díaz, L. M. Montaña and C. M. Cruz, *Simulation of a PET System and Study of Some Geometry Parameters*, AIP Conference Proceedings 1032, Tenth Mexican Symposium on Medical Physics, Mexico City, Mexico, 2008, pp. 219-221. doi: 10.1063/1.2979273.
 17. A. Leyva, I. Piñera, L. M. Montaña, Y. Abreu and C. M. Cruz, *Monte Carlo simulation in the optimization of a free-air ionization chamber for dosimetric control in medical digital radiography*, AIP Conference Proceedings 1032, Tenth Mexican Symposium on Medical Physics, Mexico City, Mexico, 2008, pp. 212-214. doi: 10.1063/1.2979271.
 18. A. Leyva, L. M. Montaña, C. C. Díaz, C. M. Ortiz, F. Padilla, R. de la Mora, M. Fontaine, A. Cabal, I. Piñera, Y. Abreu and C. M. Cruz, *Digital radiography of mammographic phantoms and biologic samples using a 64 microstrips crystalline silicon detector coupled to the RX64 ASIC*. AIP Conference Proceedings 1032, Tenth Mexican Symposium on Medical Physics, Mexico City, Mexico, 2008, pp. 215-218. doi: 10.1063/1.2979272.
 19. I. Piñera, C. M. Cruz, Y. Abreu and A. Leyva. *Monte Carlo simulation study of the positron contribution to displacements per atom production in YBCO superconductors*. Nucl. Instr. Meth. B. 266, 2008, pp. 48994902. doi: 10.1016/j.nimb.2008.08.002.
 20. I. Piñera, C. M. Cruz, Y. Abreu, A. Leyva, A. E. Cabal and P. Van Espen. *Monte Carlo assisted classical method for the calculation of dpa distributions in solids materials*. Nuclear Science Symposium Conference Record, Vol. NSS 08, 2008, pp. 2557-2560. doi: 10.1109/NSSMIC.2008.4774878.
 21. C. M. Cruz, I. Piñera, Y. Abreu and A. Leyva. *Theoretical foundations of atom displacements induced by fast electron elastic scattering in solids*. Nuclear Science Symposium Conference Record, Vol. NSS 08, 2008, pp. 2542-2544. doi: 10.1109/NSSMIC.2008.4774874.
 22. I. Piñera, C. Cruz, A. Leyva and Y. Abreu. *Calculation of displacements per atom distributions in solid materials*. Nucleus 41, 2007, pp. 39-44.

23. A. Leyva, I. Piñera, K. Shtejer, Y. Abreu and C. M. Cruz. *Calculation of the displacement cross sections and the dpa distribution in hydrogenated amorphous silicon semiconductors detectors in medical digital imaging applications*. Nucleus 41, 2007, pp. 45-49.
24. I. Piñera, C. M. Cruz, A. Leyva and Y. Abreu. *Displacement per atom calculation in YBCO superconductors through Monte Carlo simulation*. Nucl. Instr. Meth. B 265(2), 2007, pp. 536-540.
25. I. Piñera, C. M. Cruz, Y. Abreu and A. Leyva. *Determination of Atomic Displacements Distribution on YBCO superconductor induced by Gamma Radiation*. Phys. Stat. Sol. (a) 204, 2007, pp. 2279-2286.
26. A. Leyva, C. M. Cruz, M. Mora, K. Shtejer, J.C. Diez, L. A. Angurel, I. Piñera and Y. Abreu. *The effects of ^{137}Cs and ^{60}Co Gamma Radiation on the magnetic susceptibility of BSCCO textured thin rods*. Nucl. Instr. Meth. B 239(3), 2005, pp. 281-285.

Curriculum Vitae

General Information

- Birth: January 25th, 1981, Pinar del Río, Cuba.
- Institution address: Centro de Aplicaciones Tecnológicas y Desarrollo Nuclear (CEADEN), calle 30 No. 502 entre 5ta y 7ma Ave., Miramar, Playa, La Habana, Cuba. CP: 11300.
- Fax: (+53)(7) 202 1518. Telephone: (+53)(7) 206 6109.
- e-mail: yabreu@ceaden.edu.cu.

Education

- B. Sc. Nuclear Physics, July 2004, Instituto Superior de Tecnologías y Ciencias Aplicadas (InSTEC), Havana, Cuba.
- M. Sc. Nuclear Physics, December 2006, InSTEC, Havana, Cuba.

Scientific Employment

- Junior Researcher, Radiation Damage Lab., Physics Depart. CEADEN. (2004–2007)
- Research Candidate, Radiation Damage Lab., Physics Depart. CEADEN. (2007–2011)
- Aggregate Researcher, Radiation Damage Lab., Physics Depart. CEADEN. (from 2011)

Academic Responsibilities

- Instructor Professor, Physics Department, InSTEC, Cuba. (2005–2013)
- Instructor Professor, Physics Department, CUJAE, Cuba. (2005–2008)

Participation in Workshops (last 5 years)

- VIII INTERNATIONAL SYMPOSIUM ON NUCLEAR & RELATED TECHNIQUES, February 5–8, 2013, Havana, Cuba. Oral Presentations and Posters.
- Joint ICTP-IAEA Workshop on Physics of Radiation Effect and its Simulation for Non-Metallic Condensed Matter, ICTP, August 13–24, 2012, Trieste, Italy. Oral Presentation and Poster.
- 2011 IEEE Nuclear Science Symposium and Medical Imaging Conference. Valencia, Spain. October 23–29, 2011. Three Posters.
- VII INTERNATIONAL SYMPOSIUM ON NUCLEAR & RELATED TECHNIQUES, February 7–11, 2011, Havana, Cuba. Oral Presentations and Posters.
- Joint ICTP-IAEA Advanced Workshop on Multi-Scale Modelling for Characterization and Basic Understanding of Radiation Damage Mechanisms in Materials, April 12–23, 2010, ICTP, Trieste, Italy. Poster.
- VI INTERNATIONAL SYMPOSIUM ON NUCLEAR & RELATED TECHNIQUES, February 9–12, 2009, Havana, Cuba. Oral Presentations and Posters.
- 2008 IEEE Nuclear Science Symposium and Medical Imaging Conference. Dresden, Germany. October 19–25, 2008. Two Posters.

Participation in Courses, Seminars and Schools (last 5 years)

- Joint ICTP-IAEA Workshop on Physics of Radiation Effect and its Simulation for Non-Metallic Condensed Matter, ICTP, August 13–24, 2012, Trieste, Italy.
- Summer School “Functional properties at the atomic scale”. May 21–25, 2012, Leuven, Belgium.
- Joint ICTP/IAEA Workshop on Advanced Simulation and Modelling for Ion Beam Analysis, ICTP, February 23–27, 2009, Trieste, Italy.

Organizations and Societies

- Member of the Cuban Physics Society. (from 2004)
- Member of the CEADEN Scientific Committee. (from 2011)

Languages

- First Language: Spanish.
- Second Language: English.